Evidence for charged B meson decays to $a_1^{\pm}\pi^0$ and $a_1^0\pi^{\pm}$ using the *BABAR* detector

Daniel Walker

Department of Physics
H H Wills Physics Laboratory

October 1, 2007

A thesis submitted to the University of Bristol in accordance with the requirements of the degree of Doctor of Philosophy in the Faculty of Science

Abstract

A search for the decays $B^{\pm} \rightarrow a_1^{\pm}(1260)\pi^0$ and $B^{\pm} \rightarrow a_1^0(1260)\pi^{\pm}$ is described here. The a_1 is observed through its decay to $\rho\pi$. The analysis uses a data sample with an integrated luminosity of $210.6\,\mathrm{fb}^{-1}$, corresponding to 232.3×10^6 $B\overline{B}$ pairs. These are produced in e^+e^- annihilation through the $\Upsilon(4S)$ resonance at the PEP-II asymmetric B factory.

The branching ratios averaged over charged conjugate states are measured to be

- $\mathcal{B}(B^{\pm} \rightarrow a_1^{\pm}(1260)\pi^0) \times \mathcal{B}(a_1^{\pm}(1260) \rightarrow \pi^-\pi^+\pi^{\pm})=(13.2 \pm 2.7 \pm 2.1) \times 10^{-6}$
- $\mathcal{B}(B^{\pm} \rightarrow a_1^0(1260)\pi^{\pm}) \times \mathcal{B}(a_1^0(1260) \rightarrow \pi^-\pi^+\pi^0)=(20.4 \pm 4.7 \pm 3.4) \times 10^{-6}$

where the first uncertainties are statistical and the second systematic. The first branching ratio measurement was made with a significance of 4.2σ, and the second one 3.8σ.

AUTHOR'S DECLARATION

I declare that the work in this dissertation was carried out in accordance with the Regulations of the University of Bristol. The work is original except where indicated by special reference in the text and no part of the dissertation has been submitted for any other degree. Any views expressed in the dissertation are those of the author and in no way represent those of the University of Bristol. The dissertation has not been presented to any other University for examination either in the United Kingdom or overseas. The data used in this analysis were recorded by the *BABAR* detector run by the *BABAR* collaboration. The detector hardware, electronics and data acquisition system, as discussed in Chapter 3, and the offline reconstruction software as described in Chapter 4 were developed by the *BABAR* collaboration and are the tools used for recording the data used in the analysis presented in this thesis.

The author contributed to the running of the detector through the taking of general shifts and being the Commissioner of the Electromagnetic Calorimeter Trigger for 20 months. During this period the author developed online monitoring code.

The maximum likelihood analyses described in Chapter 5 were undertaken solely by the author. The event reconstruction process described in Chapters 4 and 5 makes use of code developed centrally within *BABAR* as well as more specific pre-selection code developed by the quasi two-body analysis working group. The author has added various functionality to these packages.

SIGNED: .... DATE: ....

Contents

List of Figures

List of Tables

Chapter 1

Introduction

The Big Bang theory is the accepted description of how the Universe came into existence. It describes how matter and antimatter particles were created in equal amounts, and then how they would have later annihilated producing radiation. In the Universe today, all of the antimatter has annihilated with matter, yet there is still a surplus of matter. The only explanation for this is a matter-antimatter asymmetry, which is small but yet responsible for the existence of the Universe as we know it.

The Standard Model (SM) describes the smallest scale of the Universe, the fundamental particles that make up all matter (and antimatter) and the interactions between them, in a relativistic quantum field and a mathematical gauge theory. All observed matter is thought to consist of various combinations of 12 elementary, spin $\frac{1}{2}$ fermions (6 quarks and 6 leptons). The fundamental interactions are explained by the exchange of spin 1 bosons, whilst a further boson, called the Higgs with spin 0, accounts for particles' masses. The theory is incomplete as it does not incorporate the relatively very weak gravitational interaction. Furthermore, the SM does not address some fundamental questions, such as why there are three generations of fermions; why fermions have mass and why they differ so much; and why the Higgs bare mass in the SM Lagrangian had to be so unnaturally fine-tuned to one part in 10^{17}. These and other issues point towards more fundamental physics at higher energies, for further reading see [1]. However, rigorous and precise experimental measurements show that the SM is an extremely successful model within currently probed energies.

How the rates of various processes differ if particles are exchanged with antiparticles and spatial directions are reversed is termed CP violation. This is one of three conditions identified by Sakharov [2] that must be satisfied to make it possible for the current Universe, with different amounts of matter and antimatter to have evolved from a system with equal amounts. CP violation is explained in the SM, but the amount predicted by this mechanism is too small by several orders of magnitude to account for the observed difference between matter and antimatter in the Universe. This area is therefore an interesting one in which to look for new physics beyond the SM.

Experimentally measuring this effect is a central theme within high energy physics research and the *BABAR* experiment [3] at the Stanford Linear Accelerator Center (SLAC) [4] in California addresses this. The *BABAR* collaboration is composed of around 600 physicists and engineers from around the world.

The analysis presented in this thesis sets out to determine the branching fraction of the decays $B^{\pm} \to a_1^{\pm}\pi^0$ and $B^{\pm} \to a_1^0\pi^{\pm}$. The *BABAR* Collaboration has previously measured the branching fraction of the decay $B^0 \to a_1^{\pm}\pi^{\mp}$ [5] to be $33.2 \pm 3.8 \pm 3.0$. This decay can be used to obtain the weak phase α [6]. A prediction of 38×10^{-6}, within the framework of naive factorisation is made by Bauer, Stech and Wirbel [7], which agrees well with the experimentally determined value. Using the same prediction, expected values for each of the two charged B meson decays to $a_1\pi$ are found to both be 19×10^{-6}. Laporta [8] also makes predictions using the naive factorization approach of $(5 - 11) \times 10^{-6}$ for $B^{\pm} \to a_1^{\pm}\pi^0$ and $(4 - 9) \times 10^{-6}$ for $B^{\pm} \to a_1^0\pi^{\pm}$, where the ranges correspond to different values of the mixing angle. It is feasible to measure this branching fraction from the collected data sample of *BABAR*.

B decays to $a_1\pi$ occur as $b \to u$ transitions at the quark level, and studies of these decays provide an important test of factorisation as well as verifying the $B \to a_1$ transition form factors. These decays are important backgrounds to a study of $B^0 \to (\rho\pi)^0$, an isospin analysis determining the angle α of the unitarity triangle.

Chapter 2 describes the parts of the SM relevant to the *BABAR* experiment and to the decay mode under investigation. The physics requirements, design and performance of the *BABAR* detector and the PEP-II B factory are discussed in Chapter 3. Chapter 4 explains how the raw detector data is reconstructed so that it can be used for physics analyses, and in Chapter 5 the analysis method, which includes event selection, background treatment, the fit procedure and validation is described. The analysis results are presented in Chapter 6. and then discussed in Chapter 7.

Chapter 2

Theory

2.1 Introduction

The purpose of *BABAR* is to make precision measurements of CP violation within the B meson system, of which charmless hadronic B decays play a substantial part. This chapter introduces CP violation in the framework of the Standard Model and its effects on B decays. It also briefly discusses how an investigation of the decay $B^+ \to (a_1\pi)^+$ can help ultimately lead to a measurement of the unitarity triangle angle α.

2.2 CP Violation in Field Theory

The charge conjugation operator, C, is discrete and changes the signs of the internal quantum numbers of a particle, and so changes a particle into its corresponding anti-particle. The parity operator, P, is also discrete and inverts space, so that $(x,t) \to (-x,t)$. The momentum of a particle is reversed by the application of P, however the spin is left unchanged. The time reversal operator, T inverts the time component, so that $(x,t) \to (x,-t)$.

As opposed to the strong and electromagnetic interactions, the symmetries of both the $\mathbf{C}$ and $\mathbf{P}$ transformations are violated by the weak force. This means that only particles with left-handed chirality and antiparticles with right-handed chirality take part in weak interactions in the SM. Chirality is a Lorentz invariant quantity, and for massless particles it is the same as helicity, which is the projection of a particle's spin onto the direction of its motion. Parity violation was first suggested by Lee and Yang in 1956 [9], and experimentally verified (using β decay of cobalt-60) in 1957 by Wu *et al.* [10]. During this same year Ioffe *et al.* showed that $\mathbf{P}$ violation lead to $\mathbf{C}$ invariance being violated in weak decays [11]. As of yet though, there was no evidence to say that the combined transformation of $\mathbf{C}$ and $\mathbf{P}$, $\mathbf{CP}$, was violated. In 1964 Christenson *et al.* presented experimental evidence for the violation of symmetry under the $\mathbf{CP}$ transformation, termed CP violation, in the K^0 meson system [12]. The K_L^0 particle was observed to decay to two pions, as opposed to the expected three, This occurred at the 10^{-3} level.

A property unique to the weak interaction is that it can change the flavour. This mechanism that allows this in quarks is called *quark mixing* and was introduced by Cabibbo in 1963Cabibbo hypothesised that the weak eigenstate d' consists of a linear superposition of the flavour eigenstates d and s. This can then be written as follows for the two quark system:

$$\begin{pmatrix} d' \\ s' \end{pmatrix} = \begin{pmatrix} \cos\theta_C & \sin\theta_C \\ -\sin\theta_C & \cos\theta_C \end{pmatrix} \begin{pmatrix} d \\ s \end{pmatrix}. \tag{2.1}$$

The matrix in Eq. (2.1) is written using the single Cabibbo angle, θ_C, which is measured experimentally to be $12.3°$ [13]. In 1973 Kobayashi and Maskawa suggested a third generation of quarks and leptons [14] with the 2×2 Cabibbo matrix being replaced by the 3×3 *CKM matrix*, $\mathbf{V}_{\mathrm{CKM}}$. Three real angles and one complex phase are required to parameterise this three quark matrix and the complex phase can be shown to be the only source of CP violation in the SM. Not long after this, the first experimental evidence showing the existence of third generation fermions appeared, specifically the discovery of the b quark [15] and the τ lepton [16] in 1977.

In quantum field theory, if a hamiltonian operator is invariant under a Lorentz transformation, then it is also invariant under the CPT transformation. A particle that is unstable is an eigenstate of H with a complex eigenvalue $m - i\Gamma/2$, where m is the mass and Γ is the total decay width. CPT invariance indicates that the mass and lifetime of the particle and anti-particle are the same, however the partial decay widths may still differ. Conservation of CPT implies that if CP violation occurs, then there also must be T violation. Applying the time reversal operator, T transforms e^{-iEt} to e^{iEt}, transforming H into its complex conjugate H^*. Therefore if H and its complex conjugate are not equal then this means /T/ and hence /CP/ is violated.

2.3 CP Violation in the Standard Model

CP Violation can be incorporated in the three generation Standard Model Lagrangian and is done by allowing CP symmetry to be violated, which only shows up in a minority of weak decays. The source of CP violation is a single imaginary parameter in the CKM mixing matrix, this matrix relating the quark weak interaction eigenstates to the mass eigenstates [14]. The weak charged current interaction can be written in terms of the weak eigenstates q':

$$\mathcal{L}_{\text{Int}}^{\text{CC}} = -\frac{g}{\sqrt{2}} \left(\overline{u}'_L, \overline{c}'_L, \overline{t}'_L\right) \gamma^\mu \begin{pmatrix} d'_L \\ s'_L \\ b'_L \end{pmatrix} W_\mu^\dagger + h.c. \tag{2.2}$$

where g is the weak coupling constant, as given by $e/\sin\theta_W$, γ^μ are the Dirac matrices and W_μ are the charged weak bosons. Left handed projections of the *weak* eigenstates of the quark fields are indicated by the q'_L. $h.c.$ represents the hermitian conjugate of the first term. The quarks acquire mass by their Yukawa coupling to the Higgs boson, and so the Lagrangian can be more usefully written in terms of the left-handed projections of mass eigenstates, (q):

$$\mathcal{L}_{\text{Int}}^{\text{CC}} = -\frac{g}{\sqrt{2}} \left(\overline{u}_L, \overline{c}_L, \overline{t}_L\right) \gamma^\mu \mathbf{V}_{\text{CKM}} \begin{pmatrix} d_L \\ s_L \\ b_L \end{pmatrix} W_\mu^\dagger + h.c. \tag{2.3}$$

where $\mathbf{V}_{\text{CKM}}$ is the Cabbibo-Kobayaski-Maskawa (CKM) matrix, which relates the weak eigenstates to the mass eigenstates [14].

Eq. (2.3) can be rewritten in terms of the full quark fields, (u_i, d_j), on which the left-handed projection operator $\frac{1}{2}(1-\gamma_5)$ acts:

$$\mathcal{L}_{\rm Int}^{\rm CC} = -\frac{g}{2\sqrt{2}}(\overline{u}_i\gamma^\mu W_\mu^+\,(1-\gamma_5)\,V_{ij}d_j + \overline{d}_j\gamma^\mu W_\mu^-\,(1-\gamma_5)\,V_{ij}^* u_i). \tag{2.4}$$

Applying the CP operator to the field terms in Eq. (2.4) transforms them as:

$$\overline{u}_i\gamma^\mu W_\mu^+\,(1-\gamma_5)\,d_j \to \overline{d}_j\gamma^\mu W_\mu^-\,(1-\gamma_5)\,u_i. \tag{2.5}$$

Thus it can be seen that the field terms are interchanged, but the $\mathbf{V}_{\rm CKM}$ couplings (V_{ij} and V_{ij}^*) are unchanged, and since $V_{ij} \neq V_{ij}^*$ is likely with a complex element in $\mathbf{V}_{\rm CKM}$, CP violation can appear in the SM.

With only two generations of quarks, the mixing matrix is a 2×2 matrix [17]

$$V_{Cabbibo} = \begin{pmatrix} \cos\theta_C & -\sin\theta_C \\ \sin\theta_C & \cos\theta_C \end{pmatrix} \tag{2.6}$$

This is unitary ($VV^\dagger = 1$) and the phases must be non-trivial, which means they cannot be removed by a redefinition of the fields. The Cabbibo mixing matrix has only one parameter θ, which is real. This means that there is no CP violation with only two generations.

Kobayashi and Maskawa introduced a third quark family [14], so that the electro-weak gauge theory can accommodate CP violation. The relationship between the weak and mass eigenstates becomes

$$\begin{pmatrix} d' \\ s' \\ b' \end{pmatrix} = \mathbf{V}_{\rm CKM} \begin{pmatrix} d \\ s \\ b \end{pmatrix} = \begin{pmatrix} V_{ud} & V_{us} & V_{ub} \\ V_{cd} & V_{cs} & V_{cb} \\ V_{td} & V_{ts} & V_{tb} \end{pmatrix} \begin{pmatrix} d \\ s \\ b \end{pmatrix}. \tag{2.7}$$

where for example, V_{us} is the weak coupling between u and s. This had already been seen in the K meson system in 1964 [12]. The CKM matrix is again unitary and the phases must be non-trivial. This means that it has four independent parameters, three of which are real and one imaginary. This imaginary parameter is the cause of CP violation in the SM.

It is possible to parameterise the CKM matrix in different ways. Eq. (2.8) is the PDG favoured parameterisation [18], where $s_{ij} = \sin\theta_{ij}$, $c_{ij} = \cos\theta_{ij}$, δ is the complex phase and θ_{12}, θ_{13} and θ_{23} are real angles:

$$\mathbf{V}_{\mathrm{CKM}} = \begin{pmatrix} c_{12}\,c_{13} & s_{12}\,c_{13} & s_{13}\,e^{-i\delta} \\ -s_{12}\,c_{23} - c_{12}\,s_{23}\,s_{13}\,e^{i\delta} & c_{12}\,c_{23} - s_{12}\,s_{23}\,s_{13}\,e^{i\delta} & s_{23}\,c_{13} \\ s_{12}\,s_{23} - c_{12}\,c_{23}\,s_{13}\,e^{i\delta} & -c_{12}\,s_{23} - s_{12}\,c_{23}\,s_{13}\,e^{i\delta} & c_{23}\,c_{13} \end{pmatrix}, \tag{2.8}$$

From experimental results, the magnitudes of the matrix elements are $|V_{ii}| \approx 1$,$|V_{12}| \approx |V_{21}| \approx \lambda$, $|V_{23} \approx |V_{32}| \approx \lambda^2$ and $|V_{13}| \approx |V_{31}| \approx \lambda^3$ (where $\lambda \approx V_{us} \approx \sin\theta_C \approx 0.22$, $c_{13} \approx 1$ and $s_{12} \approx \lambda$). This parameterisation is useful to represent $\mathbf{V}_{\mathrm{CKM}}$ as an expansion of the variable λ. A and ρ are real numbers of order unity and the complex component is described by η. Hence $\mathbf{V}_{\mathrm{CKM}}$ can be parameterised as first suggested by Wolfenstein [19]:

$$\mathbf{V}_{\mathrm{CKM}} = \begin{pmatrix} 1-\frac{\lambda^2}{2} & \lambda & A\lambda^3(\rho - i\eta) \\ -\lambda & 1-\frac{\lambda^2}{2} & A\lambda^2 \\ A\lambda^3(1-\rho-i\eta) & -A\lambda^2 & 1 \end{pmatrix} + \mathcal{O}(\lambda^4). \tag{2.9}$$

The CKM matrix must be unitary, which in effect means that the number of quarks is conserved and the matrix is self-contained. This can be expressed by:

$$\mathbf{V}^{\dagger}_{\mathrm{CKM}}\mathbf{V}_{\mathrm{CKM}} = \mathbf{I} = \mathbf{V}_{\mathrm{CKM}}\mathbf{V}^{\dagger}_{\mathrm{CKM}} \tag{2.10}$$

There are several relations that derive from this, which can be separated into two types:

$$\textstyle\sum_j |V_{ij}|^2 = 1 \quad \text{and} \tag{2.11}$$

$$\begin{gathered} \sum_i V_{id}V^*_{is} = 0 \quad \textstyle\sum_i V_{is}V^*_{ib} = 0 \quad \displaystyle\sum_i V_{id}V^*_{ib} = 0 \\ \sum_j V_{uj}V^*_{cj} = 0 \quad \textstyle\sum_j V_{cj}V^*_{tj} = 0 \quad \displaystyle\sum_j V_{uj}V^*_{tj} = 0 \end{gathered} \tag{2.12}$$

where $i = u, c, t$ and $j = d, s, b$. Eq. (2.11) describes weak universality, implying that the sum of all the couplings of any up-type quark to the down-type quarks is independent of the generation considered.

Of the relations in Eq. (2.12), the most useful is:

$$V_{ud}\,V^*_{ub} + V_{cd}\,V^*_{cb} + V_{td}\,V^*_{tb} = 0. \tag{2.13}$$

Each of the three terms contributing are of similar magnitude, of order λ^3. It can also be expressed visually in the form of a triangle in the complex plane, as shown in Figure 2.1. This is called the Unitarity Triangle, where $V_{cd}V^*_{cb}$ is chosen to be real, and also the terms are normalised by $|V_{cd}V^*_{cb}|$. This convention ensures that two of the corners lie at $(0,0)$ and $(1,0)$. The three angles, α, β and γ are given by:

$$\alpha \equiv \arg\left[-\frac{V_{td}\,V^*_{tb}}{V_{ud}\,V^*_{ub}}\right], \quad \beta \equiv \arg\left[-\frac{V_{cd}\,V^*_{cb}}{V_{td}\,V^*_{tb}}\right], \quad \gamma \equiv \arg\left[-\frac{V_{ud}\,V^*_{ub}}{V_{cd}\,V^*_{cb}}\right]. \tag{2.14}$$

The triangle apex is at $(\overline{\rho}, \overline{\eta})$, where $\overline{\rho} = (1-\frac{\lambda^2}{2})\rho$ and $\overline{\eta} = (1-\frac{\lambda^2}{2})\eta$, where λ, ρ and η are the quantities used in the Wolfenstein parameterisation of the CKM matrix. $\frac{V_{td}V^*_{tb}}{|V_{cd}V^*_{cb}|} \approx 1$ and so the two sides of the unitarity triangle opposite γ and α are of the same length. By measuring the angles of the unitarity triangle in as many independent ways as possible, CP violation in the Standard Model can be verified.

There is also a model independent measure of the amount of CP violation in the Standard Model, called the Jarlskog invariant [20], which is given by Eq. (2.15):

$$J = c_{12}c_{23}c^2_{13}s_{12}s_{23}s_{13}\sin\delta \approx A^2\eta\lambda^6. \tag{2.15}$$

where the area of the unitarity triangle is equal to $J/2$.

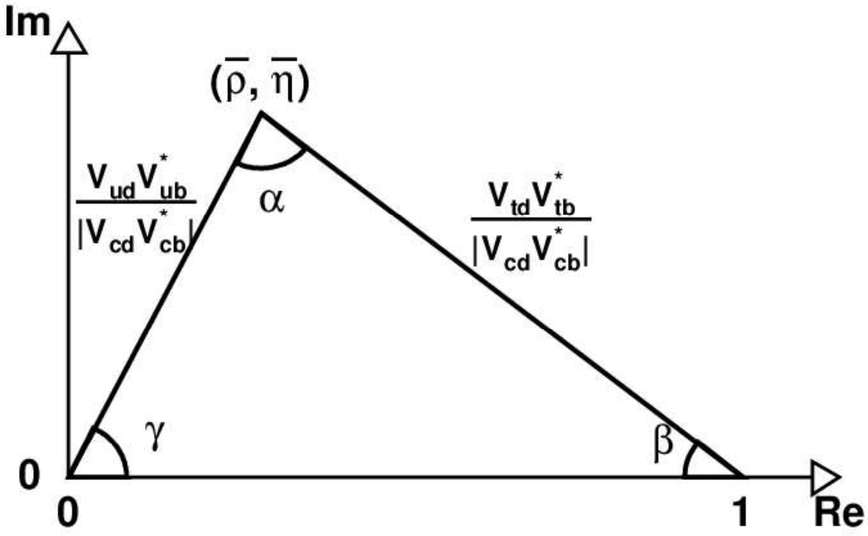

Figure 2.1: The Unitarity Triangle.

2.4 CP Violation in B Decays

The lifetime of B mesons is $\sim 10^{-12}s$ [21]. An estimate of $|V_{cb}|$ can be found by comparing this lifetime with that of the μ lifetime. The weak interaction couples universally, so the lifetimes of all particles that decay weakly is proportional to m^{-5}. From this the B meson lifetime can be determined to be $\tau_B \sim \tau_\mu (\frac{m_\mu}{m_B})^5 \sim 10^{-15}s$. The observed discrepancy is due to the quark mass eigenstates being different from the weak eigenstates. The mixing matrix introduces a factor $|V_{cb}|^2$, and so $|V_{cb}| \sim 1/30$ being of the order λ^2. This also means that the sides of the unitarity triangle are of similar sizes, and also that the angles are large. This means that B decays have weak phases of order unity, and large CP violation.

Three different types of CP violation may occur in B decays: *Direct CP violation*, or CP violation in decay is caused by the interference between different diagrams that contribute to the same final state. This process happens for the decay of both charged and neutral B mesons, and results in an asymmetry between a branching fraction for a B decay and the conjugate process. In charmless decays in particular, this effect may be large due to interference of similar sized tree and penguin contributions. Both of the other types of CP violation found in B decays are indirect. Second order weak interactions mean that neutral B mesons can transform into their anti-particle. The two states mix and a neutral B meson will oscillate between the B^0 and $\overline{B}^0$ states. There is *CP violation in mixing*, which is very small and *CP violation due to interference in decays with and without mixing*. This results in a time-dependent matter anti-matter asymmetry, which can be observed because the B lifetime is long enough so that mixing oscillations are measurable. In B mesons, the b quark is very heavy, so approximations in theoretical calculations mean that the SM model parameters can be extracted from these asymmetries.

2.4.1 Mixing in neutral mesons

Figure 2.2 has examples of box diagrams showing *mixing* in the SM, through which particle and antiparticle states can oscillate. For most particle-antiparticle systems this is not permitted, as various quantum numbers must be conserved independent of whether the interaction is strong, electromagnetic or weak. However, for a few systems, including the neutral K, D and B systems, there are no quantum numbers to conserve when considering the weak interaction. When this is so, the observed physical particles correspond not to the flavour eigenstates, ($|P^0\rangle$ and $|\overline{P}^0\rangle$, which have a particular quark content, but to linear combinations of these.

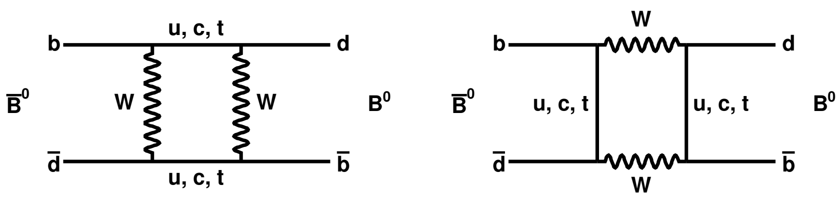

Figure 2.2: Feynman diagrams showing the second order weak interactions that cause $B^0-\overline{B}^0$ mixing. The top quark dominates these transitions due to its large mass and because $V_{tb} \approx 1$.

We can consider the time evolution of an arbitrary state, which consists of a linear superposition of the flavour eigenstates:

$$|P(t)\rangle = a(t)|P^0\rangle + b(t)|\overline{P}^0\rangle, \tag{2.16}$$

which is determined by the time dependent Schrödinger equation (TDSE):

$$i\frac{\partial}{\partial t}\begin{pmatrix} a(t) \\ b(t) \end{pmatrix} = \mathbf{H}\begin{pmatrix} a(t) \\ b(t) \end{pmatrix} = \begin{pmatrix} H_{11} & H_{12} \\ H_{21} & H_{22} \end{pmatrix}\begin{pmatrix} a(t) \\ b(t) \end{pmatrix} = \left(\mathbf{M} - \frac{i}{2}\mathbf{\Gamma}\right)\begin{pmatrix} a(t) \\ b(t) \end{pmatrix}. \tag{2.17}$$

where $\mathbf{H}$ is the Hamiltonian matrix, and $\mathbf{M}$ and $\mathbf{\Gamma}$ are 2×2 Hermitian matrices that describe mixing and decay respectively.

Invariance under the $\mathbf{CPT}$ transformation, where $\mathbf{T}$ is the time reversal operator, is a principle of quantum field theory and assumed to be true. This invariance requires that H_{11} and H_{22} are equal. The off-diagonal elements, H_{12} and H_{21} are the amplitudes for mixing, and if these elements are zero then no mixing will occur.

2.4.1.1 Mixing without CP violation

For CP symmetry to be true, we require that $H_{12}^* = H_{21}$. With no CP violation Eq. (2.17) becomes

$$i\frac{\partial}{\partial t}\begin{pmatrix} a(t) \\ b(t) \end{pmatrix} = \begin{pmatrix} A & B \\ B^* & A \end{pmatrix}\begin{pmatrix} a(t) \\ b(t) \end{pmatrix} = \begin{pmatrix} M_{11} - \frac{i}{2}\Gamma_{11} & M_{12} - \frac{i}{2}\Gamma_{12} \\ \left(M_{12} - \frac{i}{2}\Gamma_{12}\right)^* & M_{22} - \frac{i}{2}\Gamma_{22} \end{pmatrix}\begin{pmatrix} a(t) \\ b(t) \end{pmatrix}. \tag{2.18}$$

$\mathbf{H}$ can be diagonalised to express this in the mass basis. $\mathbf{X}$ is defined to be the matrix with columns containing the eigenvectors of $\mathbf{H}$ so that:

$$\mathbf{H} = \mathbf{X}\begin{pmatrix} A + |B| & 0 \\ 0 & A - |B| \end{pmatrix}\mathbf{X}^{-1}, \tag{2.19}$$

where $A + |B|$ and $A - |B|$ are eigenvalues of $\mathbf{H}$. The mass eigenstates can be expressed as:

$$|P_{1,2}\rangle = \frac{1}{\sqrt{2}}\left(|P^0\rangle \pm |\overline{P}^0\rangle\right), \tag{2.20}$$

The masses and widths of the mass eigenstates are given by the real and imaginary parts of the eigenvalues respectively:

$$M_{1,2} = \Re(A \pm |B|), \quad -\frac{\Gamma_{1,2}}{2} = \Im(A \pm |B|). \tag{2.21}$$

If CP invariance is exact, them the mass eigenstates are also CP eigenstates, which have eigenvalues of ± 1:

$$\begin{aligned}
\mathbf{CP}|P_1\rangle &= \mathbf{CP}\left(\frac{1}{\sqrt{2}}\left(|P^0\rangle + |\overline{P}^0\rangle\right)\right) \\
&= \frac{1}{\sqrt{2}}\left(\mathbf{CP}|P^0\rangle + \mathbf{CP}|\overline{P}^0\rangle\right) \\
&= \frac{1}{\sqrt{2}}\left(e^{i\delta}|\overline{P}^0\rangle + e^{-i\delta}|P^0\rangle\right) \\
&= \frac{1}{\sqrt{2}}\left(|P^0\rangle + |\overline{P}^0\rangle\right), \text{ choosing the convention } \delta = 0 \\
&= (+1)\,|P_1\rangle, \qquad (2.22) \\
\mathbf{CP}|P_2\rangle &= \mathbf{CP}\left(\frac{1}{\sqrt{2}}\left(|P^0\rangle - |\overline{P}^0\rangle\right)\right) \\
&= \frac{1}{\sqrt{2}}\left(\mathbf{CP}|P^0\rangle - \mathbf{CP}|\overline{P}^0\rangle\right) \\
&= \frac{1}{\sqrt{2}}\left(e^{i\delta}|\overline{P}^0\rangle - e^{-i\delta}|P^0\rangle\right) \\
&= -\frac{1}{\sqrt{2}}\left(|P^0\rangle - |\overline{P}^0\rangle\right), \text{ choosing the convention } \delta = 0 \\
&= (-1)\,|P_2\rangle. \qquad (2.23)
\end{aligned}$$

2.4.1.2 Mixing with CP violation

If CP invariance is not assumed to be exact, the off-diagonal elements of $\mathbf{H}$ are not required to be of equal magnitude, and $\mathbf{H}$ can now be expressed as:

$$\mathbf{H} = \begin{pmatrix} A & B/r \\ rB^* & A \end{pmatrix}. \qquad (2.24)$$

The mass eigenstates can be written as:

$$|P'_{1,2}\rangle = \frac{1}{\sqrt{1+|r|^2}}\left(|P^0\rangle \pm r|\overline{P}^0\rangle\right). \qquad (2.25)$$

The masses and widths of the two states derive from the real and imaginary parts of $A \pm |B|$, and the mass eigenstates are no longer CP eigenstates.

2.4.1.3 $B^0 - \overline{B}^0$ mixing

The neutral B meson mass eigenstates, $|B_L\rangle$ and $|B_H\rangle$, can be written as linear superpositions of the flavour eigenstates, $|B^0\rangle$ and $|\overline{B}^0\rangle$, as shown in Eq. (2.26):

$$\begin{aligned} |B_L\rangle &= p|B^0\rangle + q|\overline{B}^0\rangle, \\ |B_H\rangle &= p|B^0\rangle - q|\overline{B}^0\rangle, \end{aligned} \tag{2.26}$$

where p and q are complex coefficients, this allowing for a phase difference between the two states, and this satisfies the normalisation condition of:

$$|p|^2 + |q|^2 = 1. \tag{2.27}$$

The mass, M, mass difference, Δm_B, and lifetime difference, $\Delta\Gamma_B$, are defined as:

$$\begin{aligned} M &= \frac{1}{2}\left(M_H + M_L\right), \\ \Delta m_B &= M_H - M_L, \\ \Delta\Gamma_B &= \Gamma_H - \Gamma_L; \end{aligned} \tag{2.28}$$

$M_{H,L}$ and $\Gamma_{H,L}$ are particular quantities described in Eq. (2.21).

Experimentally it has been found [22] that

$$\Delta m_B \gg \Delta\Gamma_B \approx \mathcal{O}(1\%) \tag{2.29}$$

A general B state $|\psi(t)\rangle$ propagating through space is a superposition of the mass eigenstates, and evolves with time like:

$$|\psi(t)\rangle = a_L(t)|B_L\rangle + a_H(t)|B_H\rangle, \tag{2.30}$$

where the amplitudes $a_L(t)$ and $a_H(t)$ are time dependent and solutions of the TDSE, as given by:

$$\begin{aligned} a_L(t) &= a_L(0)e^{-iM_Lt}e^{-\frac{1}{2}\Gamma_Lt}, \\ a_H(t) &= a_H(0)e^{-iM_Ht}e^{-\frac{1}{2}\Gamma_Ht}. \end{aligned} \tag{2.31}$$

It can be seen from Eq.s (2.26), (2.30) and (2.31) that for a pure $|B^0\rangle$ state at time $t = 0$, the following condition must be satisfied:

$$a_L(0) = a_H(0) = \frac{1}{2p}, \tag{2.32}$$

and similarly for a pure $|\overline{B}^0\rangle$ state at time $t = 0$:

$$a_L(0) = -a_H(0) = \frac{1}{2q}. \tag{2.33}$$

If we substitute Eq.s (2.26) and (2.31) into (2.30), then invoke Eq.s (2.28), (2.32) and (2.33), we can show how a state being initially pure $|B^0\rangle$ evolves to become pure $|\overline{B}^0\rangle$ (similarly for initial pure $|\overline{B}^0\rangle$ states), and then oscillates between the two states. The relation $\Gamma_L = \Gamma_H = \Gamma$ is used, which follows from: Eq. (2.29)):

$$\begin{aligned} |B^0(t)\rangle &= g_+(t)|B^0\rangle + \frac{q}{p}g_-(t)|\overline{B}^0\rangle, \\ |\overline{B}^0(t)\rangle &= \frac{p}{q}g_-(t)|B^0\rangle + g_+(t)|\overline{B}^0\rangle, \end{aligned} \tag{2.34}$$

with

$$\begin{aligned} g_+(t) &= e^{-iMt}e^{-\frac{1}{2}\Gamma t}\cos\left(\frac{\Delta m_B t}{2}\right), \\ g_-(t) &= e^{-iMt}e^{-\frac{1}{2}\Gamma t}\sin\left(\frac{\Delta m_B t}{2}\right). \end{aligned} \tag{2.35}$$

So, it follows that the probability a state beginning as a pure $|B^0\rangle$ will decay as a $|\overline{B}^0\rangle$, will oscillate sinusoidally, having a frequency depending on Δm_B.

2.4.2 Three types of CP violation

Within the framework of the SM, CP violation becomes observable in three ways. Each of these three types will now be discussed.

2.4.2.1 Direct CP Violation

This type is also termed CP violation in decay, and occurs when the amplitude for a decay and its CP conjugate process are different. It is the only type permitted for charged B decays.

Both strong and weak processes can contribute to direct CP violation. Weak phases change sign under CP transformations, but strong phases do not. There is the possibility of direct CP violation only if the amplitude contains non-trivial strong and weak phases. The amplitude of $B^0 \to f$, where f is any final state, and its CP conjugate can be written as

$$A_f = \sum_i A_i e^{i(\delta_i + \phi_i)}, \quad \overline{A}_{\overline{f}} = e^{i\xi} \sum_i A_i e^{i(\delta_i - \phi_i)}, \tag{2.36}$$

where each process that contributes has an amplitude A_i, a weak phase of ϕ_i and a strong phase δ_i, where ξ is some arbitrary phase. For CP violation to occur the following is required:

$$A_f \neq \bar{A}_{\bar{f}}. \tag{2.37}$$

For this to be true, there must be contributions from at least two processes with different strong and weak phases, which is shown in Eq. (2.38) where there are two contributing processes:

$$|A_f|^2 - |\bar{A}_{\bar{f}}|^2 = -2 \sum_{ij} A_i A_j \sin(\phi_i - \phi_j) \sin(\delta_i - \delta_j). \tag{2.38}$$

It turns out to be useful when making experimental measurements of this effect if the amplitudes for these processes are of similar magnitudes.

The observed asymmetry, $\mathcal{A}_{CP}^D$ can be written as:

$$\mathcal{A}_{CP}^D = \frac{\Gamma(\overline{B} \to \bar{f}) - \Gamma(B \to f)}{\Gamma(\overline{B} \to \bar{f}) + \Gamma(B \to f)} = \frac{\left|\bar{A}_{\bar{f}}/A_f\right|^2 - 1}{\left|\bar{A}_{\bar{f}}/A_f\right|^2 + 1}. \tag{2.39}$$

Direct CP violation has been experimentally observed in the K system [23, 24] and subsequently in B decays in which the quantity $\frac{\Gamma(B^0 \to K^- \pi^+) - \Gamma(B^0 \to K^+ \pi^-)}{\Gamma(B^0 \to K^- \pi^+) + \Gamma(B^0 \to K^+ \pi^-)}$ was measured to be -0.133 ± 0.031 by the *BABAR* collaboration [25]. The theoretical calculations of these asymmetries involve knowing the strong phases and the relative contributions of the various diagrams, of which estimates have large theoretical uncertainties.

2.4.2.2 CP violation in mixing

CP violation in B meson mixing is observed as a difference in the rates for the $P^0 \to \overline{P}^0$ and $\overline{P}^0 \to P^0$ transitions. This difference is due to interference between the box diagrams as shown in Figure 2.2, occurring between those proceeding via the t quark and those occurring through other flavours. This happens if the mass eigenstates are different to the CP eigenstates:

$$\mathbf{CP}|P_{1,2}\rangle \neq \pm|P_{1,2}\rangle \tag{2.40}$$

which means that the mass eigenstates are described by Eq. (2.25) as opposed to Eq. (2.20)).

Following Eq.s (2.22)-(2.23), it can be shown that for the B system, which is described by Eq. (2.26), to ensure $|B_{L,H}\rangle$ are CP eigenstates and CP therefore conserved, (q/p) must equal 1. To obtain an interpretable result, a phase convention-independent approach must be adopted so that δ can take on any value, and this is not necessarily zero:

$$\begin{aligned}
\mathbf{CP}|B_{L,H}\rangle &= \mathbf{CP}\left(p|B^0\rangle \pm q|\overline{B}^0\rangle\right) \\
&= \mathbf{CP}\left(|p|\, e^{i\arg(p)}|B^0\rangle \pm |q|\, e^{i\arg(q)}|\overline{B}^0\rangle\right) \\
&= |p|\, e^{i\arg(p)}\, e^{i\delta}|\overline{B}^0\rangle \pm |q|\, e^{i\arg(q)}\, e^{-i\delta}|B^0\rangle \\
&= \pm\left(|p|\left|\frac{q}{p}\right|\, e^{i(\arg(q)-\delta)}|B^0\rangle \pm |q|\left|\frac{p}{q}\right|\, e^{i(\arg(p)+\delta)}|\overline{B}^0\rangle\right) \\
&= \pm|B_{L,H}\rangle, \text{ if} && (2.41) \\
\left|\frac{q}{p}\right| e^{i(\arg(q)-\delta)} &= e^{i\arg(p)}, \text{ and} && (2.42) \\
\left|\frac{p}{q}\right| e^{i(\arg(p)+\delta)} &= e^{i\arg(q)}. && (2.43)
\end{aligned}$$

From this it can be seen that there is always a value of δ that will satisfy Eq. (2.41), as long as $|q/p| = 1$.

For CP violation to occur it is required that:

$$\left|\frac{q}{p}\right| \quad \left(= \left|\sqrt{\frac{\left\langle \overline{B}^0 \left|\mathbf{H}\right| B^0 \right\rangle}{\left\langle B^0 \left|\mathbf{H}\right| \overline{B}^0 \right\rangle}}\right|\right) \quad \neq 1. \tag{2.44}$$

Also termed *indirect CP violation*, this type of CP violation was the first type to be found to exist in the K system. Within the B meson system, the level of indirect CP violation is expected to be small, of order (10^{-4})This is due to $|q/p| \approx 1$, as implied by Eq. (2.29).

2.4.2.3 CP Violation Due to Interference Between Decays With and Without Mixing

This type of CP violation originates from the interference of decays with and without mixing. It is observed for both B^0 and $\overline{B}^0$ decays to the same final state, so we can say $f = \overline{f} = f_{CP}$, and that this is a CP eigenstate.

If $A_{f_{CP}}$ is the amplitude of $B^0 \to f_{CP}$ and $\bar{A}_{f_{CP}}$ is the amplitude of $\overline{B}^0 \to f_{CP}$ then the following phase convention independent quantity $\lambda_{f_{CP}}$ can be used:

$$\lambda_{f_{CP}} = \frac{q}{p}\frac{\bar{A}_{f_{CP}}}{A_{f_{CP}}}. \tag{2.45}$$

CP violation will then occur when $\lambda_{f_{CP}}$ is not equal to unity, which can come about from either direct or indirect CP violation. For direct CP violation, $|\frac{\bar{A}_{f_{CP}}}{A_{f_{CP}}}| \neq 1)$, and for indirect CP violation, $(|\frac{q}{p}| \neq 1)$. It can though happen that there is no CP violation in either mixing or decay, and for this to be true the imaginary part of $\lambda_{f_{CP}}$ must be non-zero as follows:

$$\Im\left(\lambda_{f_{CP}}\right) \neq 0; \quad |\lambda_{f_{CP}}| = 1. \tag{2.46}$$

When this is so, $\lambda_{f_{CP}}$ becomes a pure phase calculable without having to consider hadronic uncertainties.

Using Eq. (2.34) the time dependent amplitudes for $B^0, \overline{B}^0 \to f_{CP}$ can be expressed as:

$$\begin{aligned} \left\langle f_{CP}\left|\mathbf{H}\right|B^0(t)\right\rangle &= A_{f_{CP}}\left(g_+(t) + \lambda_{f_{CP}} g_-(t)\right), \\ \left\langle f_{CP}\left|\mathbf{H}\right|\overline{B}^0(t)\right\rangle &= A_{f_{CP}}\frac{p}{q}\left(g_-(t) + \lambda_{f_{CP}} g_+(t)\right). \end{aligned} \tag{2.47}$$

By taking the modulus squared of the amplitudes, the rates of these processes are:

$$\Gamma(t)(B^0 \to f_{CP}) = \left|\left\langle f_{CP}\left|\mathbf{H}\right|B^0(t)\right\rangle\right|^2$$

$$
\begin{aligned}
&= |A_{f_{CP}}|^2 e^{-\Gamma t}\Bigg(\frac{1+|\lambda_{f_{CP}}|^2}{2} + \frac{1-|\lambda_{f_{CP}}|^2}{2}\cos(\Delta m_B t) \\
&\quad -\Im(\lambda_{f_{CP}})\sin(\Delta m_B t)\Bigg), \\
\Gamma(t)(\overline{B}^0 \to f_{CP}) &= \left|\left\langle f_{CP}\left|\mathbf{H}\right|\overline{B}^0(t)\right\rangle\right|^2 \\
&= |A_{f_{CP}}|^2 e^{-\Gamma t}\Bigg(\frac{1+|\lambda_{f_{CP}}|^2}{2} - \frac{1-|\lambda_{f_{CP}}|^2}{2}\cos(\Delta m_B t) \\
&\quad +\Im(\lambda_{f_{CP}})\sin(\Delta m_B t)\Bigg),
\end{aligned} \tag{2.48}
$$

where the $g_{\pm}$ as defined in Eq. (2.35) is used and also $|q/p| = 1$ is assumed to be true.

$\mathcal{A}^I_{CP}(t)$, which is the time dependent asymmetry is the difference between the two rates in Eq. (2.48) as a fraction of their sum:

$$
\begin{aligned}
\mathcal{A}^I_{CP}(t) &= \frac{\Gamma(t)(\overline{B}^0 \to f_{CP}) - \Gamma(t)(B^0 \to f_{CP})}{\Gamma(t)(\overline{B}^0 \to f_{CP}) + \Gamma(t)(B^0 \to f_{CP})} \\
&= \frac{-\left(1-|\lambda_{f_{CP}}|^2\right)\cos(\Delta m_B t) + 2\Im(\lambda_{f_{CP}})\sin(\Delta m_B t)}{1+|\lambda_{f_{CP}}|^2} \\
&= -C_{f_{CP}}\cos(\Delta m_B t) + S_{f_{CP}}\sin(\Delta m_B t)\,,
\end{aligned} \tag{2.49}
$$

where C and S, the direct and indirect CP asymmetries are:

$$
C_{f_{CP}} = \frac{1-|\lambda_{f_{CP}}|^2}{1+|\lambda_{f_{CP}}|^2} \quad \text{and} \quad S_{f_{CP}} = \frac{2\Im(\lambda_{f_{CP}})}{1+|\lambda_{f_{CP}}|^2} = \sin(2\beta). \tag{2.50}
$$

Figure 2.3 and Figure 2.4 show plots of the direct CP asymmetry, C and the indirect CP asymmetry S respectively.

With $|\lambda_{f_{CP}}| = 1$ it can be seen that Eq. (2.49) reduces to

$$
\mathcal{A}^I_{CP}(t) = \Im(\lambda_{f_{CP}})\sin(\Delta m_B t)\,. \tag{2.51}
$$

For most B decays, the level of direct and indirect CP violation is negligible. CP violation in interference between decays with and without mixing occurs at measurable levels and, with $|\lambda_{f_{CP}}| \approx 1$, is the least complicated one to measure using *BABAR*.

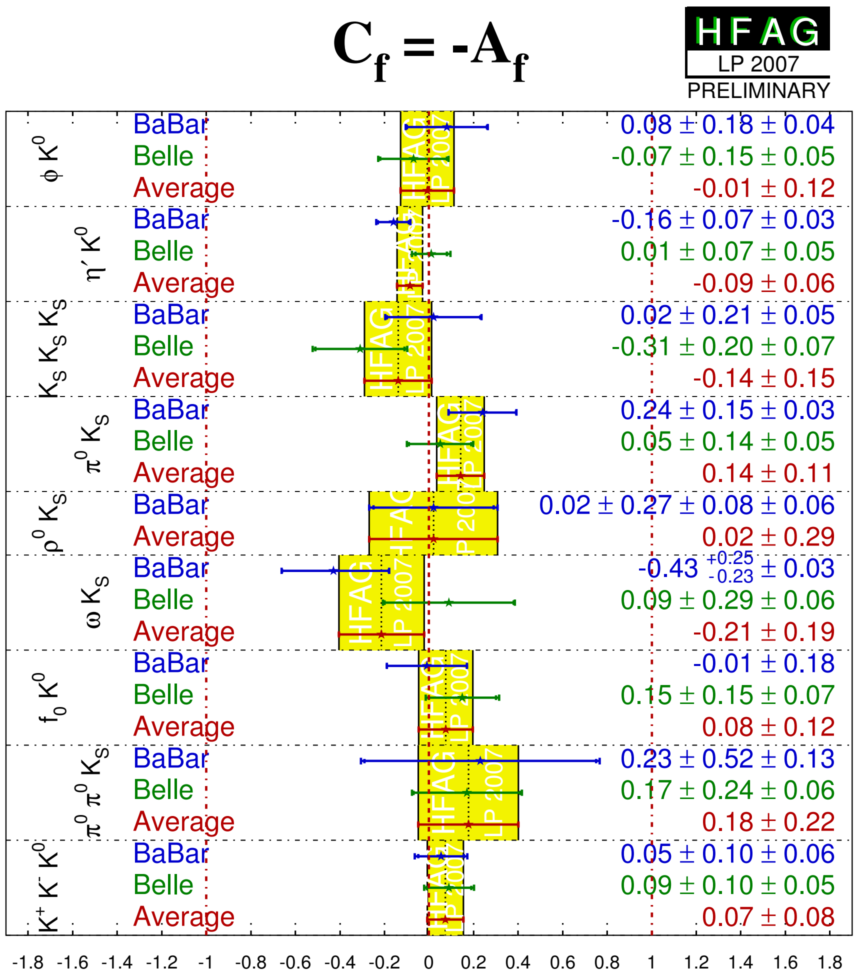

Figure 2.3: The direct CP asymmetry, C_f from *BABAR* and Belle

2.4.3 Current knowledge of CKM parameters

The B meson system is an excellent environment in which to measure several of the $\mathbf{V}_{\mathrm{CKM}}$ parameters. In general the angles in the Unitarity Triangle can be measured using time dependent CP studies, whilst branching ratio measurements are used to determine the lengths of the sides.

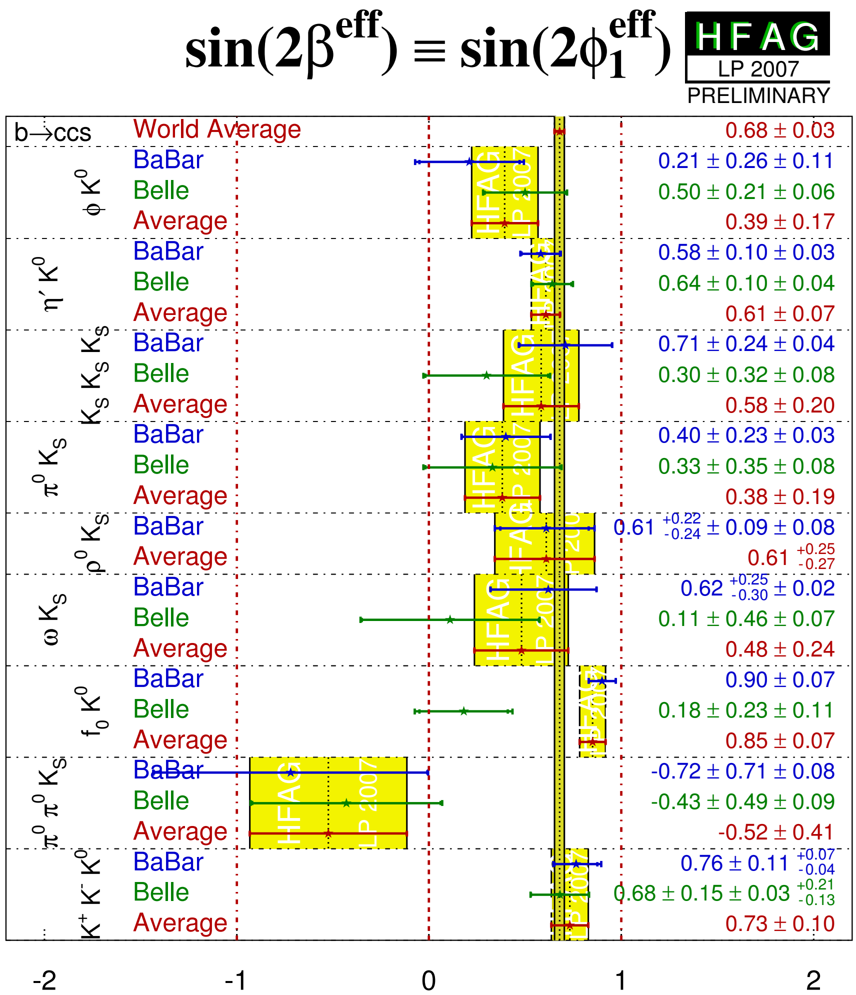

Figure 2.4: The indirect *CP* asymmetry, S_f, which is equal to $\sin(2\beta)$, with results from the world average of charmonium decays, compared with charmless penguin decays from *BABAR* and Belle.

The angle β of the Unitarity Triangle has been measured to a high precision within both the *BABAR* and Belle [26] collaborations, by determining $\sin 2\beta$ using the 'golden channel' $B^0 \rightarrow J/\psi K_S^0$:

- *BABAR*: $\sin 2\beta = 0.72 \pm 0.05 \pm 0.02$ [27].
- Belle: $\sin 2\beta = 0.64 \pm 0.03 \pm 0.02$ [28]
- World average measurement of $\sin 2\beta = 0.675 \pm 0.026$ [29]

These measurements constrain the area of the Unitarity Triangle to be non zero, and hence provide concrete experimental evidence of CP violation in the SM.

To measure the other angles of the unitarity triangle, α and γ, at an equivalent precision requires much larger datasets. The angle α is best measured using the interference of $b \to u$ decay amplitudes with $B^0 - \overline{B}^0$ mixing, but $b \to u$ is CKM suppressed and non-negligible penguin contributions causing possible significant direct CP violation further complicate matters. Measuring γ poses an even bigger challenge as it suffers, depending on the method employed, from either experimental, for example suppressed rates, or theoretical difficulties, for example large hadronic uncertainties. There are also promising methods utilising B_s mesons but these will be best implemented using LHC data, as of now, the LHC [30] experiments have not yet commenced data-taking. Further discussion of methods used to extract Unitarity Triangle angles can be found in [21, 31, 32].

The current experimental knowledge of the CKM sector can be summarised using the four parameters λ, A, $\overline{\rho}$ and $\overline{\eta}$ as defined in the Wolfenstein parameterisation in Eq. (2.9). The parameter λ ($= |V_{us}|$) is 0.22 as found from $K^+ \to \pi^0 \ell^+ \nu_\ell$ decays, with an accuracy of $\approx 2\%$ [33]. The parameter A ($= |V_{cd}|$) is also moderately well known from the studies of B decays to charm states. Its value is $(40.2^{+2.1}_{-1.8}) \times 10^{-3}$ [33]. The parameters $\overline{\rho}$ and $\overline{\eta}$ are less well known. It is revealing to plot the constraints on the $(\overline{\rho}, \overline{\eta})$ as obtained from the measurements of numerous parameters, which include:

- Unitarity Triangle angles.
- B mixing parameters: Δm_s for $B^0_s - \overline{B}^0_s$ mixing and Δm_d for $B^0_d - \overline{B}^0_d$ mixing, where $B^0_d \equiv B^0$, $\Delta m_d \equiv \Delta m_B$ as defined in Eq. (2.28))).
- The neutral kaon mixing parameter ϵ_K, which is defined as $\frac{1-\epsilon_K}{1+\epsilon_K} = \frac{q}{p}$, where p and q

are the values from the K system and are analogous to p and q from Eq. (2.26).

- The sides of the triangle opposite the angles γ and α can be written as $R_u = (1-\lambda^2/2)\,|V_{ub}/V_{cb}|/\lambda$ and $R_t = |V_{tb}/V_{cb}|/\lambda$. Inclusive semileptonic B decays to charmless states are used to measure $|V_{ub}|$ [34], which allows R_u to be calculated to a precision of $\approx 20\%$. R_t is mainly constrained using mixing analyses as $\Delta m_d \propto |V_{td}V_{tb}^*|$, the theoretical hadronic uncertainties leading to an uncertainty in the measurement of $|V_{td}|$ of the order of 20%.

The plot resulting from the various CKM constraints is shown in Figure 2.5, based on a results presented at Flavor Physics and CP Violation conference in 2007. The plot was generated using the `CKMfitter` package [33], with the non-shaded areas being excluded at the 95% CL. For $\sin 2\beta$, also shown are 68% CLs.

CP violation has now been observed in numerous channels; the current values obtained experimentally (at 90% CLs) for the magnitudes of the $\mathbf{V}_{\text{CKM}}$ elements are [18]

$$|\mathbf{V}_{\text{CKM}}| = \begin{pmatrix} 0.97377 \pm 0.00027 & 0.2257 \pm 0.0021 & 0.00431 \pm 0.0003 \\ 0.230 \pm 0.011 & 0.957 \pm 0.11 & 0.00416 \pm 0.0006 \\ 0.0074 \pm 0.0008 & 0.0406 \pm 0.0027 & 0.77 \pm 0.21 \end{pmatrix} \tag{2.52}$$

Figure 2.5 represents significant constraints on these parameters. Over-constraining them is necessary so that variations from the SM description of flavour changing processes might be detected. This would show up in any observed discrepancies between measured parameters using decay modes that should be independent of each other.

Figure 2.6 shows the result of measurements of the CKM angle α for charmless $B\overline{B}$ modes, namely $B^+ \to \rho\pi, \rho\rho$ and $\pi\pi$. Figure 2.7 shows experimental results of measurements of the angle γ as measured in charm $B\overline{B}$ decays in *BABAR*.

2.5 Strong Hadronic Interactions

The weak interactions are comparatively simple, but it is necessary to consider complications introduced by radiative corrections, which come from the emission and absorption of gluons.

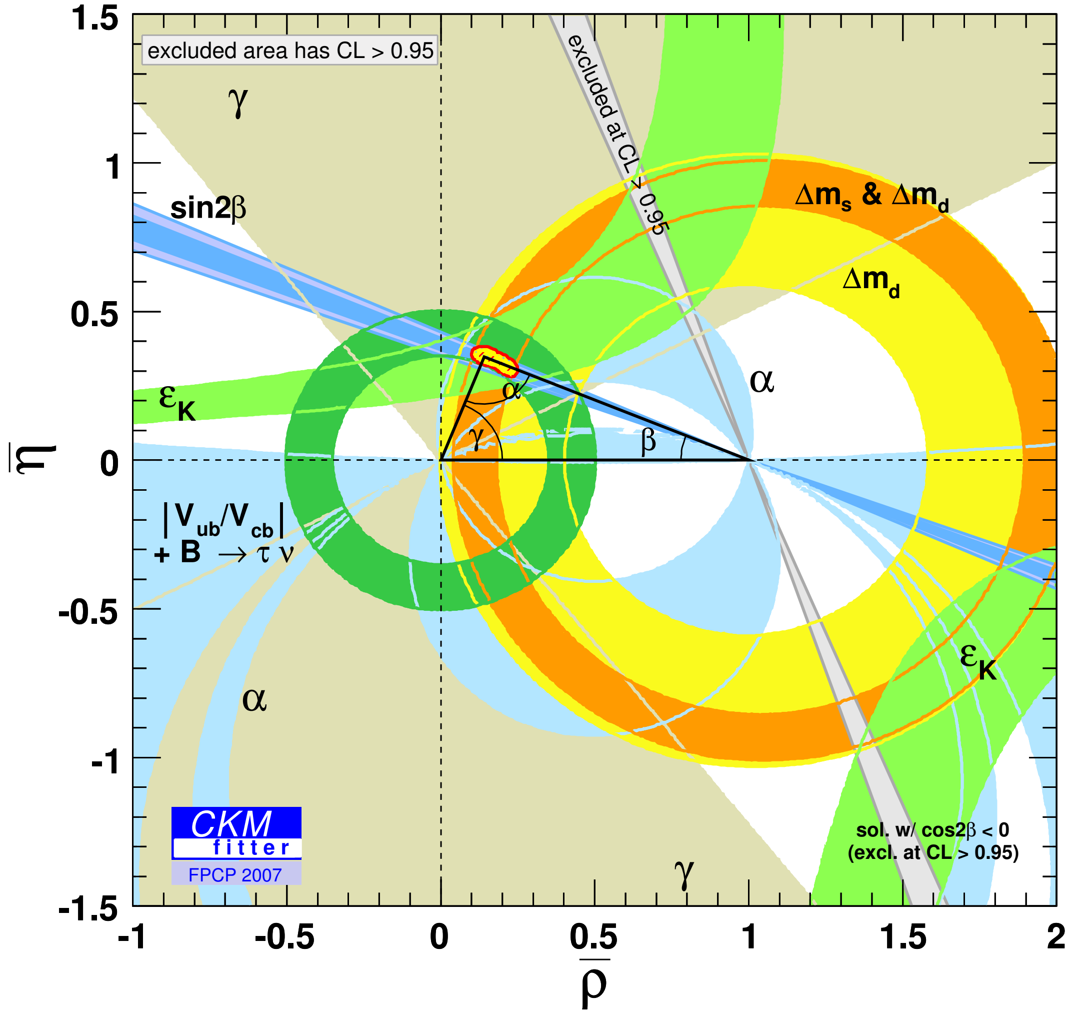

Figure 2.5: Constraints on the CKM matrix depicted in the $(\overline{\rho}, \overline{\eta})$ plane. The apex of the Unitarity Triangle is constrained to the pale yellow area with the red outline.

The gluons can have a range of momenta, which complicates the calculations of cross sections. This section will consider the methods used to estimate these QCD effects in hadronic B decays, so that predictions of branching fractions and CP asymmetries can be made.

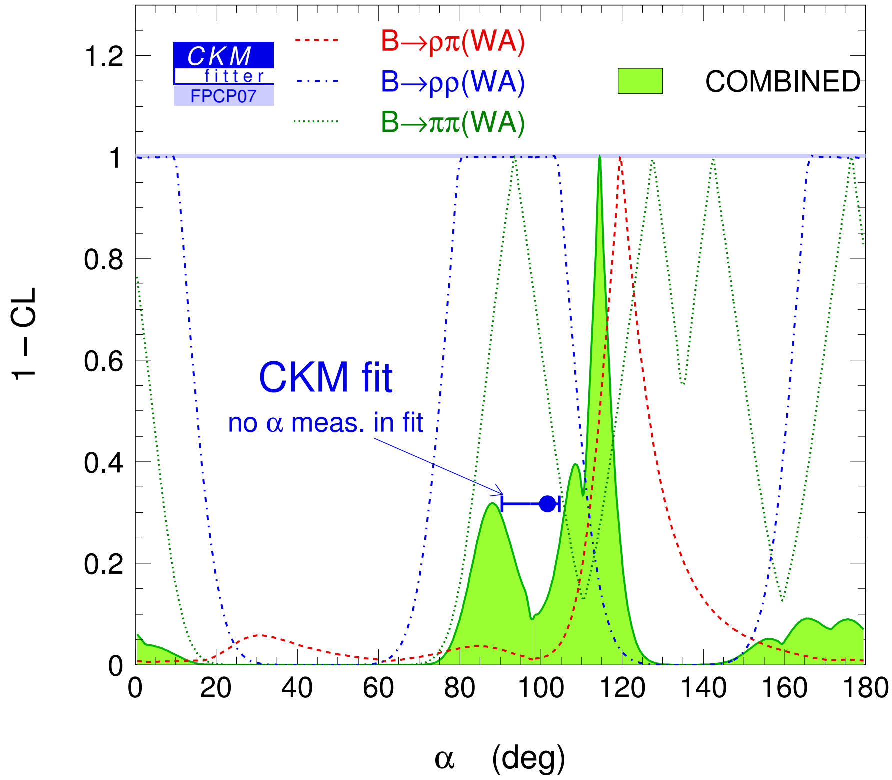

Figure 2.6: The unitarity angle α as measured by *BABAR* in $B^+ \to \rho\pi, \rho\rho$ and $\pi\pi$ decays.

2.5.1 Isospin Symmetry

Hadrons occur in families of particle with roughly equal masses, and within a particular family all of the particles have the same spin, parity, baryon number, strangeness, charm and beauty, but differ in their electric charge. For example, the K mesons, $K^+(494) = u\bar{s}, K^0(498) = d\bar{s}$ are part of the same family, and this behaviour highlights a symmetry that exists between u and d quarks. So, if the masses of these quarks were the same and the forces acting them are also equal, then replacing a u by a d quark would produce a particle with exactly the same mass. As the observed masses are actually slightly different, we know that this symmetry is not exact. However, the strong forces on u and d quarks are the same, even

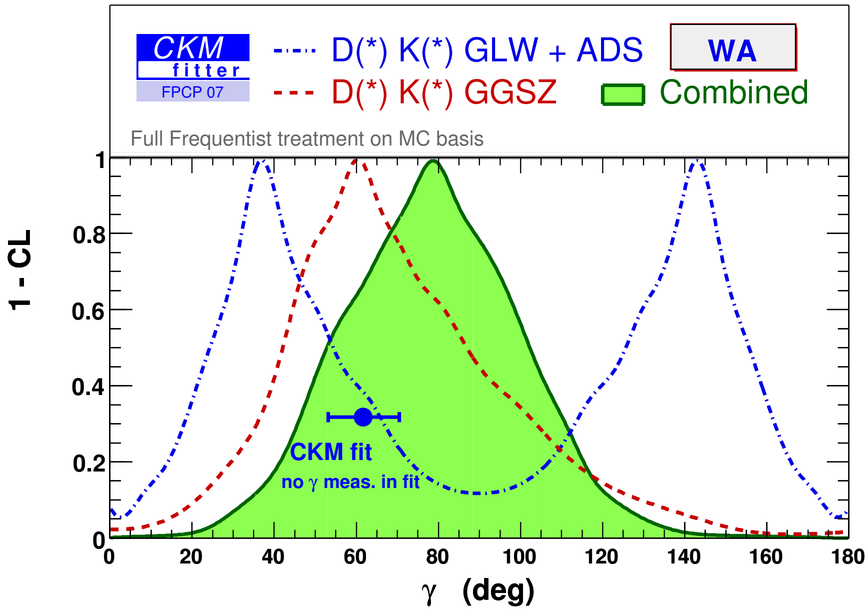

Figure 2.7: The unitarity angle γ as measured by *BABAR* in charm $B\overline{B}$ decays.

though the electromagnetic forces are different owing to the different charges. As the quark mass difference is small compared with typical hadron masses, and the electromagnetic forces are weak compared with the strong forces, then isospin symmetry is a good approximation, which immensely simplifies the interpretation of hadron physics. The families of particles are termed isospin muliplets.

To precisely describe isospin symmetry, three quantum numbers are formulated, these being conserved in strong interactions. The hypercharge is defined as:

$$Y \equiv B + S + C + \tilde{B} + T \tag{2.53}$$

where B, S, C B and T are the baryon number, strangeness, charm, beauty and truth. These all have the same values for the members of a particular isospin multiplet, hence so does the hypercharge. The second quantum number is defined by:

$$I_3 \equiv Q - Y/2 \tag{2.54}$$

Q being the electric charge. I_3 takes a different value for every member of a multiplet. Defining the maximum value within a multiplet as I, where:

$$I \equiv (I_3)_{max} \tag{2.55}$$

then it can be seen that all observed multiplets have exactly $(2I + 1)$ members with I_3 values:

$$I_3 = I, I - 1, \ldots, -I \tag{2.56}$$

which is analogous to the formalism for spin or angular momentum quantum numbers. I is termed the isospin quantum number and I_3 is the third component of isospin.

This formalism of isospin also leads to useful relations between the rates of reactions that involve members of the same isospin multiplets, and hence can be used to make predictions for branching ratios for resonance decays.

2.5.2 The Operator Product Expansion (OPE)

The OPE separates the non-perturbative long distance effects from the calculable short distance ones, this produces an *effective* theory [35]. This is reached at by performing an expansion of the decay amplitude in a small parameter k^2/m_W^2, k being the momentum transfer through the weak gauge boson propagator, W, itself having a mass of m_W. This expansion is valid provided that:

$$k < m_b \ll m_W \tag{2.57}$$

where m_b is the mass of the b quark.

Consider the decay $B^+ \to (a_1\pi)^+$ which at the tree level proceeds via the first diagram in Figure 2.8. The other two diagrams in this figure show the colour suppressed tree and gluonic penguin diagrams respectively. These are shown for $B^+ \to a_1^+\pi^0$, but the diagrams for $B^+ \to a_1^0\pi^+$ are identical except for the charges.

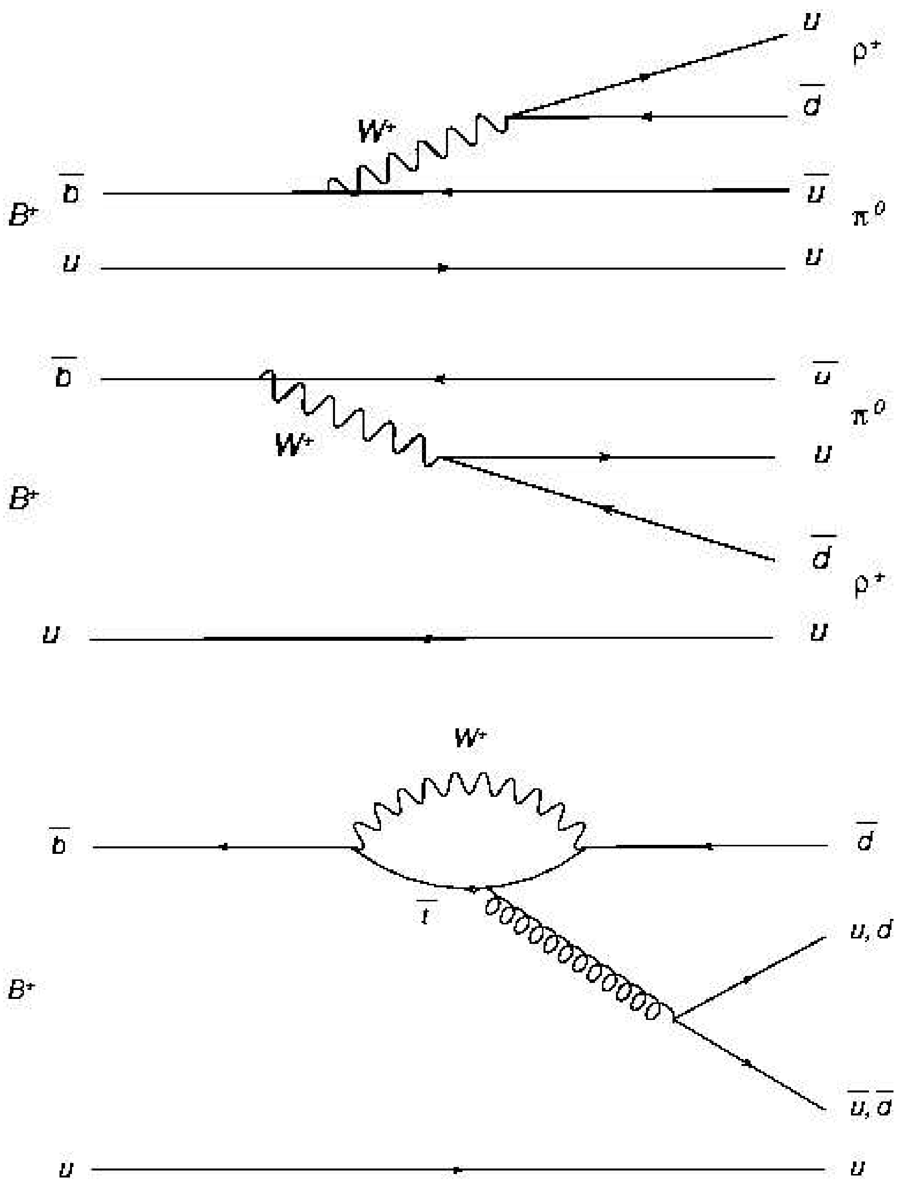

Figure 2.8: Feynman Diagrams for $B^+ \to a_1^+\pi^0$. The first is a tree diagram, the second is a colour suppressed tree diagram, and the third is a gluonic penguin diagram.

The amplitude for the first, tree-level diagram is:

$$\frac{G_F}{\sqrt{2}} V_{ub} V_{ud}^* (b^\dagger \gamma^\mu \gamma_L u)(u^\dagger \gamma_\mu \gamma_L d) \frac{m_W^2}{k^2 - m_W^2} \tag{2.58}$$

where γ_L denotes $(1 - \gamma_5)$ and $\frac{G_F}{\sqrt{2}} = \frac{g^2}{8m_W^2}$. Within the framework of OPE the non-local product of currents can be expanded into an infinite series of local operators as follows:

$$\begin{aligned} & -\frac{G_F}{\sqrt{2}} V_{ub} V_{ud}^* (b^\dagger \gamma^\mu \gamma_L u)(u^\dagger \gamma_\mu \gamma_L d) \left[1 + \frac{k^2}{m_W^2} + \cdots \right] \\ \approx & -\frac{G_F}{\sqrt{2}} V_{ub} V_{ud}^* (b^\dagger \gamma^\mu \gamma_L u)(u^\dagger \gamma_\mu \gamma_L d) = -\frac{G_F}{\sqrt{2}} V_{ub} V_{ud}^* Q_1 \end{aligned} \tag{2.59}$$

k is less than m_b and $m_b^2/m_W^2 \approx 10^{-3}$ and so everything except for the leading term can be neglected as corrections to the approximation.

So the W-boson has essentially been removed as a degree of freedom from the theory, which leaves a form similar to the Fermi theory of weak interactions. This method is sometimes called "integrating out" the degree of freedom, which refers to the formal path-integral method used to derive this.

Consider the QCD corrections to the decay $B^+ \to (a_1\pi)^+$. The gluons make the situation more complicated as they carry colour, which mixes the colour indices of the quarks and generates a new operator:

$$\sum_{a=1}^{8} (b_w^\dagger \gamma^\mu \gamma_L \lambda_{wz}^a u_z)(u_y^\dagger \gamma_\mu \gamma_L \lambda_{yx}^a d_x) \tag{2.60}$$

where λ^a are the Gell-Mann matrices and w, x, y and z are the colour indices. A Fierz transformation [36] can be applied to this operator to show that it is a combination of the operator in Eq. (2.59) and also that:

$$Q_2 = (b_x^\dagger \gamma^\mu \gamma_L u_y)(u_y^\dagger \gamma_\mu \gamma_L d_x) \tag{2.61}$$

Also, the gluons are able to transfer momentum between the quarks in both the initial and final states. If the gluon momentum is large, which are called "short distance" corrections, then perturbation theory can be applied due to the asymptotic freedom of QCD. However, this requires the introduction of a renormalisation scale μ to the operators. As the amplitude cannot have a dependence on μ the scale dependence must be cancelled in μ dependent coefficients, which are called Wilson coefficients, $C_n(\mu)$. These Wilson coefficients are calculated by matching the standard model and the effective theory at a scale $\mu \sim m_W$, which gives $C_n(m_W)$. The perturbative evolution of the coefficients down to the scale m_b is obtained by applying the renormalisation group to sum the large logarithms that appear.

Taking the QCD effects into account to obtain the tree level Hamiltonian requires that the two current-current operators Q_1 and Q_2 are each multiplied by Wilson coefficients:

$$\mathcal{H}_{eff} = \frac{G_F}{\sqrt{2}} V_{ub} V_{ud}^* (C_1(\mu) Q_1(\mu) + C_2(\mu) Q_2(\mu)) + \mathrm{h.c.} \tag{2.62}$$

There are four further operators within the effective Hamiltonian that may arise from Feynman diagrams with QCD corrections. These are known as QCD "penguin" diagrams, where the CKM factor in the Hamiltonian depends on which quark is present in the loop. Penguin operators differ from Q_1 and Q_2 in that the gluon coupling has both a left and right handed part and that there is sum over the possible $q\bar{q}$ pairs that the gluon may produce. If we define $\gamma_R = (1 + \gamma_5)$, then six operators can be defined that describe all of these corrections.

By making use of OPE, the calculable short distance contributions have been separated into the Wilson coefficients. The low momentum, long distance, QCD effects are contained within these operators. The next section will introduce a method used to approximate these effects, known as QCD Factorisation.

2.5.3 QCD Factorisation

The preceding section described how the calculable effects can be contained in the Wilson coefficients, and how the low momentum effects are taken into account with the hadronic matrix elements. Using lattice QCD techniques, the theoretical work on performing calculations of these elements is progressing but not yet reached the stage where calculations can be made for the decays such as the ones analysed here. In this section we will introduce an approximation of this known as Factorisation. A more detailed discussion of this topic can be found in [37].

A "naive" factorization approach has been widely used to estimate exclusive two-body B decay amplitudes [7]. This does give the correct order of magnitude of branching fractions in many cases, but it fails at predicting direct CP asymmetries as it assumes no strong rescattering. Naive factorization has been superseded by QCD factorization [38, 39, 40], which allows the calculation of two-body decay amplitudes from first principles. The limitations to the accuracy comes only from power corrections to the heavy-quark limit and uncertainties of theoretical inputs, such as quark masses, form factors and light-cone distribution amplitudes.

Factorisation says that there is a matrix element of the form

$$\langle a_1\pi \left| Q_n \right| B^+\rangle \tag{2.63}$$

which can be rewritten as a product of two elements as

$$\left\langle \pi \left| J_n^1 \right| 0 \right\rangle \left\langle a_1 \left| J_n^2 \right| B^+ \right\rangle \tag{2.64}$$

or as

$$\left\langle a_1 \left| J_n^1 \right| 0 \right\rangle \left\langle \pi \left| J_n^2 \right| B^+ \right\rangle \tag{2.65}$$

The effective weak Hamiltonian for charmless hadronic B decays is built up from a sum of local operators Q_i multiplied by short-distance coefficients C_i and products of elements of the quark mixing matrix, $\lambda_p^{(D)} = V_{pb}V_{pD}^*$, where $D = d, s$ can be a down or strange quark depending on the decay mode being considered, and $p = u, c, t$. By using the unitarity relation $\lambda_u^{(D)} + \lambda_c^{(D)} + \lambda_t^{(D)} = 0$ the effective Hamiltonian can be written:

$$\mathcal{H}_{eff} = \frac{G_F}{\sqrt{2}} \sum_{p=u,c} \lambda_p^{(D)} \left(C_1 Q_1^p + C_2 Q_2^P + \sum_{i=3}^{10} C_i Q_i + C_{7\gamma} Q_{7\gamma} + C_{8g} Q_{8g} \right) + \text{h.c.} \quad (2.66)$$

where $Q_{1,2}^p$ are the left-handed current-current operators arising from W-boson exchange, $Q_{3,...,6}$ and $Q_{7,...,10}$ are QCD and electroweak penguin operators, and $Q_{7\gamma}$ and Q_{8g} are the electromagnetic and chromomagnetic dipole operators as described in [41]. The effective Hamiltonian describes the quark transitions $b \to u\bar{u}D, b \to c\bar{c}D, b \to Dq\bar{q}$ with $q = u, d, s, c, b$, and $b \to Dg, b \to D\gamma$, as appropriate for decay modes with interference of "tree" and "penguin" contributions. The Wilson coefficients are calculated at next-to-leading order, consistent with the calculation of operator matrix elements.

Using the formalism of QCD factorization, the matrix elements of the effective weak Hamiltonian can be systematically calculated in the heavy-quark limit for particular two-body final states $M_1' M_2'$.

Figure 2.9 shows a graphical representation of this concept:

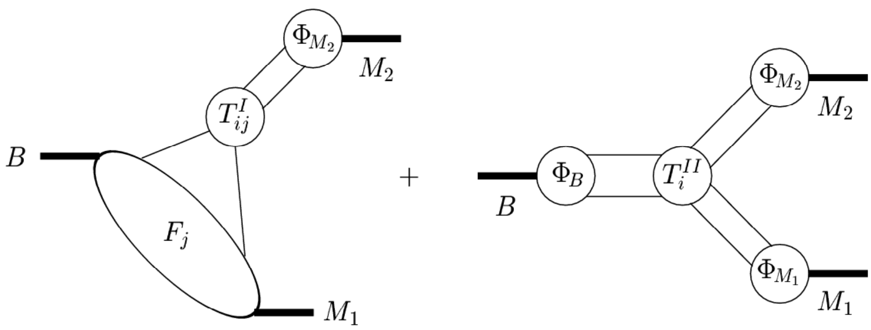

Figure 2.9: Graphical representation of QCD factorization.

Factorisation is used to calculate the operators need in OPE in terms of measurable quantities. In effect it splits these into individual elements, each of which can be calculated using non-perturbative techniques.

2.6 a_1 Decay Kinematics

The a_1(1260) has a mass of $1230 \pm 40\,\mathrm{MeV}/c^2$ and is broad with a width of 250 to $600\,\mathrm{MeV}/c^2$. $I^G(J^{PC})$ is equal to $1^-(1^{++})$ [18]. Several a_1 decays have been observed including both S-wave and D-wave $\rho\pi$ decay.

The rare decays $B^\pm \to a_1^\pm(1260)\pi^0$ and $B^\pm \to a_1^0(1260)\pi^\pm$ are expected to be dominated by $b \to u\bar{u}d$ contributions. The branching fraction for the neutral B meson decay, $B^0 \to a_1^\pm \pi^\mp$ has been measured to be $(33.2 \pm 3.8 \pm 3.0) \times 10^{-6}$ [5]. The Feynman diagrams corresponding to the charged B decays to $a_1\pi$ as discussed here are shown in Figure 2.8.

A theoretical calculation of the branching fraction of the neutral B decay mode exists by Bauer, Stech and Wirbel [7], of 38×10^{-6}. This is carried out within the framework of naive factorization and assumes $|V_{ub}/V_{cb}| = 0.08$. The branching fractions of the charged B decays to $a_1\pi$ are expected be half those of the neutral decays, so 19×10^{-6}. A more recent analysis, also using naive factorization and measured form factors predicts branching fractions in the range $(9-21) \times 10^{-6}$ and $(8-17) \times 10^{-6}$ for $B^\pm \to a_1^\pm\pi^0$ and $B^\pm \to a_1^0\pi^\pm$, respectively [8]. These modes are a possibly significant background to the decay $\rho\pi$, this is used to extract the weak interaction phase $\alpha \equiv \arg\left[-V_{td}V_{tb}^*/V_{ud}V_{ub}^*\right]$ of the Unitarity Triangle. Making a comparison between the theoretical predictions and measured branching fractions helps to verify the underlying theoretical hypotheses concerning factorisation and the $B \to a_1(1260)$ transition form factors. It can also lead to an improved determination of α, by contributing as a background to the $B^0 \to (\rho\pi)^0$ time dependent analysis, which will yield a measurement of α.

2.6.1 $a_1 \to 3\pi$ mass distribution

The decay $B \to a_1\pi, a_1 \to \rho\pi, \rho \to \pi\pi$ is a 4-body final state, and so ideally one would attempt a 4-dimensional Dalitz analysis in order to measure this and related decay branching fractions. However, as this is a first observation and the number of events in the sample was unknown, it was decided to treat this as a quasi 2-body $B^+ \to (a_1\pi)^+, (a_1 \to \rho\pi, \rho \to \pi\pi)$ decay.

The 2-body approach has a drawback in that it ignores interference between other modes, for example $B^+ \to a_2\pi$ may have a significant effect. However, for the purpose of a first observation this effect can be treated as a systematic error on the branching fraction measurement. As a comparison the Dalitz analysis would allow one to look at the interference and intermediate resonance states. As a 2-body decay, we can alternatively look at $a_1 \to 3\pi$ angular distributions, as they can be useful in distinguishing with other vector particles.

2.6.2 $a_1 \to 3\pi$ Spin Distributions

An important feature of this decay is the presence of a fast pion, π_1 in the B rest frame. The energy of this pion can be written as:

$$E_1 = \frac{m_B^2 + m_\pi^2 - m_a^2}{2m_B} \tag{2.67}$$

where m_B is the B meson mass, m_π is the pion mass and m_a is the a_1 mass.

This is useful to calculate as it shows that this pion has a distinctively large energy, which is useful to identify this *bachelor* pion. m_a is the apparent a_1 mass, largely in the region $(1.23 \pm 0.4)\,\mathrm{GeV}$ which implies $E_1 > 2.42\,\mathrm{GeV}$. There should be little confusion as to which pion is π_1 since it is unlikely that a second pion will also be so energetic. As a comparison, the combined energies of the other three pions are shown in Figure 2.10. These were obtained via an investigation using a_1 simulated events, which is discussed in Section 5.3.

A general four pion decay of a B meson is described by the following decay rate formula:

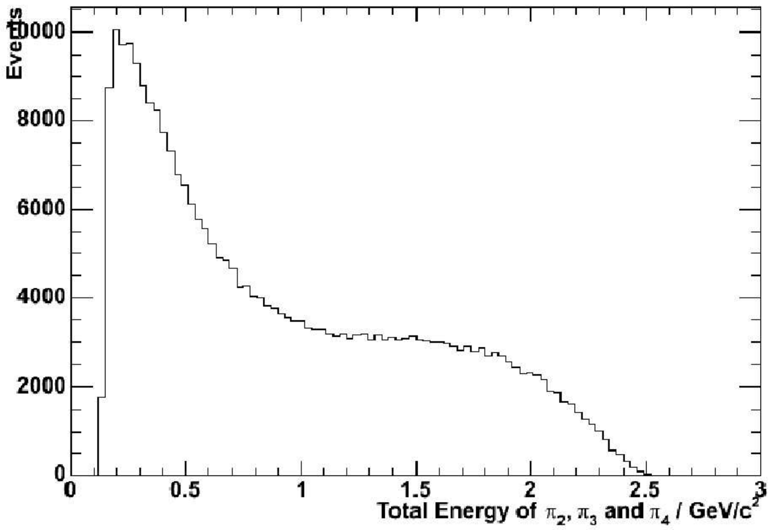

Figure 2.10: The energy distributions of π_2, π_3 and π_4 in the B rest frame

$$d\Gamma = \frac{|A|^2}{2E_B}\frac{d^3p_1}{2E_1}\frac{d^3p_2}{2E_2}\frac{d^3p_3}{2E_3}\frac{d^3p_4}{2E_4}\delta^4(p_1+p_2+p_3+p_4-p_B) \tag{2.68}$$

where p_i and E_i are the momenta and energies of each of the pions. From this expression it can be seen that there are four three momenta and four constraints from the delta function, thus any particular decay is specified by $8(4 \times 3 - 4)$ parameters. Since the B has no spin, the direction of any meson and in particular $\hat{p}_1$, the direction of π_1 is uniformly distributed in solid angle $d\Omega_1$, and an angle ϕ, which specifies rotations about $\hat{p}_1$ is also distributed uniformly. This leaves five variables that carry information beyond the fact that the B has no spin. In this section, some choices are suggested for these five variables, and these will be investigated using simulated a_1 decays in Section 5.3.

For the case of $B \to \pi_1 a_1$, $a_1 \to \pi_1\pi_2\pi_3$ there is a well defined intermediate state I with fixed invariant mass, unique spin, parity and helicity zero. The invariant amplitude A can then be expressed as the product of three terms: An invariant amplitude for the decay $B \to \pi_1 I$, an invariant amplitude for $I \to 3\pi$ and an invariant propagator linking the two. $|A|^2$ is then also the product of three terms.

The intermediate state, I decays to three pions and, in its rest frame the three momenta $\vec{p}_2, \vec{p}_3$ and $\vec{p}_4 = -(\vec{p}_2 + \vec{p}_3)$ lie in a plane and define a star like configuration, as shown in Figure 2.11.

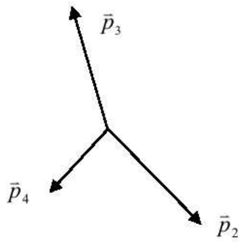

Figure 2.11: The intermediate state I, where $B \to \pi_1 I$, and its decay in a star-like configuration

The internal geometry of the star is completely specified by three variables, these being M_I and two Dalitz variables M_{23}^2 and M_{24}^2 for example. M_{34}^2 is not independent since:

$$M_{34}^2 + M_{23}^2 + M_{24}^2 - M_I^2 - 3m_\pi^2 = 0 \tag{2.69}$$

The orientation of the star is specified, as that for a rigid body, by three Euler angles. We characterise the orientation by the directions of three orthogonal unit vectors, here by $\hat{p}_2$ (where $\hat{p}$ denotes a unit vector), $\hat{q}_2$, with $\vec{q}_2$ a vector in the plane of the star but perpendicular to $\vec{p}_2$, and $\hat{n} = \hat{p}_2 \times \hat{q}_2$. Taking $\vec{q}_2$ to be:

$$\vec{q}_2 = (\vec{p}_3 - \vec{p}_4) - ((\vec{p}_3 - \vec{p}_4).\hat{p}_2)\hat{p}_2 \tag{2.70}$$

with $\hat{p}_2$ and $\hat{q}_2$ depending on the labelling of the mesons 1, 2 and 3, apart from its sign $\hat{n}$, which is perpendicular to the plane of the star and independent of the labelling. As a coordinate system, independent of the orientation of the decay of I, we take $\hat{p}_I(= -\hat{p}_1)$ to be the z axis, we take the x axis to be $\hat{x}$ with $\vec{x} = \vec{p}_B \times \hat{p}_I$, $\vec{p}_B$ the B lab momentum and $\hat{y} = \hat{p}_I \times \hat{x}$. To define an orientation we first need a reference one. Here I will consider two examples, the first being with $\hat{p}_2 = \hat{z}, \hat{q}_2 = \hat{x}$ and $\hat{n} = \hat{y}$:

$$\hat{p}_2 = (0,0,1) \quad \hat{q}_2 = (1,0,0) \quad \hat{n} = (0,1,0) \tag{2.71}$$

A general orientation is generated by rotation with Euler angles ϕ, θ, ψ with a rotation matrix:

$$R = e^{i\phi J_z} e^{i\theta J_y} e^{i\psi J_z} \tag{2.72}$$

which yields:

$$\begin{aligned}
\hat{p}_2 &= (\sin\theta\cos\phi, \sin\theta\sin\phi, \cos\theta) \qquad (2.73)\\
\hat{q}_2 &= (\cos\theta\cos\phi\cos\psi - \sin\phi\sin\psi, \cos\theta\sin\phi\cos\psi + \cos\phi\sin\psi, -\sin\theta\cos\psi)\\
\hat{n} &= (-\cos\phi\cos\theta\sin\psi - \sin\phi\cos\psi, -\sin\phi\cos\psi, -\sin\phi\cos\theta\sin\psi + \cos\phi\cos\psi,\\
&\quad \sin\theta\sin\psi)
\end{aligned}$$

Given the momentum vectors the angular configuration of the star is then determined by the relations:

$$\begin{aligned}
\cos\theta &= \hat{p}_I.\hat{q}_2 \qquad (2.74)\\
\sin\theta\cos\psi &= -\hat{p}_I.\hat{q}_2\\
\sin\theta\sin\psi &= \hat{p}_I.(\hat{p}_2 \times \hat{q}_2)\\
\sin\theta\cos\phi &= \hat{p}_2.\hat{x}\\
\sin\theta\sin\phi &= \hat{p}_2.(\hat{p}_I \times \hat{x})
\end{aligned}$$

$-1 < \cos\theta < 1$ and $0 < \theta < \pi$ so $\sin\theta$ can be taken as positive. The relations specify:

$$\begin{aligned}
&-\pi < \psi < \pi \qquad (2.75)\\
&-\pi < \phi < \pi
\end{aligned}$$

It can be seen that the angle ϕ is a rotation about $\hat{p}_I$, and should be uniformly distributed. θ and ψ are two angles that can be used with the three mass variables to generate the five significant variables mentioned above. However, these angles depend both on the labelling of mesons 2, 3 and 4 and on the reference orientation. For the case in which the intermediate state is an a_1 meson, and because of rotation invariance about the axis $\hat{p}_I$, its polarisation vector $\vec{\epsilon} = \hat{p}_I$, in the rest frame of I. The decay amplitude of a vector meson is overall rotation invariant, and there are three possible terms (a) $\vec{\epsilon}.\hat{p}_2 = \cos\theta$ (b) $\vec{\epsilon}.\hat{q}_2 = -\sin\theta\cos\psi$ and (c) $\vec{\epsilon}.(\hat{p}_2 \times \hat{q}_2) = \sin\theta\sin\psi$. Both (a) and (b) have intrinsic negative parity. (c) has intrinsic positive parity so only (a) and (b) are relevant for the pseudo vector a_1 decay to three pions.

With the intermediate state being an a_1 meson the B decay amplitude must be of the form:

$$\begin{aligned} A &= \alpha\hat{p}_2.\hat{p}_{a_1} - \beta\hat{q}_2.\hat{p}_{a_1} \\ &= \alpha\cos\theta + \beta\sin\theta\cos\psi \end{aligned} \tag{2.76}$$

where α and β are functions of M_I and the two Dalitz variables. The angular dependence is a feature specific to the a_1, and the details of the three pion decay of the a_1 are in the functions α and β.

$\cos\theta$, $\sin\theta\cos\psi$ and $\sin\theta\sin\psi$ are wave functions of a rigid body, like the star, rotating with total angular momentum 1 and spin projection 0 along the axis $\hat{p}_I$. For a given total angular momentum J and spin projection 0 there are in general $(2J+1)$ wave function, which are generally written in terms of the Wigner rotation matrices $D^J_{mm'}(\phi,\theta,\psi)$ but with $m = 0$, zero spin projection and hence no ϕ dependence. No dependence on ϕ is the signature of a helicity zero intermediate state. The Wigner rotation matrices can be written as:

$$\begin{aligned} D^J_{0,m'} &= d^J_{0,m'}(\theta)e^{-im'\psi} \qquad (2.77) \\ \cos\theta &= D^1_{00} \\ \sin\theta\cos\psi &= \frac{1}{\sqrt{2}}(D^1_{01} - D^1_{0-1}) \end{aligned}$$

$$\sin\theta\sin\psi \quad = \quad \frac{i}{\sqrt{2}}(D^1_{01} + D^1_{0-1})$$

The presence of intermediate states in the a_1 mass band but with spin parity other than 1^+ can be investigated in the angular distributions in $\cos\theta$ and ψ.

Here π_2 was chosen to define $\cos\theta$. Either π_3 or π_4 could have been chosen instead, and this would have been equivalent to a redefinition of the reference state. The same form would be obtained with α and β replaced by linear combinations. There could be sound physics reasons for choosing a particular pion as π_2. For example, in the decay $B^+ \to \pi^0 a_1^+(a_1^+ \to \pi^-\pi^+\pi^+)$, it is expected that the dominant mode is $a_1^+ \to \rho^0\pi^+(\rho^0 \to \pi^+\pi-)$. The π^- is unique and is likely to come from a ρ meson, so taking the π^- as π_2, then both π_3 and π_4 are π^+. Bose Einstein symmetry then implies that the Dalitz type function α will be symmetric and β antisymmetric if M^2_{23} and M^2_{24} are interchanged ($\vec{q}_2$ changes sign on the interchange of 3 and 4). The two π^+ can be labelled 3 and 4, for example by choosing $M^2_{23} < M^2_{24}$, or equivalently in the a_1 rest frame $E_3 < E_4$. To avoid double counting this restriction must also be applied on phase space.

2.6.3 Interference

Interference may occur between different decay modes that decay to the same final state. If a given intermediate state is a resonance it is useful to describe its dynamics using a relativistic Breit-Wigner formula and $\cos\theta_H$ by

$$\mathcal{M} \propto \frac{m_x\Gamma_x}{(m_x^2 - s) - im_x\Gamma_x} P_{s_x}(\cos\theta_H) \tag{2.78}$$

where m_x, Γ_x and s_x are the mass, width and spin of the resonance respectively. $\cos\theta_H$ is the cosine of the helicity angle, which will describe further in Chapter 5. The first term is a mass term, and the second relates to the helicity of the particle. P_{s_x} are Legendre polynomials describing spin distributions.

The $B^+ \to (a_1\pi)^+$ Dalitz plot may contain several intermediate modes, with all of these decaying to the same final state and quantum mechanically interfering with each other.

Examples of these are $B^+ \rightarrow \rho^+\rho^0, \pi^+\pi^-\pi^+\pi^0 or a_2\pi$. The $a_2\pi$ intermediate state is a prominent interference effect, and so within the confines of a two-body analysis will be treated as a systematic error on the branching fraction measurement. Analogously, the decay of the a_1 can proceed in more than one way to the same final state, for example $\rho\pi$, which is the channel considered here, but also to $\sigma\pi$, which also causes interference. This again will be treated as a systematic effect.

The interference of two states, each with amplitudes $\mathcal{M}_a$ and $\mathcal{M}_b$ and a relative phase δ can be shown to be of the following form:

$$
\begin{aligned}
|\mathcal{M}|^2 &= |\mathcal{M}_a + \mathcal{M}_b e^{i\delta}|^2 && (2.79)\\
&= |\mathcal{M}_a|^2 + |\mathcal{M}_b|^2 + 2\mathrm{Re}(\mathcal{M}_a\mathcal{M}_b^* \exp^{i\delta}) && (2.80)\\
&= |\mathcal{M}_a|^2 + |\mathcal{M}_b|^2 + 2\mathrm{Re}(\mathcal{M}_a\mathcal{M}_b^*)\cos\delta - 2\mathrm{Im}(\mathcal{M}_a\mathcal{M}_b^*)\sin\delta && (2.81)
\end{aligned}
$$

The effect of the interference is proportional to the area of overlap between resonances in the Dalitz plot. The orthogonality of the Legendre polynomials ensures that for resonances within the same mass pair having different spins, the effect of interference on the branching ratio will integrate to zero over $\cos\theta_H$, if the range of integration is symmetric about $\cos\theta_H = 0$. The distribution of events in the Dalitz plot will however still reflect this interference and an amplitude analysis for example, which takes into account this interference would be able to measure this.

Chapter 3

The BABAR Experiment

3.1 Introduction

The main purpose of *BABAR* is to measure CP violating asymmetries arising from neutral B mesons decaying to CP eigenstates. An important measurement is that of the CKM matrix element V_{ub} as this provides a constraint on the unitarity triangle. Other goals of the experiment include precise measurements of rare decays of charged and neutral B mesons, as well as charm, τ and two-photon physics. These factors determined the design of both the *BABAR* detector and PEP-II accelerator. Construction was finished in the summer of 1999 and data taking began shortly afterwards.

3.2 The PEP-II Accelerator

3.2.1 Overview

Figure 3.1 shows the PEP-II linear accelerator at the Stanford Linear Accelerator Center (SLAC) in California. This two mile long accelerator is the source of electrons and positrons for injection into PEP-II. Electron bunches are created by an electron gun at the far end of the linac, then stored in the north damping ring, before being accelerated in the linac to $9\,\mathrm{GeV}$, and injected into PEP-II's High Energy Ring (HER). Other electron bunches are produced, and then accelerated to $30\,\mathrm{GeV}$, and then collided with a stationary Beryllium target to produce positron bunches. These bunches are stored in the south damping ring, before being accelerated in the linac to $3.1\,\mathrm{GeV}$ and injected into PEP-II's Low Energy Ring (LER).

A complete description of the PEP-II machine can be found in [42]. The centre of mass energy was chosen to be $10.58\,\mathrm{GeV}$, as this energy corresponds to the $\Upsilon(4S)$ resonance, which almost always decays to $B\overline{B}$ pairs ($\approx 50\%$ $B^{+}B^{-}$, $\approx 50\%$ $B^{0}\overline{B}^{0}$ [43]) . The cross sections at this energy for fermion pairs are shown in Table 3.1. There are several categories of modes that can be produced from the $e^{+}e^{-}$ collisions at a centre of mass energy of $10.58\,\mathrm{GeV}$:

- $u\overline{u}$ $d\overline{d}$ $s\overline{s}$ $c\overline{c}$ continuum events are a large background and consist of quark anti-quark pairs, which in total have a large cross section. This background can also contain resonances.
- $\tau^{+}\tau^{-}$ pairs are produced copiously in *BABAR*, with a cross section similar to B production. These modes allow the study of flavour violation.
- $\mu^{+}\mu^{-}$ dimuon pairs are very useful for tracking studies and are used to calculated the luminosity via the number of $B\overline{B}$ pairs, as their cross section is well known and well simulated. They are in addition used for SVT alignment and tracking studies.
- $e^{+}e^{-}$ bhabha pairs are produced at a very high rate as they have a large cross section, however most of these travel down the beam pipe and not through the detector. Two track events aren't a background to the analysis considered here, as I am looking at hadrons, the final products of which are easily distinguishable from events with just two tracks.

For about 10% of the time, the accelerator is run at a CM energy $\sim 40\,\mathrm{MeV}$ lower, which is below the $B\overline{B}$ production threshold. This offpeak mode is used to study backgrounds from continuum events ($e^+e^- \to c\overline{c}$, $s\overline{s}$, $u\overline{u}$, $d\overline{d}$), as Monte Carlo is less reliable for continuum. The MC doesn't simulate all of the possible decays and the amplitudes of the decays may not be correct, whereas in data these conditions are satisfied. The design luminosity goal for PEP-II was $3 \times 10^{33}\,\mathrm{cm}^{-2}s^{-1}$, and as of the time of writing it has reached $\sim 12 \times 10^{33}\,\mathrm{cm}^{-2}s^{-1}$. This high luminosity, coupled with very clean events when compared with a hadronic collider, enables many rare B decays to be studied.

Figure 3.1: The linac injection system and the PEP-II storage rings.

$e^+e^- \to$	**Cross-section (** nb**)**	**Production Rate (** Hz**)** **At Design Luminosity** **(** $3.0 \times 10^{33}\,\mathrm{cm}^{-2}\mathrm{s}^{-1}$**)**
$b\overline{b}$	1.05	3.2
$c\overline{c}$	1.30	3.9
$s\overline{s}$	0.35	1.1
$u\overline{u}$	1.39	4.2
$d\overline{d}$	0.35	1.1
$\tau^+\tau^-$	0.94	2.8
$\mu^+\mu^-$	1.16	3.5
e^+e^-	~ 40	~ 120

Table 3.1: e^+e^- production cross-sections at CM energy $10.58\,\mathrm{GeV}$ [21]. For e^+e^- scattering, the cross-section given applies only within detector coverage.

Flavour tagging on one of the B mesons can be utilised as they are produced and oscillate coherently, which means the B^0 and $\overline{B}^0$ are always opposite flavours. When one of the B decays, the flavour of the other one can be determined. This is very important for time dependent measurements. Another essential measurement is that the distance between the B meson decays vertices is measurable. This is achieved by having asymmetric beam energies, and so giving the $\Upsilon(4S)$ system a relativistic boost. The $\Upsilon(4S)$ energy is just above the $B\overline{B}$ production threshold, so the B mesons are produced almost at rest in the CM frame. The B mesons inherit the relativistic boost of the $\Upsilon(4S)$ and this boost has a value of $\beta_z = 0.56$ in the direction of the e^- in the detector (laboratory) frame. This corresponds to the B travelling around $\frac{1}{4}\,\mathrm{mm}$ before it decays, and this allows the distance to be measured, which is possible with the vertex resolution. The e^- are stored in the high energy ring (HER) and the e^+ in the low energy ring (LER). The energy of the HER is $9\,\mathrm{GeV}$, and the energy of the LER is $3.1\,\mathrm{GeV}$.

Precision measurements of CP quantities and branching fractions require a very large data set. Tagging efficiencies for time dependent analyses are $\approx 30\%$, and B decays to CP eigenstates are only a subset of B decays. For example, in the case of charm decays, the branching ratios are $\sim 10^{-4}$ and for charmless decays are $\sim 10^{-5} - 10^{-6}$. This requires there to be minimal downtime and for PEP-II to deliver extremely high luminosities. Also, the detector must operate with very high efficiency.

3.2.2 The Interaction Region

To minimise the beam-beam interference, the beams are divided into a large number of low charge bunches, with the inter-bunch distance bunch being small. There are around 10^{10} particles per bunch. This helps achieve the high luminosities that the physics program requires. However, this means that secondary collisions would occur close to the interaction point (IP). To avoid these secondary collisions, the beams are horizontally displaced from one another until very close to the interaction point (IP). Figure 3.2 shows a plan view of the interaction region.

Sets of quadrupole magnets are used to focus the beams so they collide head on. The HER ring is focused with sets of quadrupole magnets Q4 and Q5, as shown in Figure 3.2. Q2 focuses the LER ring, and Q1 is a final focus which affects both beams. Q1 magnets are permanent magnets, and partially enter the detector volume. Q2, Q4 and Q5 are made from iron, and are located entirely outside the detector volume. A disadvantage of this

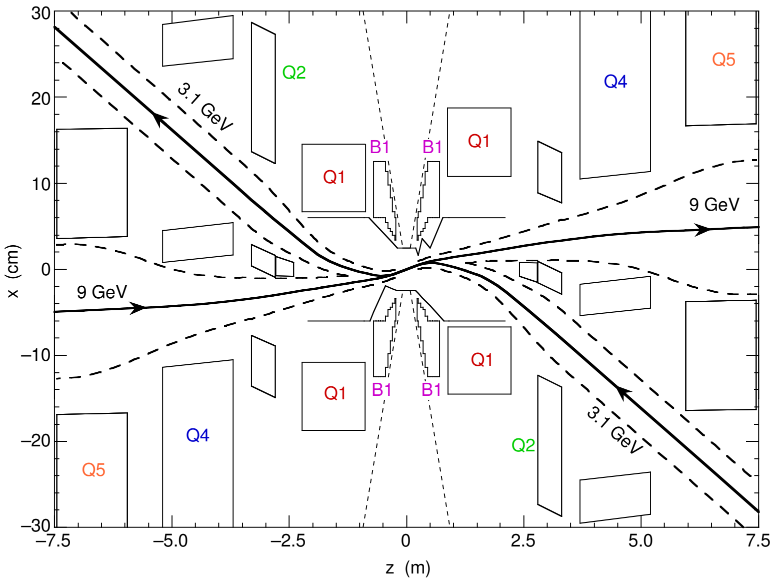

Figure 3.2: The PEP-II interaction region, with exaggerated vertical scale.

approach is the synchrotron radiation that is emitted as the beams are diverted by the magnets. This affects background conditions, and potentially cause long term damage to detector components. The Belle experiment [26] in Japan uses an alternative approach in which the beams are collided at an angle of $1.3° = 22\,\mathrm{mrad}$,thereby avoiding the magnets and the synchrotron radiation. At the time of construction of *BABAR* this method was untried and therefore was deemed too risky to pursue.

3.2.3 Machine Backgrounds

Machine backgrounds can degrade physics measurements by causing high occupancy in the detector systems. The trigger rate is adversely affected, so that deadtime increases, meaning desirable physics events are lost. Backgrounds also cause radiation damage, through both long and short term exposures.

Synchrotron radiation is a large problem in PEP-II, due to the complicated optics near the IP, although by design the majority of the synchrotron radiation from the extra bending magnets passes through the detector without interaction.

Beam particles undergoing bremsstrahlung or coulombic interactions with gas molecules in the beam pipe may collide with the storage rings, causing an electromagnetic shower upon impact. This background is dealt with by ensuring a good vacuum in the beam pipe close to the IP. Beam-beam interactions can also cause particles to be lost from the beam, and then possibly interact with gas molecules or the beam pipe.

Another source of background is from radiative Bhabha scattering events. These are caused by an electron or positron hitting material a short distance from the IP, and causes electromagnetic showers that enter the detector. This background scales approximately linearly with luminosity and so has become more prominent as the experiment has progressed. Beam-beam and beam-gas interactions are more reliant on the bunch currents as opposed to the luminosity, so this means the overall machine background is not quite linearly dependent on the luminosity. The luminosity has been increased by changing beam tube parameters, the currents have gradually been increased, and there has also been the implementation of trickle injection.

3.2.4 Trickle Injection

So far PEP-II has performed exceptionally well. Both instantaneous and integrated design luminosity design levels were achieved during the first year of operation, and this has continued to improve since.

Trickle injection is a more recent development in the operation of the PEP-II machine. Originally, the mode of operation of the accelerator was to first fill both beams, and then to continue collisions until the luminosity reached a defined low limit. Then the beams were topped up from the SLAC linac. This method protected the detector from backgrounds that occur during injection, as the various systems' voltage was ramped down. However, in terms of integrated luminosity, this is not optimal.

An alternative is trickle injection, which continuously injects into the rings at a very low rate. This leads to increased luminosity delivery efficiency, but also to higher machine backgrounds. The machine backgrounds present technical difficulties for both the accelerator and the detector teams.

Tests with trickle injection were first carried out in November 2003, when the LER was continuously injected. The backgrounds and data taken was compared with the normal operation. A short inhibit window was set immediately after a bunch was injected, just when the background is high, so this prevents the Level-1 Trigger accepting high background events in that bunch. The backgrounds were found to be manageable, and the data compared well, so in December 2003 the default mode of data taking was switched to LER trickle injection. During 2004, tests were carried out with the HER undergoing trickle injection instead of the LER, and then with both rings. From March, the default mode was for both rings to be injected. Figure 3.3 shows the increase in daily integrated luminosity since the beginning of the experiment. The large increase at the beginning of 2004 can be attributed to when PEP-II started running in trickle injected mode.

3.2.5 Performance

The design luminosity was achieved within the first year of running and subsequently trickle injection lead to a dramatic increase in performance. Table 3.2 shows some performance records of the PEP-II machine.

3.3 The BABAR Detector

A full description of the *BABAR* detector can be found in [44]. The main physics goals drove the design of both the accelerator and the detector, but also important were cost factors, and maximisation of reliability.

To satisfy its primary physics goals, the following factors were important in designing the detector:

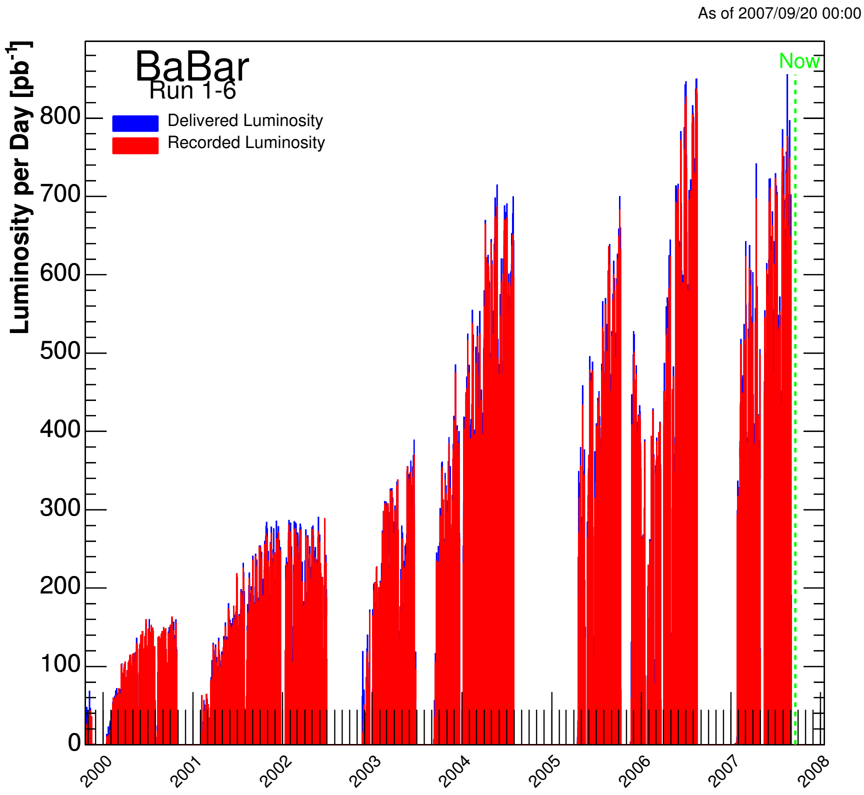

Figure 3.3: PEP-II integrated luminosity per day.

- The angular acceptance of the detector in the CM frame must be uniform and as large as possible. This is achieved by giving the detector an offset of $0.37\,\mathrm{m}$ from the IP, in the direction of the HER, and also making the detector asymmetric.
- Both charged and neutral particles must have high reconstruction efficiencies
- Charged particles must have both good position and momentum resolution, specifically over the momentum range $60\,\mathrm{MeV}/c - 4\,\mathrm{GeV}/c$.
- Neutral particle must have good energy and angular resolution, over the energy range $20\,\mathrm{MeV} - 4\,\mathrm{GeV}$. This particularly important for the detection of π^0 and η particles.

Parameter	**Design**	**Best Achieved**	**Date Achieved**
HER Current (A)	0.75	1.875	August 16, 2006
LER Current (A)	2.14	2.900	August 16, 2006
Luminosity ($10^{33}\ \mathrm{cm}^{-2}\mathrm{s}^{-1}$)	3.000	12.069	August 16, 2006
Luminosity (pb^{-1}/8 hour shift)	—	339.0	August 16, 2006
Luminosity (pb^{-1}/day)	130.0	858.4	August 19, 2007
Luminosity (fb^{-1}/week)	—	5.137	August 12-18, 2007
Luminosity (fb^{-1}/month)	—	19.732	August 2007
Total Delivered Luminosity	500 fb^{-1}		

Table 3.2: PEP-II machine performance records, as of August, 2007. Total delivered luminosity is on- and off-resonance data.

- For the measurement of the difference in decay times of the two B mesons, there must be excellent vertex resolution in the z direction. There must also be good resolution in the transverse direction for reconstruction of secondary charm and τ vertices.
- For flavour tagging and to separate some final states, for example K^+ π^- and π^+ π^- there must be excellent particle identification for e, μ, π, K and p for a large momentum range.
- There may be high background conditions due to high luminosities, and the detector must be able to function with these.
- A reliable, efficient data acquisition system, which must be able to deal with the amount of data produced at these high luminosities.
- A trigger must be efficient and able to reduce the rate of events to a manageable level, whilst not losing interesting physics events.

The above conditions were met by the design of the detector, whilst also satisfying real world demands, especially those of minimising costs and maximising reliability. The final design as shown in Figures 3.4 and 3.5 is built as a series of five sub-detectors and a solenoidal superconducting magnet. From the centre these sub-detectors are:

- Silicon vertex tracker (SVT). This gives precise positional information for charged tracks, and actually provides the only tracking for very low momentum ($p_T \leq 120\,\mathrm{MeV}/c$) charged particles.
- Drift chamber (DCH). This provides the primary charged particle momentum measurement, and also aids particle identifications through energy loss measurements.
- Detector of Internally Reflected Cerenkov radiation (DIRC). This is designed to provide charged hadron identification.
- Electromagnetic calorimeter (EMC). The EMC provides neutral electromagnetic particle identification, as well as for electrons and neutral hadrons.
- Superconducting Coil. This provides a $1.5\,\mathrm{T}$ solenoidal magnetic field, which covers the inner four sub-detectors.
- Instrumented Flux Return (IFR). This provides muon and neutral hadron identification.

3.3.1 The BABAR Co-ordinate System

BABAR uses a right hand co-ordinate system, with the origin located at the IP. The drift chamber lies along the z-axis, in the direction of the HER. The y-axis is directed vertically upwards, and the x-axis horizontally out from the centre of the PEP-II ring. The standard spherical polar co-ordinate system is used to define the polar (θ) and azimuthal (ϕ) angles. This is shown in Figure 3.5.

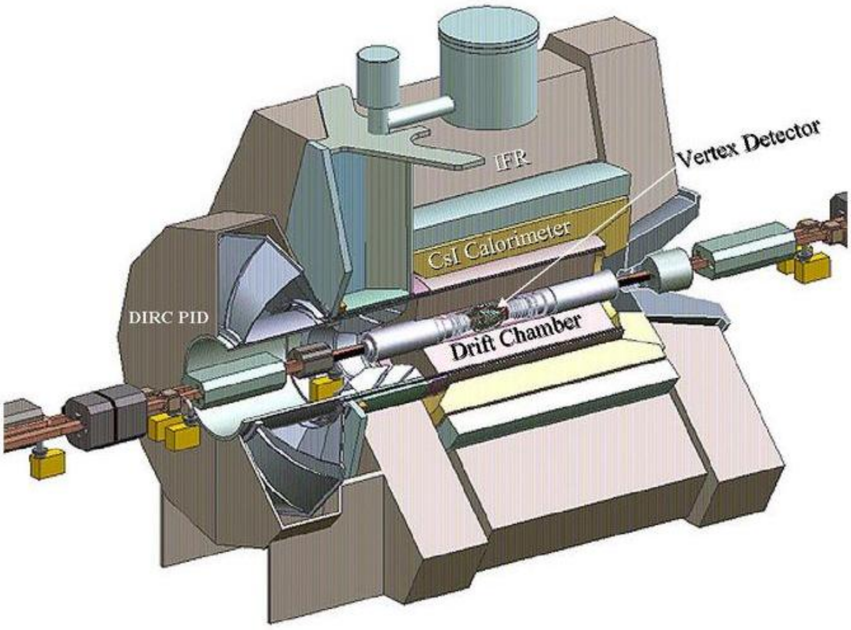

Figure 3.4: Layout of the *BABAR* detector.

3.4 The Silicon Vertex Tracker (SVT)

3.4.1 SVT Physics Requirements

The main purpose of the SVT is to make measurements of the z positions of tracks. This is to provide good measurements of the two B decay vertices, which are important for time dependent CP violation studies.

There must be excellent tracking efficiency in the SVT, for tracks with transverse momentum (p_T) less than $120\,\mathrm{MeV}/c$, as these are not detected reliably using the DCH, which is the main tracking system. An example are slow pions, which come from the decay of the very common D^* particles. The SVT measures the energy loss ($\mathrm{d}E/\mathrm{d}x$) of particle, which have momenta less than $700\,\mathrm{MeV}/c$.

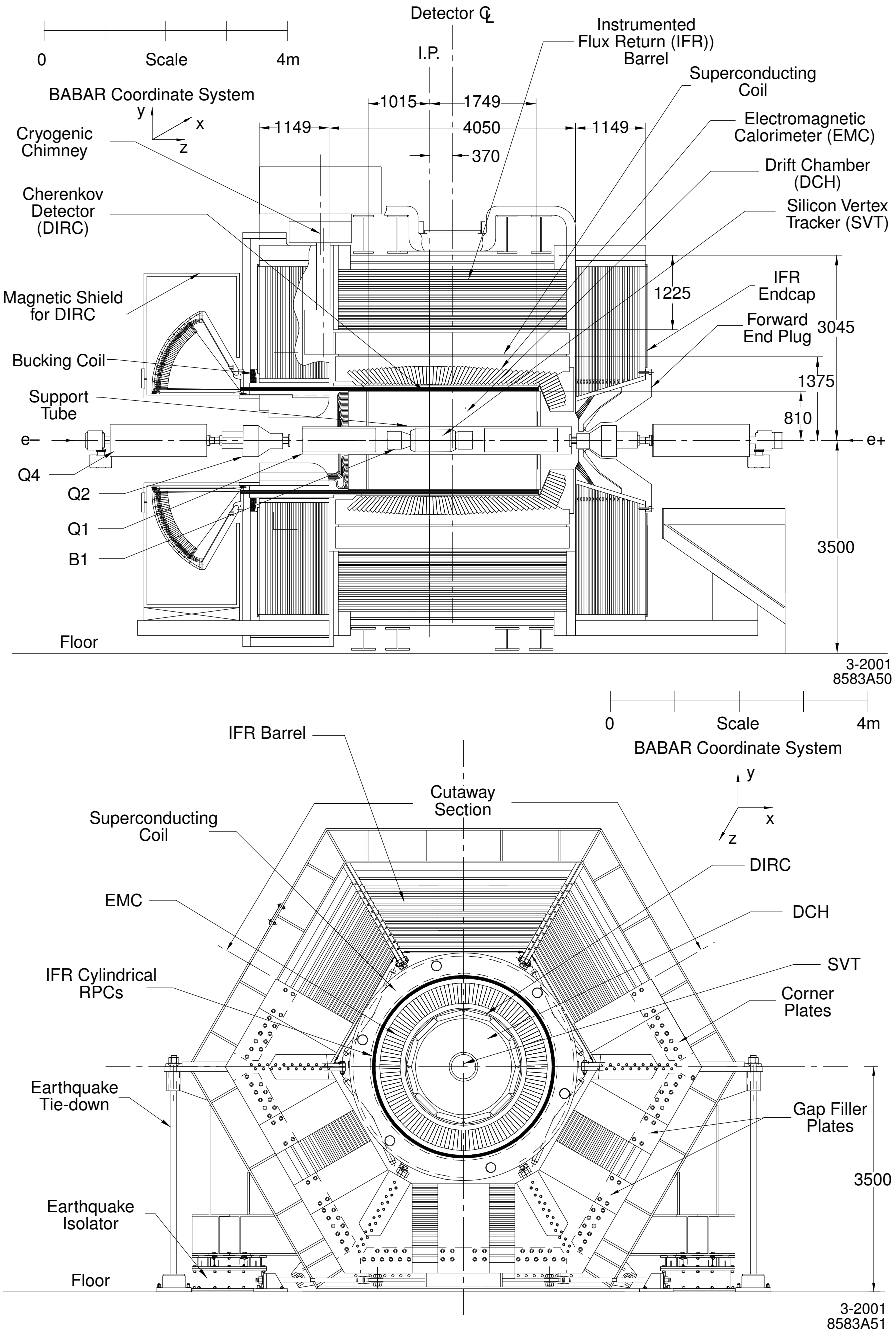

Figure 3.5: The *BABAR* detector longitudinal and end views.

3.4.2 SVT Design

The SVT is an symmetric p-n junction semi-conductor detector. There is excellent resolution due to its fine granularity. Also, these type of detectors are very small and compact.

When an ionising particle penetrates the detector, this creates electron-hole pairs along its track. The number of these pairs is proportional to the energy loss of the charged particle. By applying an external field, this makes the electrons and holes drift towards oppositely charged electrodes. These collect the charge, and this gives rise to a current pulse, the integral of this being the total charged that was generated from the incident particle.

There are some external factors that affect the SVT design. The design of the PEP-II interaction region places limits on the acceptance of the SVT. The SVT polar angle (θ) acceptance is $20.1°$ to $150.2°$, which covers 90% of the solid angle in the CM frame. The design must also be able to deal with the high levels of radiation the SVT will receive throughout its lifetime. The design limit was placed at $2\,\mathrm{MRad}$, with the instantaneous limit being up to $1\,\mathrm{Rad/ms}$.

Figure 3.6 shows how the design consists of five layers of silicon strip sensors, which are double sided. These are divided azimuthally into modules. The inner three layers each have 6 modules, which are tilted by $5°$ in ϕ to make them slightly overlap. This aids with the alignment, and also provides complete coverage. The outer two layers, 4 and 5, have 16 and 18 modules respectively. They are arch shaped in the longitudinal plane. This can be seen in Figure 3.7, and increases the angular coverage as well as minimising the amount of material that tracks pass through. Because of the arch design, the overlapping has to be achieved by splitting the modules into two sub-layers, which are at slightly different radii. The inner side of the strips contains sensors that give z measurements, whilst the outer side sensors give ϕ measurements. The inner layers, 1 and 2 primarily measure the track angle, whilst the outer two layers, 4 and 5 are mainly used for alignment with the DCH. The 3rd layer provides momentum information for low momentum tracks.

Each module is split into forward and backward halves in z, each being read out by

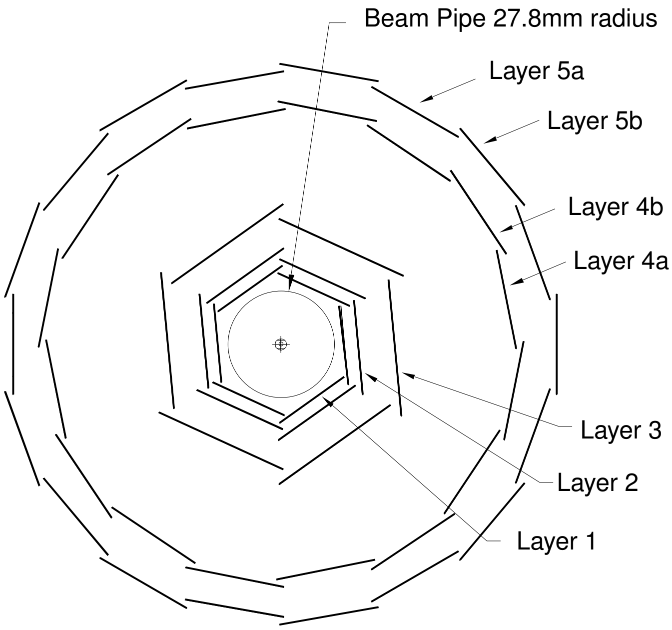

Figure 3.6: End on view of the SVT showing the five layer structure.

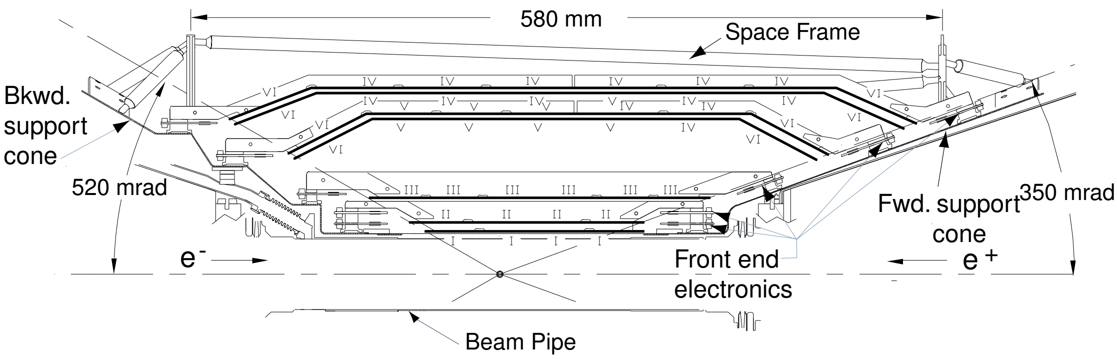

Figure 3.7: Side view of the SVT showing the five layer structure.

electronics that are outside the detector acceptance. A time over threshold (TOT) technique is used by the readout to determine the total charge deposited within a strip. The signals from the strips are simplified and shaped, then compared with a threshold depending on background conditions. A large range of deposited charge can be covered as the TOT has a logarithmic dependence on charge. Each TOT measurement supplies positional information, and also a $\mathrm{d}E/\mathrm{d}x$ measurement. The final measurement of $\mathrm{d}E/\mathrm{d}x$ is taken as the mean of the lowest 60% of the individual measurements from sensors. This truncated mean is used as $\mathrm{d}E/\mathrm{d}x$ is distributed according to a Landau distribution.

Both local and global alignment of the SVT are essential for achieving the best position and momentum resolution. Global alignment is the alignment of the whole system with respect to the rest of the detector. Local alignment is more complicated, and is the internal alignment of the modules within the SVT. This is only needed after detector access times, and is carried out using very high momentum two-prong events. These are mainly $e^+e^- \to \mu^+\mu^-$, and cosmic ray events. Global alignment is carried out for each run, by fitting tracks with sufficient numbers of SVT and DCH hits. These fits are run twice, the first time using just the DCH information, but then again using the SVT information. By minimising the difference between the track parameters from these two fits, the alignment parameters are obtained. A *rolling calibration* was carried out from *BABAR* Runs $1-3$, which means the constants were obtained from one run by using those from the previous one. From the start of Run 4, the new procedure is to use a small sample of events from a run to calculate the calibration constants. These are used to reconstruct the rest of the events in the run.

3.4.3 SVT Performance

The spatial resolution of the SVT hits can be calculated by comparing the hit position with the trajectory of the track, in the plane of the sensor. Two-prong, high momentum events are used for this, and also the track is refitted without the layer being studied. To obtain the git resolution, the uncertainty on the track trajectory is subtracted from the width of the residual distribution. For all angles, this is found to be better than $40\,\mu\mathrm{m}$ for the first three layers. This means that the B decay vertex resolution is better than $70\,\mu\mathrm{m}$. By using data, the SVT tracking efficiency is measured to be 97%, this excludes defective readout sections, accounting for less than 5% of the total. For minimum ionising particles (MIPs), the $\mathrm{d}E/\mathrm{d}x$ resolution is found to be 14%. This makes it possible to have a separation of 2σ of pions and kaons, for momenta up to $500\,\mathrm{MeV}$, and of kaons and protons up to $1\,\mathrm{GeV}/c$.

3.5 The Drift Chamber (DCH)

3.5.1 DCH Physics Requirements

This is the main charged particle detector in BABAR. It makes precise measurements of the momenta of particles and angles of tracks, for particles with momenta greater than $120\,\mathrm{MeV}/c$, and with transverse momentum in the range $0.1 < p_T < 5.0\,\mathrm{GeV}/c$. The DCH also plays a key role in extrapolating tracks into the DIRC, EMC and IFR.

The momentum resolution must be $\sigma_{p_T}/p_T < 0.3\%$, and the spatial hit resolution must be better than $140\,\mu\mathrm{m}$, so that B and D decays can be exclusively reconstructed. The DCH also provides the main reconstruction information for K_S^0 particles that decay outside the SVT. These are important as they feature in many important modes for time dependent CP asymmetry studies, for example $B^0 \rightarrow J/\psi K_S^0$. For these, the longitudinal position must be measured with a resolution better than $1\,\mathrm{mm}$. For particles with momenta between $300\,\mathrm{MeV}/c$ and $700\,\mathrm{MeV}/c$, the DIRC is unable to provide adequate particle identifications, and so the DCH becomes important for these particles, as well as for areas that fall outside the DIRC acceptance. For this, the DCH must provide $\mathrm{d}E/\mathrm{d}x$ measurements with a minimum resolution of about 7%. The DCH feeds its tracking and timing data to the Level 1 Trigger every $269\,\mathrm{ns}$.

3.5.2 DCH Design

Figure 3.8 shows a longitudinal section of the DCH. This is a $2.8\,\mathrm{m}$ long cylinder, which is placed asymmetrically around the IP so to increase the coverage in the forward direction. The inner radius of the chamber is $23.6\,\mathrm{cm}$, and the outer radius is $80.9\,\mathrm{cm}$. The chamber is filled with a gas mixture of low mass, which is made up of helium and isobutane, mixed together in the ratio of 4:1. This is to provide good spatial and $\mathrm{d}E/\mathrm{d}x$ resolution and a short drift time, and to minimise multiple scattering. To prolong the chamber lifetime, a small amount of water is added, around 0.3%.

The actual detection mechanism is made up of 7104 hexagonal drift cells, each of these typically being $1.2 \times 1.8\,\mathrm{cm}^2$ in size. A cell is a single $20\,\mu\mathrm{m}$ diameter gold plater tungsten-rhenium sense wire, which is surrounded by six $120\,\mu\mathrm{m}$ or $80\,\mu\mathrm{m}$ gold plater aluminium field wires. A high voltage of $1960\,\mathrm{V}$ is applied to the sense wires, and the field wires are grounded, thereby creating a field with approximate circular symmetry over the majority of the cell. The cells form circular layers around the DCH axis, a superlayer being formed from a group of four layers. In the complete DCH there are ten superlayers. Each adjacent layer is offset slightly, and this allows left-right ambiguities to be resolved within a superlayer, even if one out of the four signals is missing. This offsetting can be seen in Figure 3.9. It also permits local segment finding. Also six of the ten superlayers are angled acutely to the z-axis so to permit longitudinal position calculation.

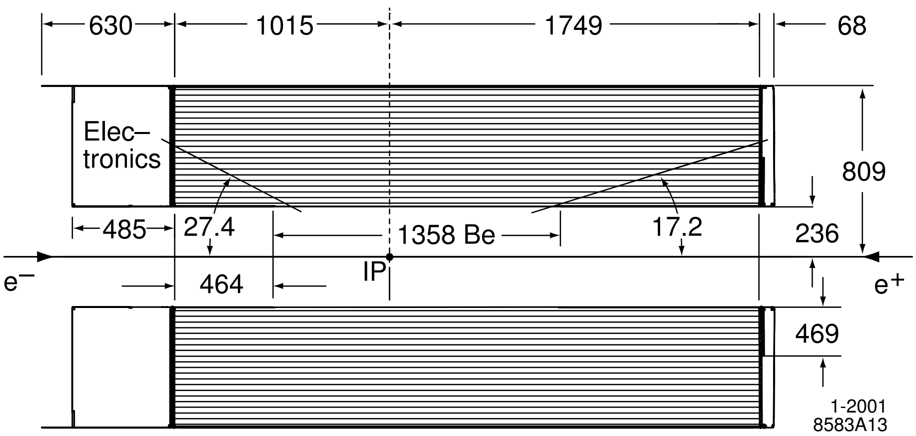

Figure 3.8: Side on view of the DCH.

Charged particles ionise the gas mixture within a drift cell, producing electrons. These are accelerated along the electric field towards the sense wire. This further ionises the gas causing a charge avalanche, which for the design voltage of $1960\,\mathrm{V}$ is a gain of 5×10^4. The detection of the leading edge of the signal and subsequent digitisation to within $1\,\mathrm{ns}$ means that the drift time and positional information can be determined. $\mathrm{d}E/\mathrm{d}x$ of the track is determined using the total charge deposited. A truncated mean of the lowest 80% of the individual energy loss measurements is used.

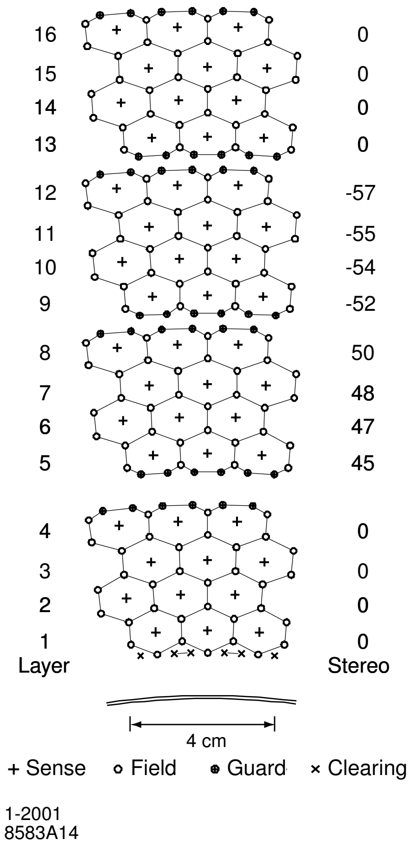

Figure 3.9: DCH cell layout for the first four superlayers. The last column shows the stereo angle of the layers.

3.5.3 DCH Performance

To calibrate the drift time to track distance relation, high momentum two-prong events are used. This calibration is carried out for each cell, where the best fit to the particular track is calculated, omitting the cell being calibrated. The drift distance is estimated by calculating the distance of closest approach of the best fit. $\mathrm{d}E/\mathrm{d}x$ measurements must also be calibrated, which then removes biases from multiple sources including those from gas pressure changes and temperature.

The track reconstruction efficiency is shown in Figure 3.10. This is calculated by comparing the number of SVT track falling within the DCH acceptance with the total number

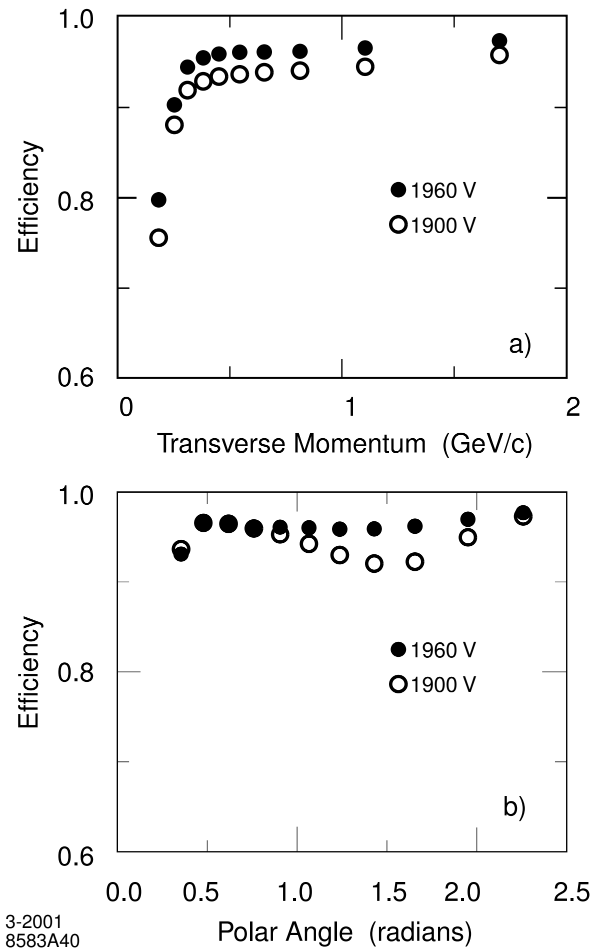

Figure 3.10: Tracking efficiency for the DCH shown as a function of p_T (top) and of polar angle (bottom). Points are shown for two voltages using in *BABAR* run 1, $1960\,\mathrm{V}$ and $1900\,\mathrm{V}$.

of DCH tracks, and this is then corrected for fake SVT tracks. Shown are the variations of efficiency with both transverse momentum and polar angle. Two operating voltages are shown, the design voltage of $1960\,\mathrm{V}$ and also for $1900\,\mathrm{V}$. The reason for this change is that a small section of the DCH was damaged during commissioning, so for an early part of *BABAR* Run 1 a reduced voltage was used in the chamber. After this *BABAR* Run, the operating voltage was consistently $1930\,\mathrm{V}$. Both at design voltage and at $1930\,\mathrm{V}$, the average tracking efficiency, as calculated using the method described above, is $(96 \pm 1)\%$.

Figure 3.11 shows the variation of $\mathrm{d}E/\mathrm{d}x$ as a function of track momentum. The Bethe-Block [18] predictions are overlaid. These are calculated from control samples of each of the labelled particle types. They demonstrate that a good $K\pi$ can be obtained for momenta up to $0.6\,\mathrm{GeV}/c$. For e^+e^- events, the $\mathrm{d}E/\mathrm{d}x$ resolution is 7.5%, this being almost as good as the design goal of 7.0%.

The transverse momentum energy resolution can be determined from cosmic ray muons. Using this method, it is found to follow the following relation:

$$\sigma_{p_T}/p_T = (0.13 \pm 0.01)\% \cdot p_T + (0.45 \pm 0.03)\% \tag{3.1}$$

where p_T is the transverse momentum, in units of GeV/c. This is found to be in good agreement with Monte Carlo simulations, and is close to the design resolution.

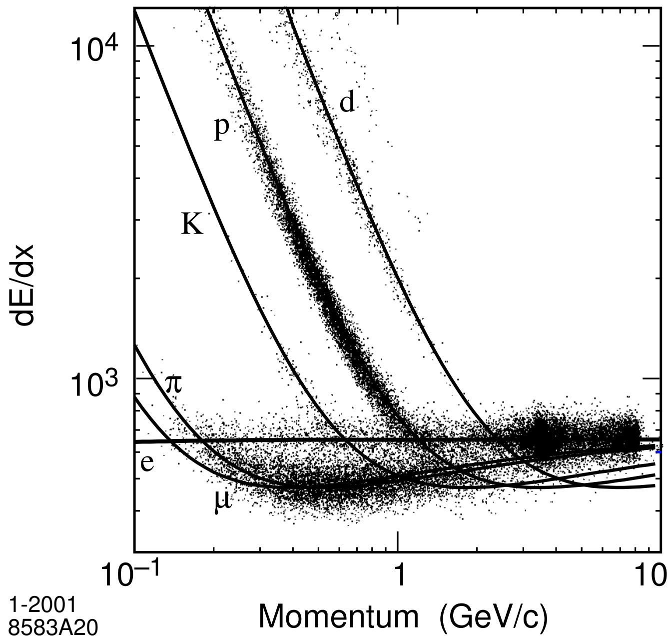

Figure 3.11: $\mathrm{d}E/\mathrm{d}x$ measurements in the DCH shown as a function of track momentum, where $\mathrm{d}E/\mathrm{d}x$ is in arbitrary units. The overlaid curves are Bethe-Bloch predictions calculated from control samples of each of the labelled particle types.

3.6 The Detector of Internally Reflected Cerenkov light (DIRC)

3.6.1 DIRC Physics Requirements

The DIRC provides charged particle identification (PID). Kaon-pion separation is essential for B flavour tagging, which is required for time dependent CP asymmetry measurements. Kaon-pion is also important for determining the correct final state in rare B decay analyses. The DCH can only provide separation for particles up to $700\,\mathrm{MeV}/c$, whereas the final state particles can have momenta up to about $4\,\mathrm{GeV}/c$. So, the DIRC must be able to provide particle identification for a large part of this momentum range. It must also complement the IFR for identifying muons that have p_T less than $750\,\mathrm{MeV}/c$, as the IFR is less efficient for muons with low transverse momentum.

The DIRC design is influenced by the EMC. The DIRC must be small in the radial direction so that the EMC does not have too large an internal radius. This is a cost factor, as the EMC is the most expensive part of the detector. Also, the DIRC must be thin in terms of radiation lengths. This is a measure of energy degradation before the calorimeter, and so impacts the resolution of the EMC. Also, to operate in a high luminosity environment, as delivered by PEP-II it must have a fast signal response, and be able to operate in high backgrounds.

3.6.2 DIRC Design

The DIRC is a ring imaging Cerenkov detector, which is designed so that it provides a 4σ K/π separation over the momentum range $0.7 - 4.2\,\mathrm{GeV}/c$. Cerenkov photons are produced when a charged particle travels through the DIRC, and these are transmitted via total internal reflection to photomultiplier tubes (PMTs), these being placed outside the detector acceptance.

Figure 3.12 shows a schematic of how the DIRC operates.. There are 144 synthetic quartz bars arranged into a 12-sided barrel. A charged particle will emit Cerenkov radiation if it passes through one of the bars with velocity βc and $\beta > 1/n$, where $n = 1.473$ is the refractive index of the quartz. The photons are emitted in a cone with opening angle θ_C, where $\cos\theta_C = 1/n\beta$. The photon is emitted in an azimuthal angle ϕ_c around the direction of the track. Some of these photons are trapped by total internal reflection, and so travel forwards or backwards along the bar. The direction depends on the incident angle of the particle. Only the backward end of the DIRC is instrumented, and so the forward moving photons are reflected by a mirror. This reduce background levels in the DIRC, and also makes enough room for an EMC endcap.

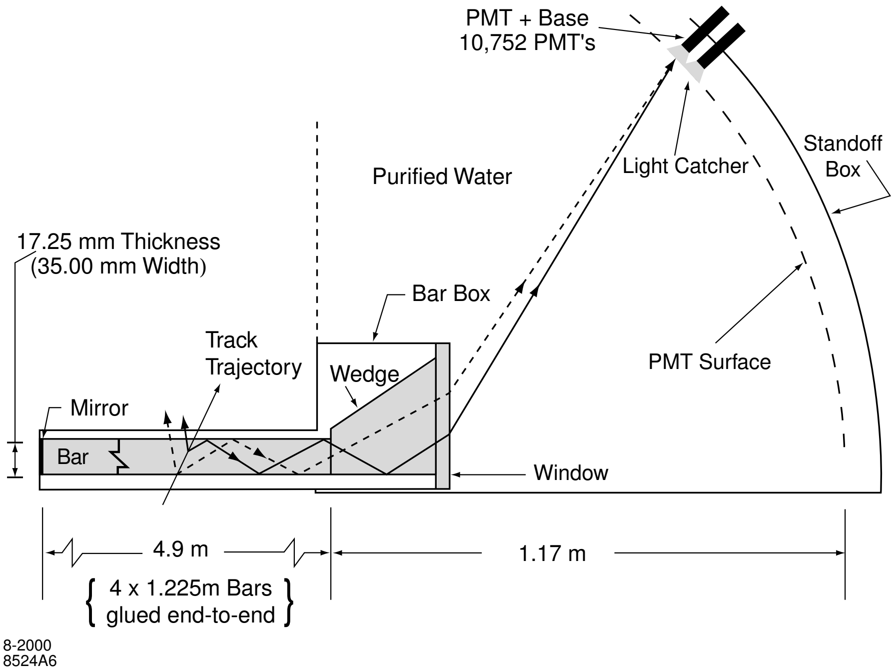

Figure 3.12: Structure and concept of the DIRC

After the photons arrive at the backwards end of the bar, they enter a region filled with 6000 litres of purified water, this is known as the standoff box. The water has a refractive index very close to quartz, and hence there is minimal total internal reflection at the boundary between the bars and the standoff box. An array of $10,752$ PMTs surrounded by "light catcher" cones detect the photons. There is also a magnetic shield round the standoff box to minimise the effect of the magnetic field on the PMTs.

There is a certain ambiguity attached to the Cerenkov angles, due to the possible paths that a photon could take to get to a particular PMT. Reconstruction code and the signal arrival time is used to deal with many of these.

The DIRC has an acceptance of 83% in the polar angle, and 94% in the azimuth. The thickness, which includes supports is $8\,\mathrm{cm}$ radially, and this translates to 17% of a radiation length for tracks that have normal incidence.

3.6.3 DIRC Performance

Di-muon events are used to calculate the time resolutions and Cerenkov angle. These are then used to determine the DIRC K/π separation power, also using the Cerenkov angles expected for kaons and pions. The K/π separation and the Cerenkov angle as a function of track momentum are shown in Figure 3.13 and Figure 3.14, respectively.

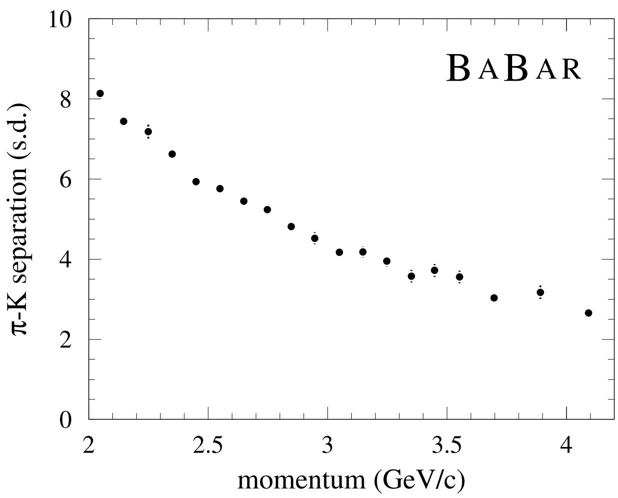

Figure 3.13: DIRC K/π separation as a function of track momentum

Figure 3.15 shows the effect of using the DIRC information in kaon identification. The peak in the shown $K\pi$ spectrum is the $\overline{D}^0 \rightarrow K^+\pi^-$ decay. When the DIRC information is used, it is observed that the combinatorial background greatly reduces, whilst the signal is

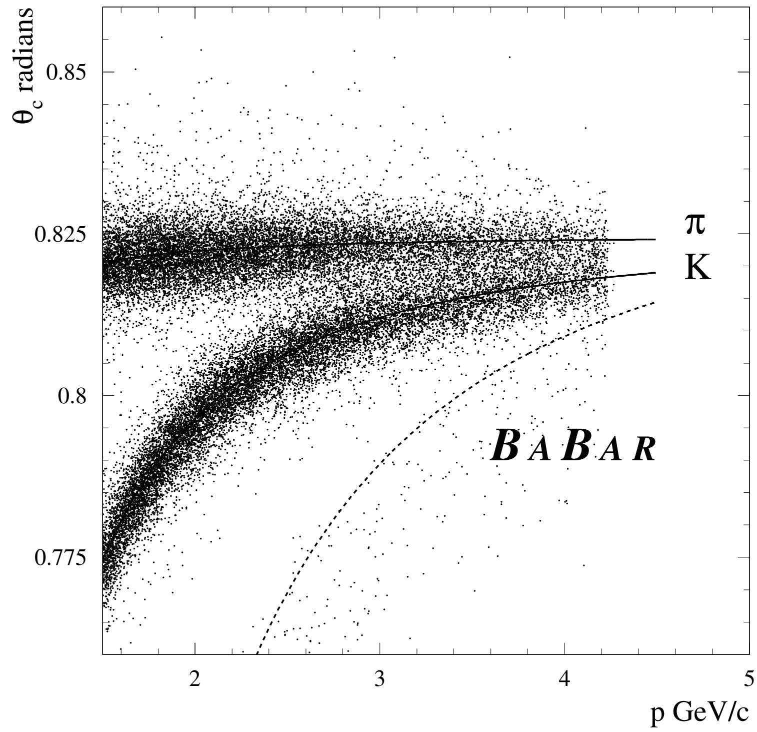

Figure 3.14: Cerenkov angle as a function of track momentum in the DIRC

left unaffected.

3.7 The Electromagnetic Calorimeter (EMC)

3.7.1 EMC Physics Requirements

Many B decays contain photons, which are products of the decay of π^0 or η particles. About half of the time, these photons have energies less than $200\,\mathrm{MeV}$. The EMC must be able to detect photons down to very low energy, around $20\,\mathrm{MeV}$. Also, processes such as $e^+e^- \to e^+e^-\gamma$ and $e^+e^- \to \gamma\gamma$ are important for calibration and monitoring luminosity. These can have energies as large as $9\,\mathrm{GeV}$ in the laboratory frame. The EMC needs to be able to detect electromagnetic showers with good resolutions in both energy and angle, with

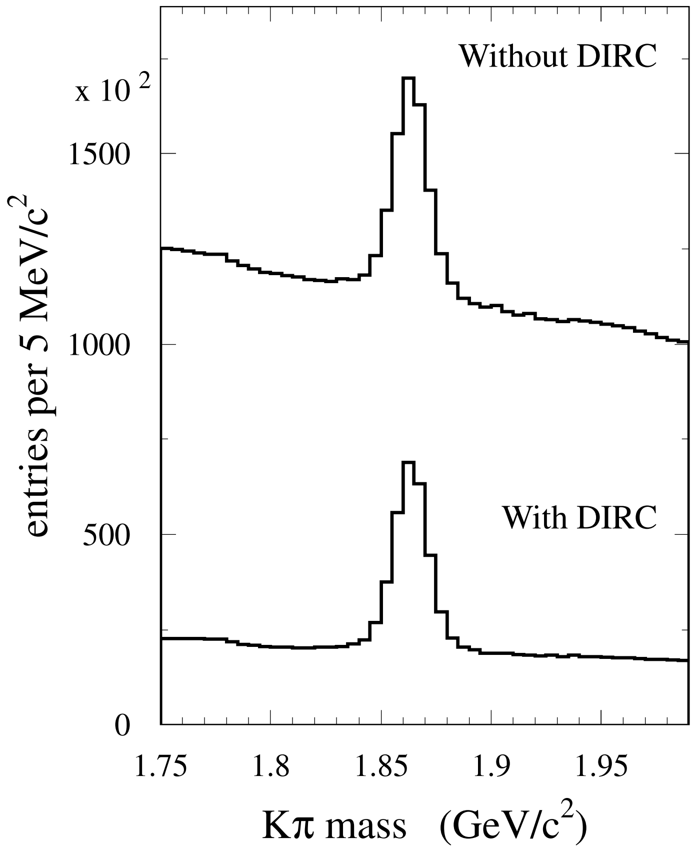

Figure 3.15: Reconstructed $K\pi$ mass with and without using the DIRC information for kaon ID. The peak corresponds to the decay $\overline{D}^0 \rightarrow K^+\pi^-$.

excellent efficiency over a large range of energies. Electron identification is also helped by the EMC, essential for flavour tagging in time dependent CP asymmetry measurements, and semi-leptonic B decays.

3.7.2 EMC Design

The EMC is constructed from 6580 Caesium Iodide (CsI) crystals doped with Thallium. These crystals are formed into a barrel and forward endcap, which is shown in Figure 3.16. CsI (Tl) was chosen, having a high light yield, giving very good energy resolution, with a small Moliére radius. This gives the EMC complete coverage azimuthally, and 90% coverage of the solid angle in the CM frame. The crystals are angled back to the IP. There are 5760 barrel crystals altogether, which are arranged into 48 rows in the θ direction, and 120 rows in the ϕ direction. The crystals are longer in the forward direction, in order to prevent shower leakage from more energetic Lorentz boosted forward particles. There are 820 endcap crystals, which are arranged into 8 rows in the θ direction. 3 of these rows have 120 rows in ϕ, 3 have 100 rows, and 2 have 80 rows. There is also a shielding ring inside the innermost crystals, this is to reduce the effect of machine background on the endcap crystals. The electromagnetic showers will spread over several adjacent crystals, thus forming a "cluster".

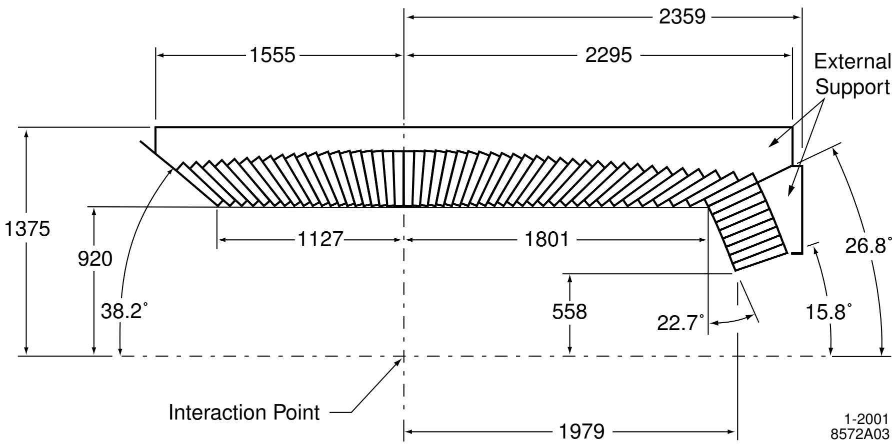

Figure 3.16: Side on view of the EMC showing only the top half - the detector is rotationally symmetric about the z-axis.

When the EMC receives a trigger, the data in a $1\,\mu\mathrm{s}$ windows undergoes processing to determine the crystal energy and peak time. The crystal data is also continuously summed into blocks of crystals, which are called "towers" and passed once every $269\,\mathrm{ns}$ to the Level 1 Trigger system.

3.7.3 EMC Performance

The EMC calibration is a two stage process. The first stage is used to determine the relation between the measured signal from each crystal and the actual deposited energy. The light yields are non uniform as a function of energy, and also vary significantly between crystals. Also radiation damage over the life of the detector can affect this relation. The low energy part of this first stage uses photons of energy $6.13\,\mathrm{MeV}$ coming from a radioactive source inside the detector. The high energy part is performed using Bhabha events, where the $e^{\pm}$ energy can be predicted from its polar angle. The second stage of the calibration is used to determine the relation between the cluster energy and the energy of the incident particle. There must be applied corrections for crystal leakage, absorption in material before the EMC and between crystals, and in other crystals not associated with the incident particle. The offline reconstruction process applies this correction. The correction can be derived from π^0 and η decays, as a function of cluster energy.

The energy resolution can be written in the following way

$$\frac{\sigma_E}{E} = \frac{a}{\sqrt[4]{E(\,\mathrm{GeV})}} \oplus b \tag{3.2}$$

where E and σ_E are the energy of a photon and its RMS error, measured in $\,\mathrm{GeV}$ and a and b are constants to be determined. The energy dependency is due mainly to fluctuations in photon statistics and also from electronics noise. The constant term is because of crystal leakage, absorption, non-uniformities and uncertainties in the calibration methods. In a similar situation to the calibrations, the resolution is measured at low using the detector radioactive source, whilst at high energies using Bhabha events. In the intermediate range processes such as π^0 decays are used. The energy resolution is shown in Figure 3.17 as it varies with energy, for various processes. Fitting Eq. (3.2) to these data values gives slightly worse parameters than the design goals, but however agreeing quite well with detailed Monte Carlo studies. These studies include the effects of machine backgrounds and electronics noise.

The EMC angular resolution is a function of the crystal size and the distance from the IP. It is described as follows:

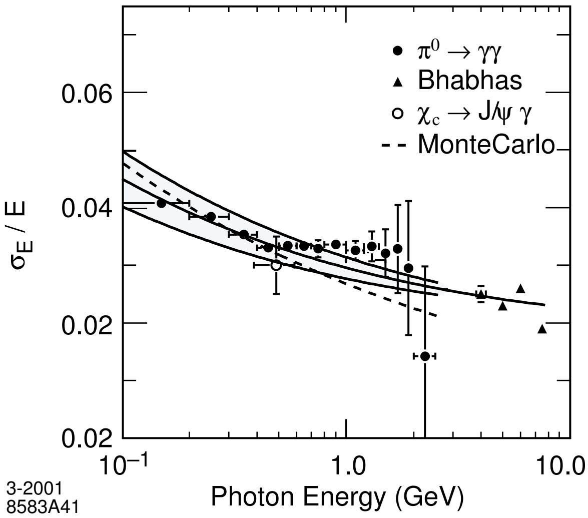

Figure 3.17: The energy resolution for the EMC measured for photons and electrons from various processes. The solid curve is a fit to Eq. (**??**) and the shaded area denotes the RMS error of the fit.

$$\sigma_\theta = \sigma_\phi = \frac{c}{\sqrt{E(\,\mathrm{GeV})}} \oplus d \tag{3.3}$$

where c and d are constants that need to be calculated. The decay of π^0 to two photons of around equal energies is used to determine them. Figure 3.18 shows the variation of angular resolution with photon energy. Fitting Eq. (3.3) gives values for these constants which are slightly better than those predicted from the Monte Carlo studies.

Electron identification uses data obtained from measuring the shower energies, the shower shapes, and track momentum. E/p is the most important variable. E is the recorded calorimeter energy, and p is the track momentum measured in either the SVT or DCH. E/p for electrons is around 1 as the mass of the electron, m_e is very small. Each electron produces electromagnetic showers in the EMC, consisting of photons, electrons and positrons, and by combining these the full energy of the original electron can be obtained. As they are very light, and so this full energy is roughly equal to their momentum.

Muons however are minimum ionising particles (MIPs). They travel through the EMC

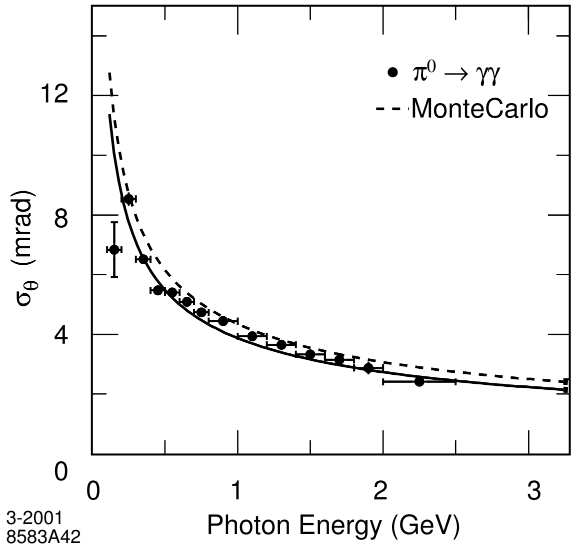

Figure 3.18: The angular resolution of the EMC for photons from π^0 decays. The solid curve is a fit to Eq. (3.3).

depositing very little of their energy. Charged hadrons, for example pions can act simply as MIPs, or they can interact, to produce an hadronic shower depositing a fraction of their energy. This behaviour of hadrons depends strongly on energy. Hadronic showers and electromagnetic showers can be distinguished as they have different longitudinal and lateral shapes. Figure 3.19 shows the electron efficiency and pion misidentification probabilities that are derived from radiative Bhabha events and reconstructed K_S^0 and τ decays.

3.8 The Instrumented Flux Return (IFR)

3.8.1 IFR Physics Requirements

Time dependent CP asymmetry analyses rely heavily on identification of muons, one example of such an analysis is the decay $J/\psi \;\; \to e^+e^- \; \mu^+\mu^-$. It is essential to identify muons for flavour tagging, where B mesons decay to semi-leptonic decays. In addition it is important to detect neutral hadrons, for example K_L^0 is used to reconstruct further CP eigenstates, the opposite CP state is K_S^0, and so is particularly important for CP analyses.

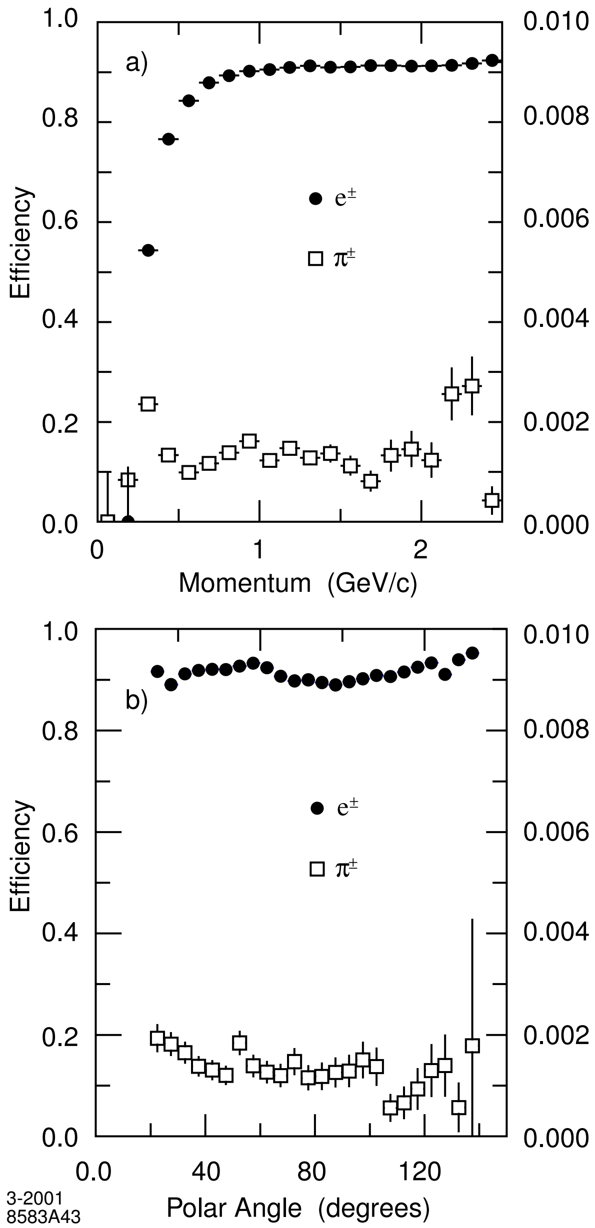

Figure 3.19: The electron efficiency and pion mis-identification probability as a function of a) the particle momentum and b) the polar angle, measured in the laboratory system.

The IFR must operate with high efficiency in muon identification, and with a high background rejection. The muons that are identified have a minimum momentum of 1 GeV/c. Neutral hadrons must also be detected with high efficiency and good angular resolution. It is desirable for the IFR to have a good solid angle coverage. The detector is relatively inaccessible, so the IFR must have high reliability and also monitoring systems should be used to keep track of the condition of the electronics.

3.8.2 IFR Design

As well as fulfilling these requirements, the IFR has a joint purpose of being a flux return for the 1.5T magnetic field, and a support structure for the rest of the *BABAR* detector. The thickness of the flux return were chosen after extensive tests using Monte Carlo. These studies were meant to optimise muon filtering and hadron absorption, and resistive plate chambers (RPCs) are placed in between each the steel layers. Figure 3.20 shows the arrangement of the detector, in particular how it is arranged in a hexagonal barrel, also with a forward and backward endcap. The solid angle coverage is 300 mrad with respect to the beamline in the forward direction, and 400 mrad in the backward direction. In the barrel there are 19 RPC layers, with each layer on each side of the barrel being split into 3 modules in the z direction. As for the endcaps, these contain 18 layers, which are split vertically in half, and each half contains 6 modules. There are also two additional RPC layers between the EMC and the magnet cryostat. These cylindrical layers are there to detect particles leaving the EMC and link tracks or EMC clusters with IFR clusters. These layers are composed of 4 quarter cylinder modules.

Figure 3.20 shows the cross-section of an individual RPC. An RPC detects streamers via capacitive readout strips. The streamers are emitted from ionising particles. The electrodes are plates made of Bakelite coated with graphite, and are $2\,\mathrm{mm}$ thick. A voltage of $8\,\mathrm{kV}$ is applied to the upper electrode, whilst the lower one is grounded. A PVC insulator is used to ensure the electrodes are kept separated and parallel, with the gap between being filled with a gas mixture. This is composed of 57% argon, 39% freon-134a and 4% isobutane, which

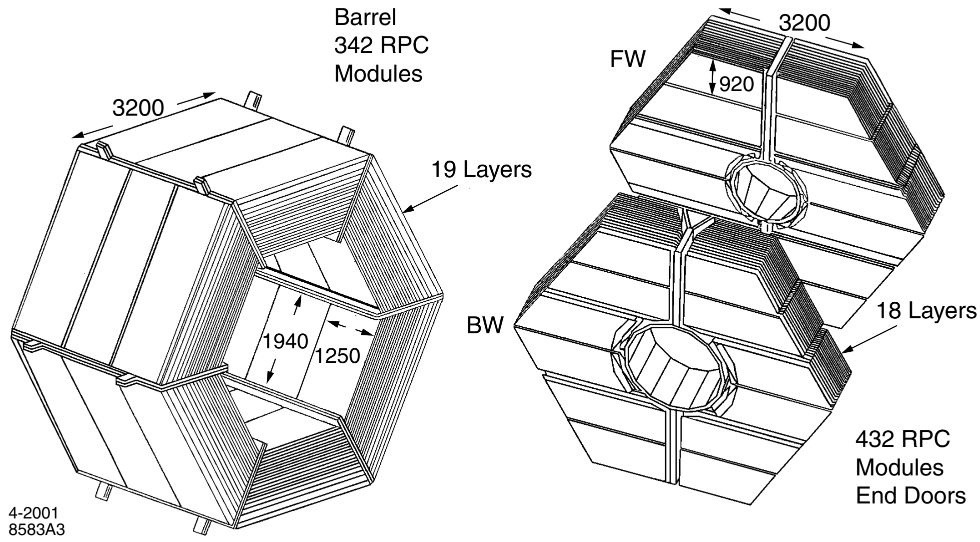

Figure 3.20: IFR geometry, showing the hexagonal barrel (left) and forward (FW) and backward (BW) endcaps.

is a non-flammable mixture. The two aluminium strips X and Y as shown in Figure 3.20 are positioned orthogonally. Along with the radial measurement from the thickness of the RPC, this gives three dimensional positional information.

There are 16 readout strips, which are then passed to a Front End readout Card (FEC). This applies a shaping procedure to the signals, and then compares them with a threshold, which determines whether or not the channel is active. Digitisation is applied to the signals from active channels, and then the hit information is passed at a frequency of once every $269\,\mathrm{ns}$ to the Level 1 Trigger.

3.8.3 IFR Performance

Clean control samples of muons and pions are used to determine the muon efficiency and pion misidentification probability. These are shown for *BABAR* Run 1 in Figure 3.22. It can be seen that for the momentum range 1.5 to $3.0\,\mathrm{GeV}/c$ a mean muon efficiency of around 90% was obtained, and a pion mis-identification rate of less than 8%.

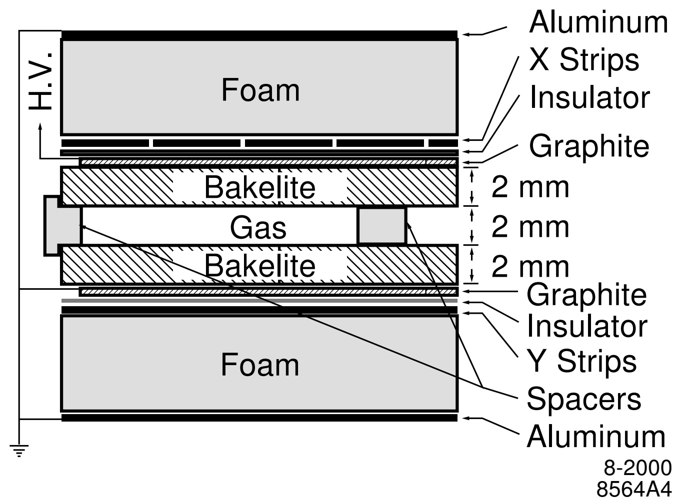

Figure 3.21: Cross section of a planar RPC with the schematics of the high voltage (HV) connection.

IFR clusters that are not associated with a charged track are determined to be neutral hadrons, for example K_L^0. Their detection efficiencies vary quite considerably. Using production angles in the EMC and in the cylindrical RPCs, and comparing them with the IFR clusters, can help to improve the angular resolution, sometimes by a factor of two.

Throughout Run 1 there was a problem with the muon efficiency degrading quickly in several RPCs. This was originally thought to be due to overheating, but even after additional cooling was installed many RPCs still showed efficiency reductions. In the shutdown after Run1, some dead RPCs in the forward endcap were replaced, whilst the malfunctioning RPCs were carefully inspected to try to determine the cause of the problems. No complete understanding of the problems was achieved.

The problem continued during Run 2, and by the end of this run the muon efficiency had dropped to around 65%. A long term solution was sought out. A couple of different approaches were taken, one for the barrel and one for the endcap. In the endcap, the RPCs were replaced with more efficient double-gap chambers, and several active layers were replaced with brass, so as to increase the absorbency. This was carried out during the 2002 summer shutdown. For the barrel, the plan was to replace six active layers with brass, and the rest of the RPC layers with Limited Streamer Tubes [45]. The first two sextants were installed during the 2004 shutdown, and the remaining four were installed during the summer 2006 shutdown.

3.9 The Trigger (TRG)

The *BABAR* trigger accepts interesting physics events and rejects backgrounds and is designed to have very high efficiency ($\approx 98\%$ or better) for hadronic decays of B mesons. It selects interesting physics events with a well understood and high efficiency, and the final event rate must be low enough for processing and storage.

The trigger consists of a Level 1 (L1) hardware trigger, and a Level 3 (L3) software trigger. The L1 trigger retains almost all physics events, whilst also rejecting background. The L3 trigger refines this selection by selecting the interesting physics events. The design ensures that the trigger can handle up to ten times the PEP-II background rates at design luminosity, and to slowly degrade at higher background levels. A fixed latency window is defined to be $11 - 12\,\mu\mathrm{s}$ after bunch crossing, and triggers are produced within this window.

3.9.1 Level 1 Trigger (L1T)

The Level 1 Trigger is designed to select events at a frequency of around $1\,\mathrm{kHz}$ at design luminosity. It consists of a DCH trigger (DCT), an EMC trigger (EMT), and IFR trigger (IFT) and a global trigger (GLT). These systems constantly receive data from their parent systems and produce summaries of the data called trigger primitives, being in terms of position and energy or momentum. The GLT takes these trigger primitives and combines them to form trigger lines, which are indicators of certain physical processes. If a trigger corresponds to the time of bunch crossing, then this is sent to the Fast Control and Timing System (FCTS). The purpose of the FCTS is to prescale or mask triggers if required, but for any that it doesn't a Level 1 Accept (L1A) is produced. This causes all of the subsystems, as well as

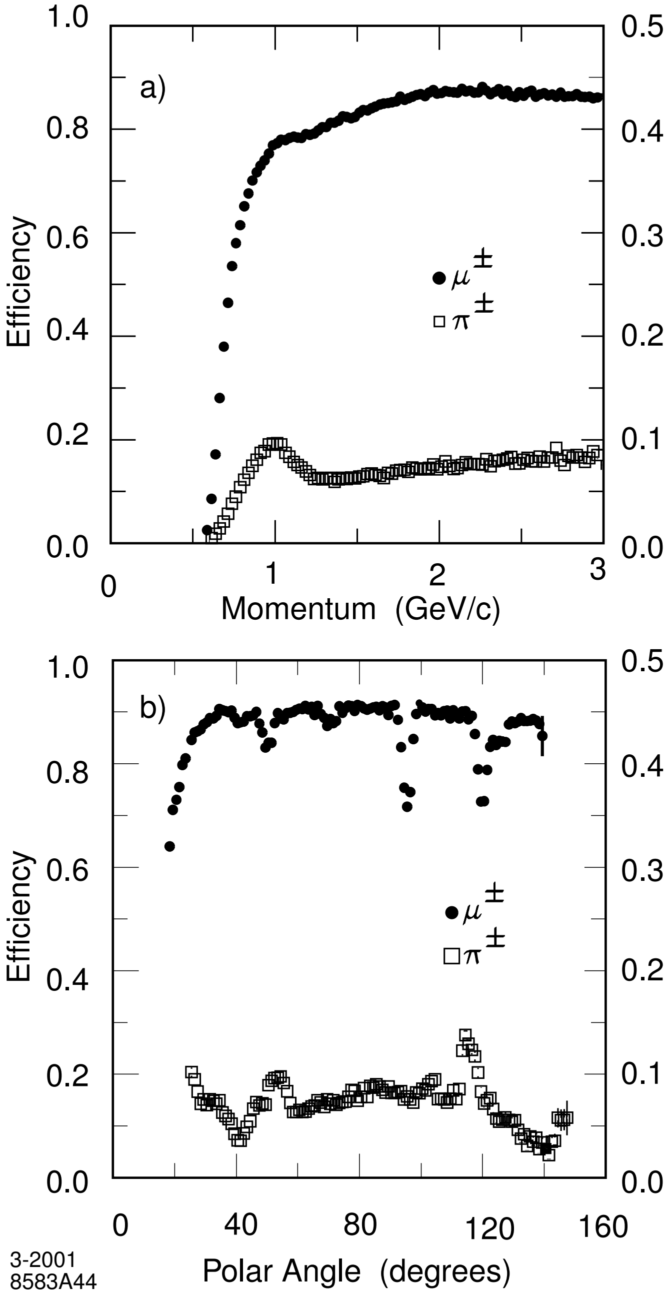

Figure 3.22: Muon efficiency (left scale) and pion misidentification probability (right scale) as a function of a) the laboratory track momentum, and b) the polar angle (for $1.5 < p < 3.0\,\mathrm{GeV}/c$ momentum), obtained with loose selection criteria.

the trigger, to read out their event buffers.

The DCT contains three types of trigger board, the Track Segment Finder (TSF), the Binary Link Tracker (BLT) and p_T Discriminant (PTD). The TSF looks for a *pivot group*, which is defined as a set of adjacent DCH hits in a group of eight cells within a superlayer (see Section 3.5.2. The BLT attempts to link track segments to form tracks. A long track is defined as a track that reaches the outermost superlayer. A short track is one that reaches at least half way through the chamber. The PTD looks at segments found in axial superlayers, and determines whether or not they are consistent with being part of a track with p_T greater than a threshold value, which is typically $800\,\mathrm{MeV}/c$. Table 3.3 shows the primitive definitions for both the DCT and EMT.

Primitive	**Origin**	**Description** (SL = superlayer)	ϕ **Segmentation**	p_T, **Energy Threshold**	z_0 **Cut** (cm)
B	DCT	Short track reaching SL U5	16	$120\,\mathrm{MeV}/c$	—
A	DCT	Long track reaching SL A10	16	$180\,\mathrm{MeV}/c$	—
Z	DCT	Track reaching SL A7	16	$220\,\mathrm{MeV}/c$	12
$\mathrm{Z_t}$	DCT	Track reaching SL A7, tighter z_0 cut	8	$220\,\mathrm{MeV}/c$	10
Z'	DCT	High p_T track reaching SL A7	8	$800\,\mathrm{MeV}/c$	15
$\mathrm{Z_k}$	DCT	Moderate p_T track reaching SL A7	4	$350\,\mathrm{MeV}/c$	10
M	EMT	All-θ MIP energy	20	$120\,\mathrm{MeV}$	—
G	EMT	All-θ intermediate energy	20	$307\,\mathrm{MeV}$	—
E	EMT	All-θ high energy	20	$768\,\mathrm{MeV}$	—
X (retired)	EMT	Forward endcap MIP energy	20	$100\,\mathrm{MeV}$	—
Y	EMT	Backward barrel high energy	10	$922\,\mathrm{MeV}$	—
U	IFT	Muon IFR sextant hit pattern	—	—	—

Table 3.3: Definition of L1T primitives. The threshold values are configurable and those shown here are typical values.

The EMT consists of only one type of trigger board, the Trigger Processor Board (TPB).

The TPBs receive their energy samples from 280 EMC towers. These energies are summed over the polar angle, forming 40 "ϕ strips", and then these are summed with their nearest neighbour. The energy and time of the peak in the waveform is obtained using a simple feature extraction. The thresholds as shown in Table 3.3 are used to define three EMT primitives, 'M', 'G' and 'E'. Two other primitives, 'X' and 'Y' are defined that discriminate position in the polar angle. The 'X' is now obsolete, as the PTD in the DCT is no longer used.

The IFT is used to trigger on $\mu^+\mu^-$ events, and also cosmic ray muons, which are used for calibration and diagnostic purposes. The primitive for the IFT are single clusters, or pairs of back to back clusters, which also includes information of whether they are located in the barrel or the endcap.

The DCT and EMT are orthogonal, which allows the individual trigger efficiencies to be easily determined. Each nearly satisfy the trigger requirements independently. Individually they have an efficiency for $B\overline{B}$ events of over 99% and their combined efficiency is over 99.9%.

3.9.2 Level 3 Trigger (L3T)

The design goal of the Level 3 Trigger is to reduce the $1\,\mathrm{kHz}$ Level 1 rate to about $100\,\mathrm{Hz}$ at design luminosity. The Online Event Processing (OEP) computing farm is used to run the Level 3 code.

More sophisticated algorithms are used by the Level 3 Trigger, as all of the event information is available, including positional information as well as increased energy and momentum resolution. Timing information helps to reject backgrounds, and track impact parameters can help isolate machine backgrounds. By running a series of algorithms, the event can be classified into different categories for physics, and also other types for calibration and monitoring, for example cosmic ray and Bhabha events. The L3 output lines are formed from logical combinations of these algorithm outputs, analogous to how the GLT forms trigger lines from L1 primitives.

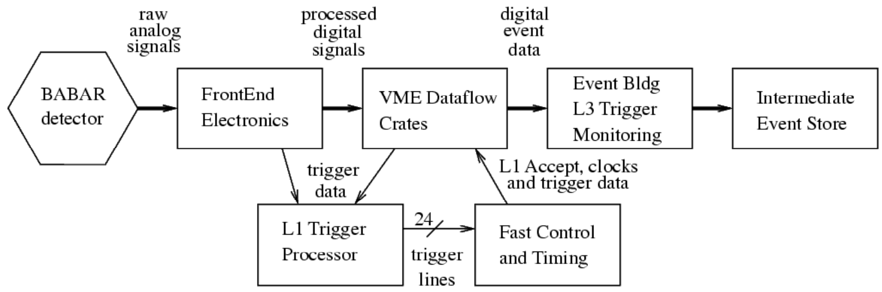

Figure 3.23: Schematic of the *BABAR DAQ* system

Some of the L3 lines are prescaled to reduce the rate at which the data for certain events are recorded. In particular, Bhabha events are needed for calibration and luminosity, but at much lower rates than they occur. "L1 Pass-Through" rates are events that have not passed Level 3, and these are accepted at a defined prescale rate. These events are used to carry out calculations of efficiency. For events that pass the L3 criteria, they are logged to disk.

3.10 The Data Acquisition System (DAQ)

A schematic of the *BABAR* DAQ system is shown in Figure 3.23. The Front End Electronics, based on each subsystem processes the raw detector output, and then sends the digitised signals over fast fibre optics links to the VME dataflow crates, which contain the dataflow Read Out Modules (ROMs). In the DCH and IFR, these signals are also sent to the DCT continuously. The ROMs contain Trigger Personality Cards (TPCs), for every system except for the EMC. This means that signals are only obtained from the FEE when a L1A has been sent from the FCTS. However, for the EMC, the ROMs contain Untriggered Personality Cards (UPCs), which means the signals are continuously received from the FEE. They are processed, and on receipt of a L1A, passed to another TPC ROM. The UPCs also sum the energies over the towers, which are continuously sent to the EMT.

For triggered events, the TPC ROMs run software to perform a feature extraction (FEX), which attempts to isolate signals and suppress background and noise. This software is specific to each subsystem. The ROMs and other boards can be configured on a run by run basis, for which the configuration database is used. This database stores objects for the configuration of each system. The data are than sent to the OEP farm so that the Level 3 Trigger can process it, and it is also available for data quality monitoring. Events that are written from Level 3 are processed in Offline Prompt Reconstruction (OPR) farms. Important information regarding detector conditions are saved in the conditions database, for example temperature, voltages, gas supply and humidity. These quantities are used later in the OPR event reconstructions.

Chapter 4

Analysis Techniques

4.1 Introduction

This chapter describes the general techniques used to carry out this analysis. These are used throughout the *BABAR* collaboration and within other high energy physics experiments.

BABAR has a very large amount of stored data, this being because of the large luminosities and the complicated nature of the detector. There is a centrally managed processing system which allows collaborators to analyse the full dataset. Using this same system, simulated events are used to compare with the data.

4.2 Reconstruction

After *BABAR* stores the data, the raw signals must be reconstructed in order to determine the particle identities and associated variables. This reconstruction occurs in two main parts:

- Offline Prompt Reconstruction (OPR) is the first process to run. This involves reconstructing charged tracks and calorimeter clusters using the raw detector hits. Also used is tracking system and DIRC information, in order to produce particle identification selectors. The data quality monitoring and rolling calibrations are also run at this stage.

OPR is run on computer farms in two stages. The first stage involves running rolling calibrations and also some of the data quality monitoring. This is run a few hours after the events are originally saved to disk. The second stage consists of the full reconstruction routines and this is run within a few days. The data are subsequently stored in an object-oriented database system. This was originally designed around Objectivity™ technology, but now has been rewritten using a *BABAR* designed system based on `Root`. This database is also termed the event store.

- The second reconstruction process combines the output from the OPR stages to form particle candidates from their decay products. There are several analysis packages used, based on a common *BABAR* framework.

4.2.1 Tracking Algorithms

There are specific routines used to reconstruct tracks, and these use data from the L3 Trigger, the SVT and the DCH. Five quantities are used to describe the charged tracks, these are defined at the point of closest approach (POCA) of the track to the z-axis, as follows:

- z_0 - the distance along the z direction to the co-ordinate system origin,
- d_0 - the distance in the x-y plane to the z-axis,
- ϕ_0 - the azimuthal angle of the track,
- $\tan\lambda$ - the tangent of the track's dip angle with, respect to the x-y plane
- $\omega = 1/p_T$ - the track curvature.

The Kalman fitting technique [46] is used to model the detector material distribution and the local magnetic field variations. This algorithm is applied to the hits describing the L3 tracks. The measurement of collision time is improved by utilising DCH hits consistent with the tracks, and then reapplying the fit. The rest of the DCH hits are then used to find tracks that originated away from the IP, or those that did not cross the whole chamber.

DCH tracks are extrapolated into the SVT, finding any hits that are consistent to add to the existing ones. An SVT track finder looks at the remaining SVT hits to find low momentum, SVT-only tracks. In addition, SVT tracks are projected into the DCH in an attempt to combine tracks that were scattered by the SVT support structure.

Tracks are placed into lists stored in the event database, the list used depends on the track quality. The track list used throughout this analysis is `GoodTracksLoose`, which has the following requirements:

- A minimum transverse momentum of 0.1 GeV/c,
- A maximum momentum of 10.0 GeV/c,
- at least 12 hits in the drift chamber,
- $d_0 < 1.5\,\mathrm{cm}$,
- $z_0 < 10\,\mathrm{cm}$.

4.2.2 Calorimeter Algorithms

These routines specifically reconstruct neutral particles, using data from the EMC. Algorithms combine individual crystals into clusters, where clusters correspond to individual particle showers. This procedure can be broken down into a few stages:

- finding crystals with energies greater than $10\,\mathrm{MeV}$,
- adding neighbouring crystals with energies greater than $1\,\mathrm{MeV}$,
- adding further crystals that fulfill this energy requirement, or if they are next to a crystal already in the cluster that has an energy greater than $3\,\mathrm{MeV}$,
- and then repeating this process until no further crystals fulfill the requirements.

A "bump" finding algorithm runs over the crystals that make up the cluster. This determines the local maxima within the cluster, as there may be more than one shower causing the cluster.

Charged tracks are also projected onto the inside surface of the EMC. Each track is associated with a bump, and they are then associated together. Bumps not connected with tracks are then assumed to be from neutral particles. These are then placed into list analogous to those used for tracks. Throughout this analysis, the neutral particle list used is `pi0DefaultMass`.

4.2.3 Particle Identification (PID)

Charged tracks detected within *BABAR* can be one of five types: pions, kaons, electrons, muons or protons. Data from each of the subsystems are combined in order to form particle selectors. A likelihood for each type of particle is constructed using PDFs. There is actually no selector for pions, but if a track fails the other selectors it is therefore assumed to be a pion. The PID selectors are developed by the *BABAR* PID group [47, 48]

4.2.3.1 Kaon Identification Selector

The Kaon selectors use the Cerenkov angle and the number of photons as measured in the DIRC, and the $\mathrm{d}E/\mathrm{d}x$ measurement using both the SVT and DCH.

The selectors compare the measured and expected Cerenkov angles, the expected angles determined using the measured momentum in the DCH to obtain the mass of the particle, as the Cerenkov angle in the DIRC depends on the particle's mass. The difference between the two is divide by the experimental errors to obtain a pull. The pull is distributed as a Gaussian. The likelihood PDF is calculated using control samples, one of these modes being $\phi \to K^+K^-$. Low momentum tracks pose difficulties, so the number of measured photons is used in these cases to obtain an accurate description of the likelihood.

$\mathrm{d}E/\mathrm{d}x$ PDFs are created similarly using the pulls. The expected $\mathrm{d}E/\mathrm{d}x$ values are modelled by Bethe-Bloch functions, and the pull distributions are obtained from data control samples.

The *BABAR* "SMSKaonSelector" uses the product of these two likelihoods as a DIRC likelihood. The tightness of the selector corresponds to using different likelihood cuts (e.g. *NotAPion, VeryLoose, Loose, Tight* or *VeryTight*). The tighter the cut, the lower the selection efficiency, but the higher the purity.

4.2.3.2 Electron Identification Selector

The EMC provides the primary means of electron identification with E/p and electromagnetic lateral and longitudinal shower shapes being the main variables. Measurements of $\mathrm{d}E/\mathrm{d}x$ from the DCH provide further discriminating power.

For tracks with momentum less than $1.5\,\mathrm{GeV}/c$ the Cerenkov angle from the DIRC is also used. Loose selections are initially applied to separate muons.

The DCH $\mathrm{d}E/\mathrm{d}x$ distribution is modelled in the same way as in the Kaon selector. The E/p distribution is modelled as a Gaussian with an exponential tail. The lateral shower shape variables are described by double Gaussian PDFs. For electrons, the correlations between these variables are negligible, but for hadrons they have to be considered. The Cerenkov angle is modelled as a double Gaussian for electrons. This shape accounts for deviations in the flight direction of electrons due to bremsstrahlung, as well as pions decaying to muons, or emitting electrons both of which happen in the DIRC.

4.2.4 Vertexing Composite Candidates

Composite candidates cannot be detected directly, but have to be reconstructed from their more stable decay products. For example, the mode considered here $B^{\pm} \to (a_1\pi)^{\pm}$, involves the a_1 and ρ resonances, which are so short-lived it appears that the charged tracks originate from the B decay vertex.

The *BABAR* vertex fitting routine is called `Geokin`. This uses an iterative χ^2 minimisation procedure. This involves running geometric fits, which constrain the tracks to come from the same point in space. Kinematic fits are also performed, these ensure that momentum is conserved at the vertex. To optimise the energy and momentum resolution, the track momenta are varied within their measured errors.

Two vertex fits are performed on the B candidates. In the first no constraint is applied to the mass of the B. In the second fit the tracks are constrained to have a B mass average. The constrained fit has the advantage that it improves the resolution and prevents decay daughter products falling outside the Dalitz kinematic region. The reconstruction makes continuum events appear more B-like and ...

A second vertex fit is performed, in this the tracks are constrained to have an invariant mass equal to world B mass average. This leads to reconstructed following Dalitz plot kinematic constraints. This improves the resolution on the intermediate resonance mass. It also makes continuum events appear more B-like in terms of their kinematics. Because of this, unconstrained kinetic variables are used to discriminate against continuum events, although constrained fit values are used to determine event topology variables.

4.3 Monte Carlo Simulation

Monte Carlo simulations are essential in order for the huge amount of data that is recorded by the *BABAR* detector to be interpreted correctly. It is beneficial to have a large statistical sample of simulated events. A full detector simulation is carried out, and then the same reconstruction routines used for data are applied.

The simulation can be broken down into three main parts:

- Event generation,
- Simulation of the movement of particles through the detectors, and the response from detector material,
- Detector electronics response, involving the trigger.

The *BABAR* EvtGen package is used for event generation. This allows effects such as CP violation and interference to be included and their parameters varied. Within EvtGen a package called Jetset is used to generate continuum events, and also for some B events.

The simulation of the detector is carried out by *BABAR* specific code based around the GEANT4 package. A detailed model of the *BABAR* detector geometry and materials is constructed. This involves looking at the behaviour of particles as they travel through the detector, and how they affect the trigger systems. All of this information is stored in an object called a "gHit". This contains the information on the interaction with the detector.

The final stage, the electronics response simulation attempts to simulate the processing of detector signals through the front end electronics and dataflow crates to the DAQ system. This includes a software simulation of the trigger system, which determines when an event would be triggered on and stored.

Also present in real data are machine backgrounds. During data taking, cyclic triggers are issued about once every second, and this tells the DAQ system to read out its event buffers. The data written from these triggers represent a good sample of the detector background conditions. These events are stored and then overlaid with simulated data. Together this constitutes the full data simulation.

The reconstruction for simulated data is almost identical to that for real data. One exception is that truth information is saved for Monte Carlo, this is so that misreconstruction effects for data can be estimated. The simulated events are saved in the event store, from which these will be retrieved for later analysis.

4.3.1 Efficiency Corrections

The reconstruction algorithms show a small difference when applied to data and Monte Carlo, this applies to both tracking and PID. To study this difference, control samples are used and the reconstruction efficiency for both data and Monte Carlo is tabulated. These are then saved into a database and later used to correct the event efficiencies. These corrections also have associated systematic errors.

For the tracking algorithms, the ratio of efficiencies are stored, and later used to correct the reconstruction efficiency. MC overestimates the efficiency and so a subtraction of 0.8% must be applied for each track. The efficiency corrections for each track can be added linearly as they are correlated, if the efficiency is low for one track then it is likely to be low for the others. For the mode $B^+ \to (a_1\pi)^+$, this results in a total tracking correction of -2.4%, or 97.6% of the reconstructed efficiency. Each track has an associated systematic error of 1.3%, giving 3.9% in total for this analysis.

For the PID algorithms the selectors are applied to either accept or reject events, and then there are several procedures to correct for the efficiency differences, with these corrections being applied in the same direction for different tracks. The PID "tweaking" method compares each track's data and MC efficiencies. The the MC efficiency is greater than that of data, and the track was accepted, then it will be rejected with probability $1 - \epsilon_{data}/\epsilon_{MC}$. If the track was already rejected, then nothing is done. If the data efficiency is greater than the MC efficiency, and the track was rejected then it will be accepted with a probability of $1 - \frac{1-\epsilon_{data}}{1-\epsilon_{MC}}$. In this case if the track was already accepted, then nothing is done. The systematic error is calculated from control sample studies, and is 1.4% per corrected track, which is added linearly.

4.4 B Counting

To be able to make a branching fraction measurement, the total number of $B\overline{B}$ pairs ($N_{B\overline{B}}$) must be accurately determined. The $\Upsilon(4S)$ production cross section is not sufficiently well known, so an alternative method to determine the number of $B\overline{B}$ pairs, known as "B Counting" must be used.

The B counting method involves carrying out a weighted subtraction of the number of multi-hadronic events (N_{MH}) recorded $40\,\mathrm{MeV}$ below the $\Upsilon(4S)$ resonance from the number recorded at the $\Upsilon(4S)$ resonance ($10.58\,\mathrm{GeV}$ CM energy). Data taken below the $\Upsilon(4S)$

resonance is below the $B\overline{B}$ production threshold, so the difference must be due to $\Upsilon(4S)$ production. The energy dependence of the continuum cross section must also be taken into account, and also the ratio of onpeak and off peak integrated luminosities must be included. This can be taken as the ratio of the number of μ μ pairs ($N_{\mu\mu}$). It is also assumed that the branching ratio of $\Upsilon(4S) \to B\overline{B}$ is 100%. $N_{B\overline{B}}$ is given by

$$N_{B\overline{B}} = \frac{1}{\epsilon_{B\overline{B}}} \left(N_{MH}^{On} - N_{MH}^{Off} \kappa \frac{N_{\mu\mu}^{On}}{N_{\mu\mu}^{Off}} \right). \tag{4.1}$$

where $\epsilon_{B\overline{B}}$ is the efficiency with which $B\overline{B}$ events pass the multi-hadronic selection cuts, these being calculated from the MC simulation. $\kappa \sim 1$ is a constant, which accounts for the energy dependence of the continuum cross section and selection efficiency.

This procedure as applied to the data used for this analysis gives a value of

$$N_{B\overline{B}} = (231.8 \pm 2.6) \times 10^6 \tag{4.2}$$

Further details, including the error calculation can be found in [49].

4.5 Discriminating Variables

For analyses of rare charmless decays, there are large levels of background, for which well understood discriminating variables are required. These variables consist of two main categories: kinematic and topological. They can also be used in two ways. If the distribution of the variable lies in a different range for both signal and background events then the variable can be cut on. This results in an increased signal to background ratio. The alternative is to use the variable as an input to the Maximum Likelihood fit, which is possible if the distributions have different shapes. See Section 4.6 for a description of the analysis method.

4.5.1 Kinematic Variables

One immediately obvious discriminating variable is the reconstructed mass of the B meson candidate:

$$m_B = \sqrt{E_B^2 - \vec{p}_B^{\,2}} \tag{4.3}$$

which should be distributed around the actual B mass, $5.279\,\mathrm{GeV}$, for correctly reconstructed candidates. The B candidates are reconstructed from many tracks and neutrals clusters, the detector resolution affecting each of these. The overall effect is large and this causes the B mass distribution to become very wide ($\sim 25\,\mathrm{MeV}$).

As this isn't an ideal variable to use, we don't use the B energy and mass, but instead construct two variables, which are mostly uncorrelated, and have the benefit of being more constrained [50, 51, 52].

The difference between the reconstructed and expected B meson energy (ΔE) is defined as

$$\Delta E = E_B - E_X \tag{4.4}$$

and the beam-energy substituted mass (m_{ES}) is defined as

$$m_{\mathrm{ES}} = \sqrt{E_X^2 - \vec{p}_B^{\,2}} \tag{4.5}$$

where (E_B, $\vec{p}_B$) is the four momentum of the reconstructed B meson and E_X is the beam-energy constrained derived energy for the B defined by

$$E_X = \frac{E_{beam}^2 - \vec{p}_{beam}^{\,2} + 2\vec{p}_{beam} \cdot \vec{p}_B}{2E_{beam}} \tag{4.6}$$

where (E_{beam}, $\vec{p}_{beam}$) is the four momentum of the beams. These quantities are all defined in the laboratory frame. m_{ES} is independent of the mass hypothesis of the B

daughter tracks, whereas ΔE depends on this as it uses the reconstructed energy of the B candidate. $m_{\rm ES}$ should peak at the B mass, $5.279\,\mathrm{GeV}$, and ΔE should peak at zero. Typical resolutions for $m_{\rm ES}$ and ΔE are $2.5\,\mathrm{MeV}$ and $20\,\mathrm{MeV}$ respectively.

4.5.2 Topological Variables

It is necessary to include variables that describe the event topology. The $B\overline{B}$ pair and $\Upsilon(4S)$ mass difference is very small, which means that the $B\overline{B}$ pair is produced almost at rest in the CM frame, and the decay products therefore have an isotropic distribution. For continuum events, mesons are produced with very large kinetic energy, and this results in the decay product jets being highly collimated around the original $q\overline{q}$ axes.

There are several possible variables that distinguish continuum background from signal events. For these it is useful to divide the particles into those from the reconstructed B candidate and those from the rest of the event (ROE). All quantities related to these variables are calculated in the CM frame.

4.5.2.1 Thrust

The cosine of the thrust angle $(\cos\theta_{\rm T})$ is defined as the cosine of the angle between the thrust axis of the reconstructed B candidate and the thrust axis of the ROE. The thrust axis of a collection of particles is the axis along which the total longitudinal momentum is maximised. $|\cos\theta_{\rm T}|$ peaks at 1 for jet-like events, and is almost uniform for B events. A cut is applied on this variable to remove many background events, in particular this is useful to remove continuum events. Figure 4.1 shows the distributions of $\cos\theta_{\rm T}$ for both MC and data.

4.5.2.2 Energy / Momentum Flow

Several variables can be defined that describe the momentum or energy flow of the ROE, and are used to provide further discrimination. In the energy flow method pioneered by CLEO,

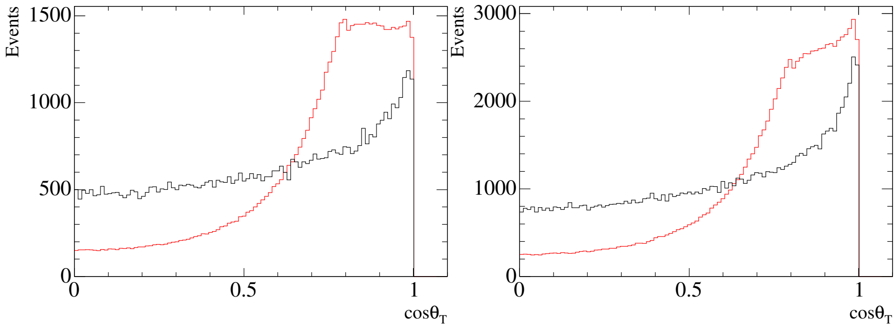

Figure 4.1: Distribution of the thrust for $B^+ \to a_1^+ \pi^0$ (left) and $B^+ \to a_1^0 \pi^+$ (right). Signal MC is shown in black and data is shown in red.

the event is split into 2 hemispheres, defined around the thrust axis of the reconstructed B. Within each hemisphere, 9 concentric 10° cones are formed. In each cone, the energy flow of all particles is summed, producing 9 variables.

Legendre polynomials are an alternative way of defining energy flow. From studies the zeroeth and second order polynomials provide the best discrimination, and these are defined as:

$$L_0 = \sum_i^{N_{ROE}} p_i, \quad (4.7)$$

$$L_2 = \sum_i^{N_{ROE}} p_i \times \frac{1}{2}(3\cos^2\theta_i - 1). \quad (4.8)$$

Individually it is found that these variables are not very powerful. It is possible to combine these into a Fisher discriminant or neural net, and these give a much large discriminating power. For this analysis a Fisher discriminant is used.

4.5.2.3 Conservation Of Angular Momentum

To construct a further set of variables, it is useful to consider angular momentum conservation. The first of these, $\cos\theta_{Bmom}$ is defined to be the cosine of the angle between the momentum of the reconstructed B candidate and the z-axes. True B events are decays of the spin one $\Upsilon(4S)$ particle to two spin zero B mesons, and so the angular momentum distribution is proportional to $\sin^2(\theta_{Bmom})$. For $q\overline{q}$ events the distribution is uniform.

The second variable, $\cos\theta_{Bthr}$ is defined as the cosine of the angle between the thrust axis of the reconstructed B candidate and z-axis. This variable is distributed roughly uniformly for true B events, as B decays are spherical. $q\overline{q}$ events have a distribution proportional to $1 + \cos\theta_{Bthr}$.

Similar to the energy and momentum flow variables, these variables are not very powerful individually, but when combined into a Fisher discriminant their usefulness is increased.

4.5.3 Fisher Discriminant

In order to improve discriminating power, the previous variables must be combined, and there are several methods to achieve this. One method is using Neural Nets, these being non-linear. The method used in this analysis is a Fisher discriminant, which is linear. The Fisher discriminant is defined as:

$$\mathcal{F} = \sum_i a_i x_i = \vec{a}^{\,T}\vec{x}. \tag{4.9}$$

where x_i is a discriminating variable, and a_i are coefficients to maximise the signal to background separation.

Studies [53] show that L_0, L_2, $|\cos\theta_{Bmom}|$ and $|\cos\theta_{Bthr}|$ combined give excellent discrimination. The difference in using the Fisher and Neural net in terms of discriminating power is negligible.

4.5.4 Helicity

The helicity, $\mathcal{H} = |\cos\theta_{\mathcal{H}}|$ is defined as the absolute value of the cosine of the angle between the direction of the π meson from $a_1 \rightarrow \rho\pi$, with respect to the flight direction of the B in the a_1 meson rest frame.

Figure 4.2 shows the distribution of helicity. Ideally it has flat distribution for signal, but a peak near ± 1 for misreconstructed candidates. However, detector effects make the distribution asymmetric, and also cause the signal one to peak, so that the shapes end up being similar.

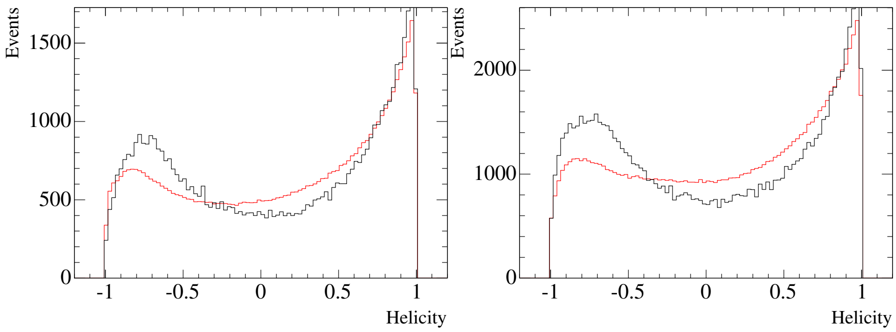

Figure 4.2: Distribution of the Helicity angle for $B^+ \to a_1^+ \pi^0$ (left) and $B^+ \to a_1^0 \pi^+$ (right). MC is shown in black and data is shown in red.

4.5.5 Decay Plane Normal

The decay plane normal, $\mathcal{A}$, is defined as the cosine of the angle between the normal to the plane of the 3π resonance and the flight direction of the bachelor pion, evaluated in the 3π resonance rest frame. This distribution proves useful in distinguishing backgrounds such as $B \to a_2 \pi$, with the a_2 having a spin of 2, compared to the a_1, which has a spin of 1.

4.6 Maximum Likelihood Fitting

Maximum Likelihood Fitting is a powerful statistical method that is a method for estimation used to determine several parameters from a data set. A more detailed description of this can be found in [54].

In comparison with the χ^2 method, the maximum likelihood technique treats events individually, so there is no need to bin data, which would lead to some inevitable bias and inaccuracy.

It is necessary to create normalised probability distributions functions (PDFs) using the fit variables, where the PDFs are distributions of the variables normalised to unity. The likelihood is then defined to be:

$$\mathcal{L}(\vec{\alpha}) = \prod_{i=1}^{N} \mathcal{P}(\vec{x}_i; \vec{\alpha}), \tag{4.10}$$

where $\vec{\alpha}$ are the parameters of the PDF. N measurements are made of the variable x.

It is more convenient to minimise the negative log-likelihood, as opposed to maximising the likelihood. The negative log-likelihood is defined as

$$-l = -\log \mathcal{L} = -\sum_{i=1}^{N} \log \mathcal{P}(\vec{x}_i, \vec{\alpha}) \tag{4.11}$$

4.6.1 Error Calculation

There are two equally useful methods for calculation of parameter errors. The first way involves calculating the covariance matrix of the fit parameters as follows

$$H_{ij} = \frac{\partial^2 l}{\partial \alpha_i \partial \alpha_j} \tag{4.12}$$

and inverting this to give the error matrix, $E = H^{-1}$.

The second method uses a Taylor expansion of l about its maximum, and then neglects higher order terms. This can be written as

$$l = l_{max} + l'(\delta\alpha_i) + \frac{l''(\delta\alpha_i^2}{2! + \cdot} \tag{4.13}$$

, as the log-likelihood is parabolic close to its maximum. This implies that the likelihood $\mathcal{L}$ is Gaussian close to the maximum, and so the parameter error can be expressed as

$$l(\alpha_i \pm \sigma_{\alpha_i}) = l_{max} - \frac{1}{2} \tag{4.14}$$

4.6.2 Extended Maximum Likelihood Fitting

The PDF normalisation has so far been assumed to be unity. However in practice the normalisation depends on the event yields, these are distributed as a Poisson distribution with a mean ν. This yields the extended likelihood function

$$\mathcal{L}(\vec{\alpha}, \vec{n}) = \exp\left(-\sum_{k=1}^{M} n_k\right) \prod_{i=1}^{N} \left(\sum_{j=1}^{M} n_j P_j(\vec{\alpha}, \vec{x_i})\right) \tag{4.15}$$

where the n_j are the number of events in hypothesis j. The extended maximum likelihood function is used in this analysis.

4.6.3 Fitting Package

Being such a commonly used technique, there are dedicated fitting packages to carry out maximum likelihood fitting.

`Minuit` [55, 56] is one such package, it minimises a function and returns parameters with errors. Within `Minuit`, there exists three main routines:

- MIGRAD is the most common minimisation routine. It calculates the function minimum, and makes an initial attempt at calculating the parameter errors.
- HESSE carries out a more precise error calculation, using the matrix inversion technique.
- MINOS performs an error calculation at a further level of precision error. This is an iterative process based on the Taylor expansion method.

RooFit [57] is a package that has been developed within the *BABAR* collaboration. It provides a simplified interface to Minuit through Root [58]. Various PDF shapes are defined, and these can be combined to obtain the desired shape.

RooRarFit [59] is a *BABAR* specific package that provides a simplified interface to RooFit, by simplifying common tasks, such as combining certain PDF shapes, or running toy Monte Carlo studies.

4.6.3.1 Toy Monte Carlo And Pull Distributions

PDFs are used for generating "toy" MC events, which are then refitted using the same PDFs. This tests for any biases in the likelihood function.

The events are generated using the Von Neumann accept / reject algorithm [60]. Random numbers are generated, these are then used to decided how the event is generated, in terms of where it lies in the N-dimensional space. The probability for the event to be accepted is

$$P_{accept}(\vec{x}) = \frac{\mathcal{L}(\vec{x})}{\mathcal{L}_{max}} \tag{4.16}$$

$\mathcal{L}(\vec{x})$ being the likelihood function at position $\vec{x}$. $\mathcal{L}_{max}$ is the maximum likelihood value. Another random number is generated, and if this is less than P_{accept} then the event is accepted, or otherwise it is thrown away. This is iterated until the desired number of events have been accepted.

Biases can exist due to very low statistics or a poorly constructed likelihood function. These biases must either be removed or account for. A large number of experiments are run, typically 500 for this analysis. For each event, a residual and pull are defined as follows

$$\text{residual} = \alpha_{gen} - \alpha_{fit} \tag{4.17}$$

$$\text{pull} = \frac{residual}{\sigma_{\alpha_{fit}}} \tag{4.18}$$

The pull should ideally be a Gaussian centered on zero, and have unit width.

Chapter 5

Analysis Method

5.1 Introduction

This chapter details the Maximum Likelihood method that was used to measure the branching fraction of the $B^{\pm} \rightarrow a_1^{\pm}(1260)\pi^0$ and $B^{\pm} \rightarrow a_1^0(1260)\pi^{\pm}$ decays. The procedure for selecting the events and ensuring that the fit has no intrinsic bias will be detailed. An investigation to look at the possible angular discriminating variables will also be described.

5.2 Overview

The extended maximum likelihood analysis of charged B-meson decays to $a_1\pi$ is carried out using a quasi-two-body approximation. An on-resonance dataset of $231.8 \times\ 10^6\ B\overline{B}$ events, corresponding to $210.5\,\text{fb}^{-1}$ was used.

The events are selected by using several kinematic and event shape variables. Particle identification selectors are used to remove kaon, electron and proton candidates. A veto is also applied for the $B^{\pm} \rightarrow a_1^0\pi^{\pm}$ mode to remove D^0 resonances.

Three main background sources are considered in this analysis:

- Continuum $q\overline{q}$ background: This consists of light quark production, and the events have a different topology to B-meson decays. Event shape cuts are used to remove continuum events, in particular $\cos\theta_{\rm T}$ has a large impact in removing this background.
- $B\overline{B}$ background: These are $B\overline{B}$ pairs, but not decaying to the signal $a_1\pi$ mode. The modes that contribute are identified by looking at simulated generic $B\overline{B}$ decays. The reconstruction efficiency and numbers of expected events for each mode are determined more accurately by reconstructing events from simulated exclusive $B\overline{B}$ decays. The $B\overline{B}$ background is split into two categories, one for $B\overline{B}$ charm and one for $B\overline{B}$ charmless, as the variables have different shapes for each of these. The overall normalisation of the $B\overline{B}$ charm PDF shape is floated in the final ML fit, whereas the $B\overline{B}$ charmless normalisations are fixed at the expected values. The corresponding PDF shapes are constructed by combining the Monte Carlo from the different $B\overline{B}$ decays in the correct ratios.
- Self cross-feed (SCF): This occurs when a track from an $a_1^+\pi^0$ or $a_1^0\pi^+$ is exchanged with a track from the rest of the event. The amount of SCF is determined from simulated, Monte Carlo events.

The final fit contains PDFs for the following fit components: signal, a_2, $q\overline{q}$, $B\overline{B}$ charm and $B\overline{B}$ charmless. The signal PDFs are obtained from MC events. The $q\overline{q}$ PDFs are obtained either from the on-resonance sidebands or off-resonance data. The charmless $B\overline{B}$ background PDFs are obtained from exclusive simulated MC events, whereas the charm $B\overline{B}$ background PDFs are determined using generic $B\overline{B}$ MC, in which all of the $B\overline{B}$ decays are simulated together in the correct ratios. As the $B\overline{B}$ charmless shapes are fixed in the final fit, it is important to determine the correct efficiency accurately, whereas for the $B\overline{B}$ charm which is floated this isn't necessary. The maximum likelihood fit is performed using the `RooRarFit` [59] package.

An initial fit is carried out to determine the PDF shape parameters from MC and these are then fixed in the final fit, carried out to the data. The yields of the signal, a_2, $q\overline{q}$ and $B\overline{B}$ charm components are floated in the final fit. Systematic errors on the branching fraction include the uncertainty of the PDF shapes, the normalisation of the fixed $B\overline{B}$ charmless backgrounds, and interference from a_2.

5.3 a_1 Angular Investigation

The validity of the analysis presented in Section 2.6.2 has been investigated on a Monte Carlo simulation of $B \to \pi_1 a_1$, $a_1 \to \pi_2 \rho$, $\rho \to \pi_3 \pi_4$ using the *BABAR* package GeneratorsQA which runs within the *BABAR* software framework. Using the same notation as in Section 2.6.2, the ρ meson is definitely identified with mesons 3 and 4. The $\pi_2 \rho$ wave function is simulated only as S wave, however in reality some D wave ($\sigma\pi$) may be present. The decay rate as written in Eq. (2.68), in the B rest frame can be written:

$$d\Gamma = |A|^2 |\vec{p}_1| \frac{dM_a dM_{23}^2 dM_{34}^2}{128 M_a M_B^2} d\Omega_1 d\cos\theta d\psi d\phi \tag{5.1}$$

where:

$$|A|^2 = |\alpha|^2 \cos^2\theta + \mathrm{Real}(\alpha\beta^*) \sin 2\theta \cos\psi + |\beta|^2 \sin^2\theta \cos^2\psi \tag{5.2}$$

and $|\vec{p}_1|$ is the momentum of meson 1 in the B rest frame. The angles Ω, θ and ψ are used consistent with the definitions in Section 2.6.2.

The decay rate must be independent of ϕ. Summing over all other variables of the simulation gives the distribution in ϕ as shown in Figure 5.1.

Summing Eq. (5.1) over Ω_1, the mass variables and ϕ gives the form:

$$d\Gamma = \Big[A\cos^2\theta + B\sin 2\theta\cos\psi + C\sin^2\theta\cos^2\psi\Big] d\cos\theta d\psi \tag{5.3}$$

Summing over $d\psi$ leaves:

$$d\Gamma = 2\pi \left[A\cos^2\theta + \frac{C}{2}\sin^2\theta\right] d\cos\theta \tag{5.4}$$

and summing Eq. (5.3) over $\cos\theta$ gives:

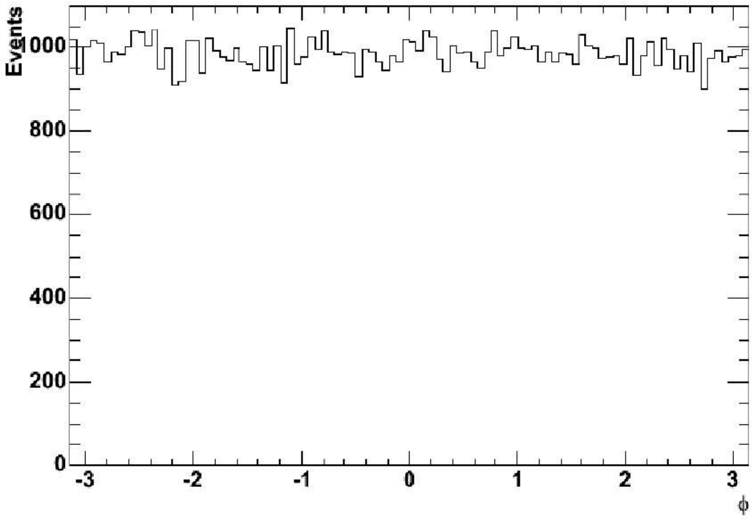

Figure 5.1: Helicity angle (ϕ) distribution

$$d\Gamma = \frac{2}{3}\left[A + 2C\cos^2\psi\right]d\psi \tag{5.5}$$

In the simulation, with π_2 taken in an S wave the distribution in $\cos\theta$ should be uniform, which in fact it is, as shown in Figure 5.2.

A uniform distribution implies $C = 2A$ and from Eq. (5.5):

$$d\Gamma = \frac{2A}{3}\left[1 + 4\cos^2\psi\right]d\psi \tag{5.6}$$

which is in agreement with the simulation distribution as shown in Figure 5.3

Figures 5.4, 5.5 and 5.6 show the distributions in M_{a_1}, M_{23} and M_{34} with the other five variables summed over, and Figure 5.7 shows the distribution in energy of the pions E_2, E_3 and E_4 in the rest frame of the B.

The decay of $B^+ \to \pi_0 a_1^+(a_1^+ \to \pi^-\pi^+\pi^+)$ has also been simulated by interchanging (p_2 and p_4) or (p_2 and p_3) at random in the Monte Carlo simulation package. π_2 comes from a ρ and is associated with the π^-. The two π^+ particles (π_3 and π_4) are distinguished

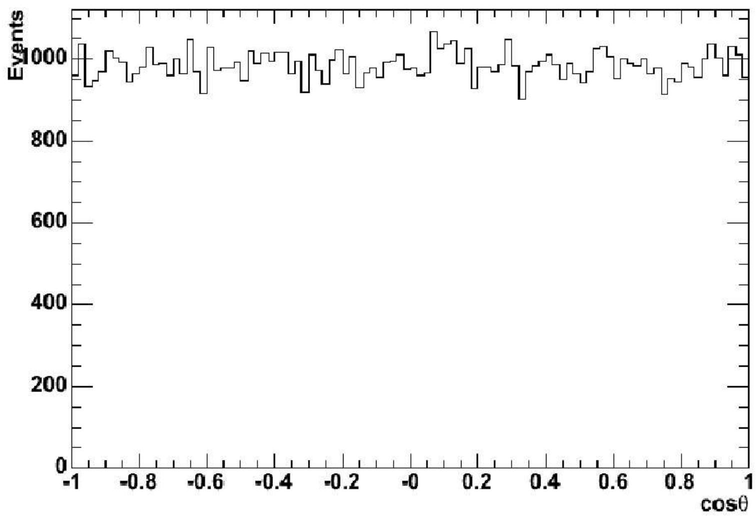

Figure 5.2: $\cos\theta$ distribution. θ is the angle between $\hat{p}_2$ and $\hat{p}_I$

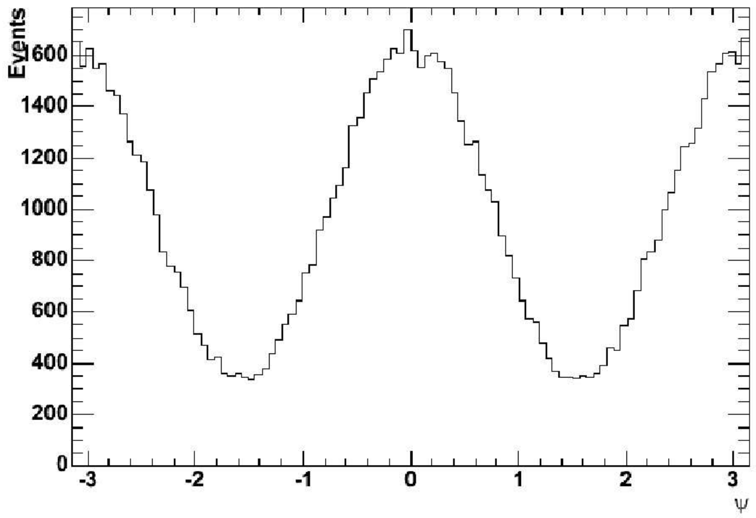

Figure 5.3: ψ distribution. ψ is the angle between the planes ($\hat{p}_2$, $\hat{p}_I$) and ($\hat{p}_3$, $\hat{p}_4$)

by imposing $M_{23}^2 < M_{24}^2 (E_3 < E_4)$. The simulation package does not impose Bose Einstein symmetry but this will only affect the expected interference patterns in the Dalitz type plots, not the angular distributions. The helicity angle ϕ is uniformly distributed. The distributions

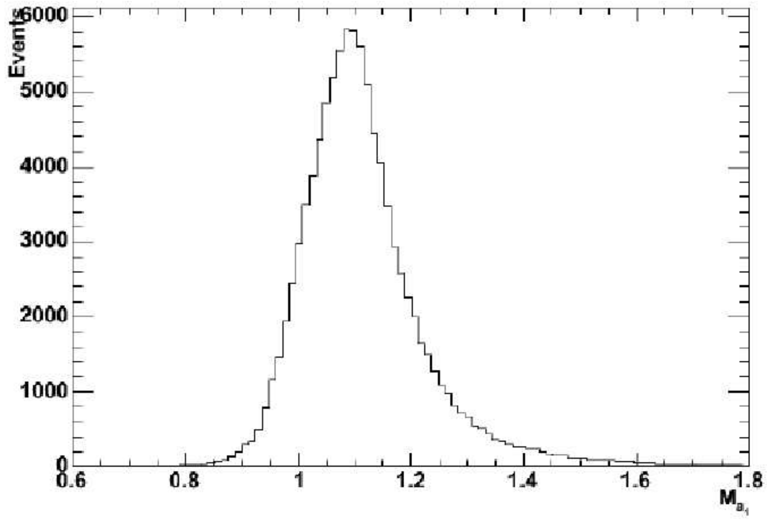

Figure 5.4: a_1 mass distribution (M_{a_1})

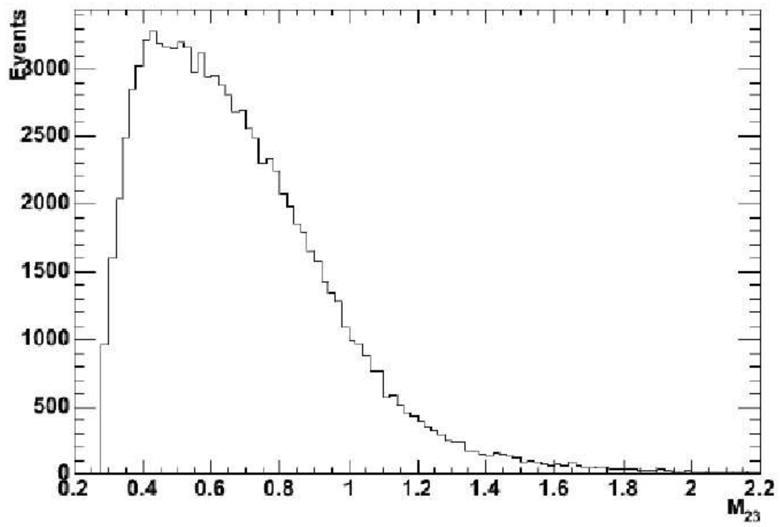

Figure 5.5: $\pi_2\pi_3$ invariant mass distribution (M_{23})

in $\cos\theta$ and ψ of Eqs. 5.4 and 5.5 shown in figures 5.8 and 5.9 . From Figure 5.8 it can been seen that $C \approx \frac{1}{5}A$, which implies

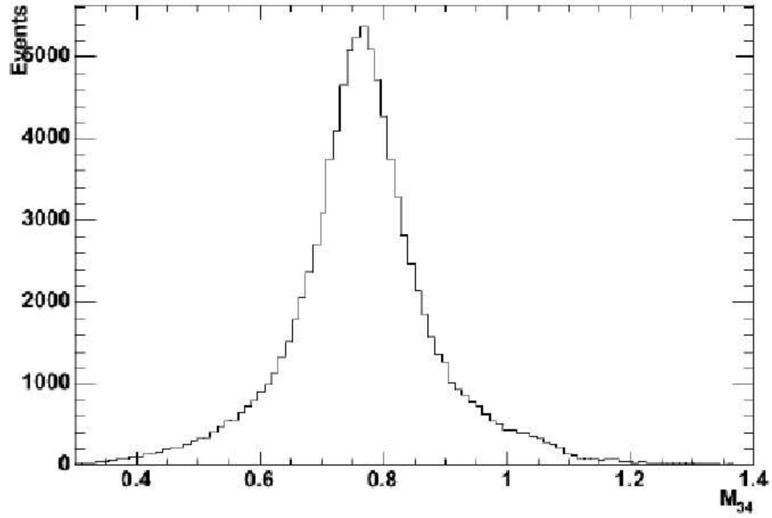

Figure 5.6: $\pi_3\pi_4$ invariant mass distribution (M_{34})

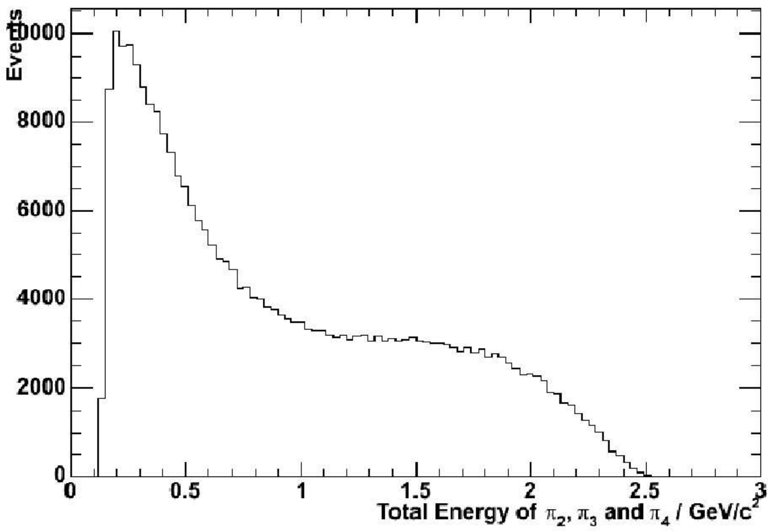

Figure 5.7: The energy distributions of π_2, π_3 and π_4 in the B rest frame

$$d\Gamma = \frac{2A}{3}\left[1 + \frac{2}{5}\cos^2\psi\right]d\psi \tag{5.7}$$

which is in agreement with Eq. (2.77).

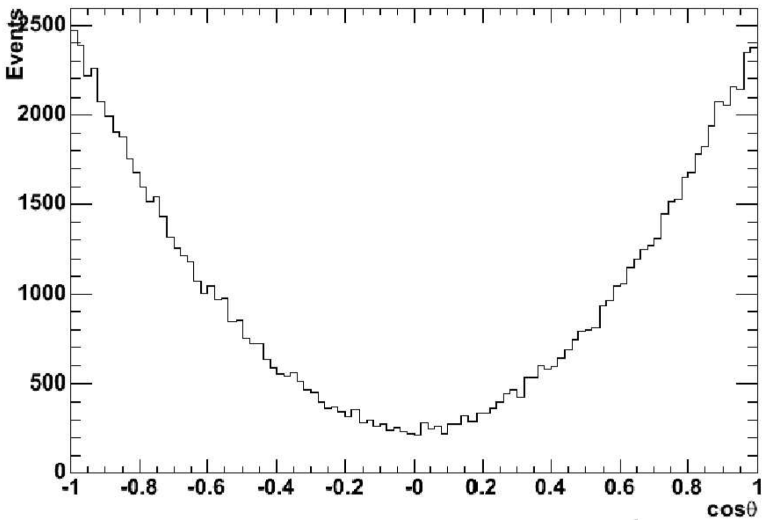

Figure 5.8: $\cos\theta$ distribution, interchanging momenta . θ is the angle between $\hat{p}_2$ and $\hat{p}_I$

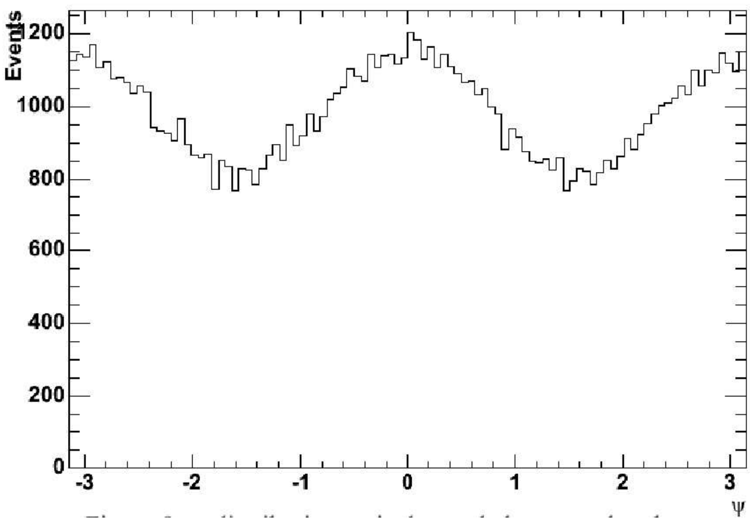

Figure 5.9: ψ distribution, ψ is the angle between the planes ($\hat{p}_2$, $\hat{p}_I$) and ($\hat{p}_3$, $\hat{p}_4$)

Figure 5.10 shows Dalitz type plots of M^2_{23} and M^2_{24} in three thin slices through phase space in the a_1 mass region. To better illustrate the ρ bands each event is represented by two points, one with $M^2_{23} < M^2_{24}$ and the other with them interchanged. The apparent uniformity of the distribution of points in the ρ bands is a feature to be expected of S wave production which, on average over all angles, will populate all the ρ helicity states.

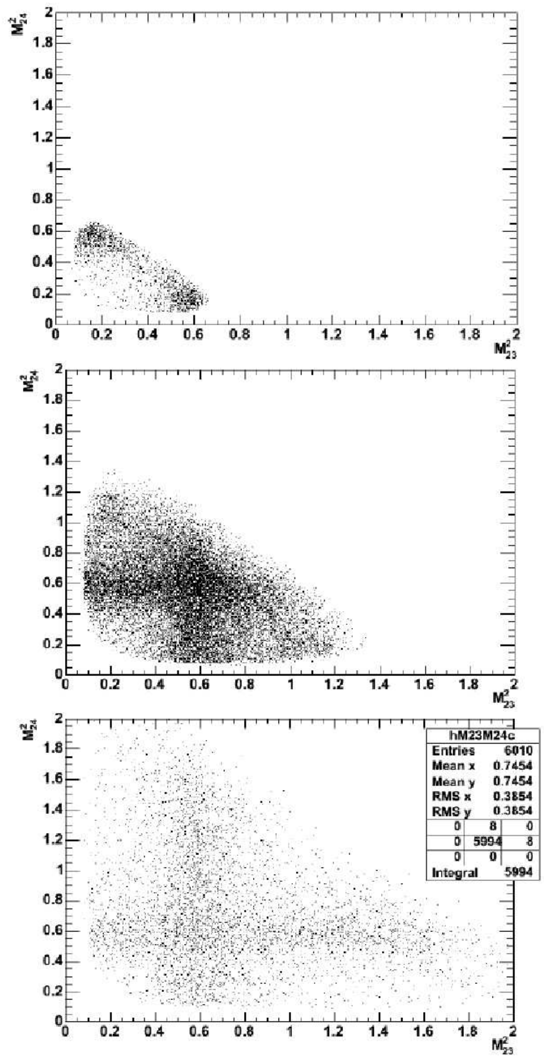

Figure 5.10: Dalitz type plots of M^2_{24} against M^2_{23} for slices through phase space where $0.91 < M_{a_1} < 0.95$ (top), $1.15 < M_{a_1} < 1.31$ (middle) and $1.45 < M_{a_1} < 1.61$ (bottom)

For the second reference orientation I take $\hat{p}_2 = \hat{x}$. $\hat{q}_2 = \hat{y}$, $\hat{n} = \hat{z}$. With reference to Eq. (2.73), applying a general rotation R gives the same form but with $\hat{p}_2$ replaced by $\hat{n}$, $\hat{q}_2$ replaced by $\hat{p}_2$ and $\hat{n}$ replaced by $\hat{q}_2$.

Given the momentum vectors the angular configuration of the star is then determined by the following relations:

$$
\begin{aligned}
\cos\theta &= \hat{p}_I.\hat{n} \qquad (5.8)\\
\sin\theta\cos\psi &= -\hat{p}_I.\hat{p}_2\\
\sin\theta\sin\psi &= \hat{p}_I.\hat{q}_2\\
\sin\theta\cos\phi &= \hat{n}.\hat{x}\\
\sin\theta\sin\phi &= \hat{n}.\hat{y}
\end{aligned}
$$

With these new Euler angles and from Eq. (2.76):

$$A = -\sin\theta(\alpha\cos\psi + \beta\sin\psi) \qquad (5.9)$$

Summing Eq. (5.1) over Ω_1, the mass variables and ϕ gives the form:

$$d\Gamma = \sin^2\theta\left[A\cos^2\psi + B\sin 2\psi + C\sin^2\psi\right]d\cos\theta d\psi \qquad (5.10)$$

and summing over $d\psi$ leaves:

$$d\Gamma = \pi\left[A + C\right]\sin^2\theta d\cos\theta \qquad (5.11)$$

Summing Eq. (5.3) over $\cos\theta$ gives:

$$d\Gamma = \frac{4}{3}\left[A\cos^2\psi + B\sin 2\psi + C\sin^2\psi\right]d\psi \qquad (5.12)$$

Figure 5.11 shows the distributions in $\cos\theta$ for the Monte Carlo simulation with π_3 and π_4 coming from the ρ. Figure 5.12 is the the $\pi^+\pi^+\pi^-$ simulation. Both exhibit the expected $\sin^2\theta$ behaviour. Figure 5.13 shows the ψ distribution with π_3 and π_4 coming from the ρ. From the reflection symmetry it appears that $B = 0$. It has already been found that $\frac{C}{A} = 2$ for this case, and from Eq. (5.10) it can be seen that the distribution follows the expected $\frac{4}{3}A\left[1 + \sin^2\psi\right]d\psi$ distribution. Figure 5.14 shows the ψ distribution with the $\pi^+\pi^+\pi^-$

simulation, and again it appears that $B = 0$. In this case it is found that $C \approx 1/5A$ and it can been that it follows the expected $\frac{4}{15}A\left[1 + 4\cos^2\psi\right]d\psi$ distribution.

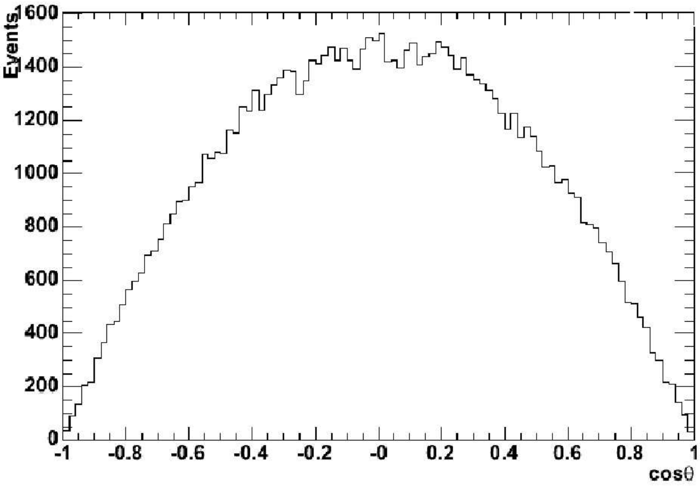

Figure 5.11: $\cos\theta$ distribution for $\rho \to \pi_3\pi_4$

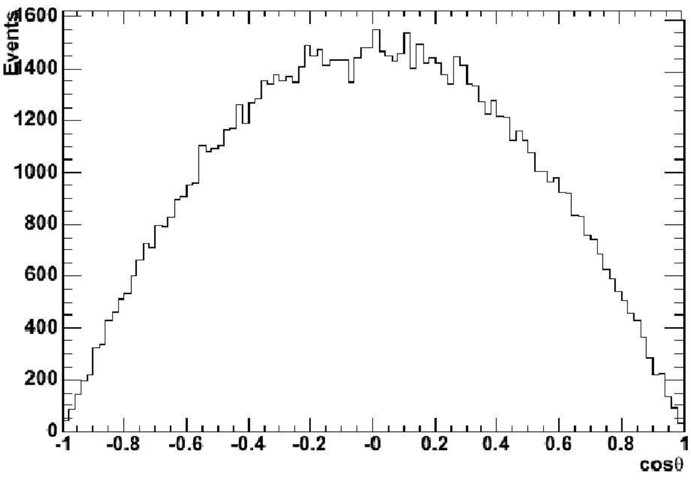

Figure 5.12: $\cos\theta$ distribution for $a_1 \to \pi_2\pi_3\pi_4$

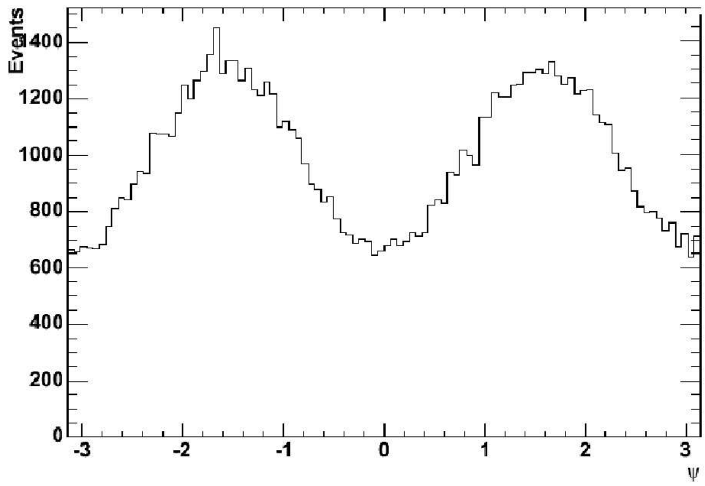

Figure 5.13: ψ distribution for $\rho \rightarrow \pi_3\pi_4$

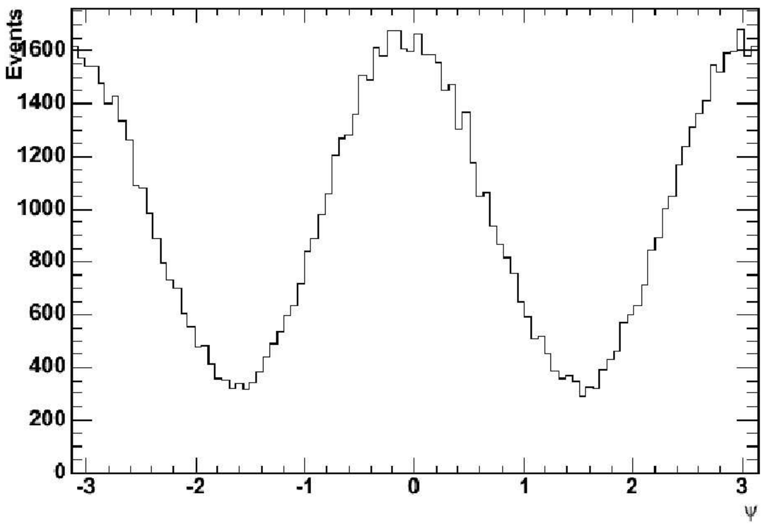

Figure 5.14: ψ distribution for $a_1 \rightarrow \pi_2\pi_3\pi_4$

5.4 Event Selection

The procedure to select events is as follows:

- Read events from the event store and *skim* them.
- Process the skimmed events, imposing more demanding criteria on some of the variables, and also calculating quantities such as event shape variables.
- Further select the final $a_1\pi$ state by imposing very tight requirements.

Each of these stages will now be discussed in further detail.

5.4.1 Event Preselection

The data is read from the *BABAR* event store, and a filter algorithm is applied. This selects inclusive B decays to 3 charged tracks and a neutral pion, by selecting all distinct combinations of these from the `GoodTracksLoose` and `pi0AllLoose` list. For each reconstructed B candidate, the following requirements are made:

- An energy constraint of $|\Delta E| < 0.310\,\mathrm{GeV}$. calculated in the lab frame.
- A requirement on the difference between the energy substituted mass and the beam energy in the centre of mass (CM) system, which is $|m_{ES} - \sqrt{s}/2| < 0.100\,\mathrm{GeV}$, where $\sqrt{s}/2 = 5.29$. The absolute value is used as m_{ES} may be larger than $\sqrt{3}/2$ due to misreconstruction.

This skim used is the *BABAR* `BFourBodyhhhp` skim. There is also an additional optional requirement placed on the B candidate thrust angle with respect to the rest of the event, which wasn't imposed here.

5.4.2 Batch Level Pre-Analysis

During this stage, the skim output is further refined. `Root` [58] ntuples are subsequently created using the `Q2BUser` package [61], which is based on the common *BABAR* framework. Using this package, the following criteria are applied:

- Photons are combined to form π^0 candidates. The unconstrained invariant mass is calculated and used for their selection. The mass is then constrained to the PDG value.
- For the $a_1^+\pi^0$ mode two charged tracks are combined to form a ρ^0 candidate. A ρ^0 is combined with a charged track to form an a_1^+ candidate.
- For the $a_1^0\pi^+$ mode a charged track and a π^0 are combined to form a ρ^+ candidate, which is then combined with another charged track to form a a_1^0 candidate.
- Vertexing of B candidates and calculation of ΔE and m_{ES}.
- Vertexing is re-performed, but with a mass constraint applied to the fitted B candidate.
- Particle selectors are run.
- Calculation of event shape variables.
- Calculation of quantities such as invariant mass, cosine of helicity angle and cosine of decay plane normal.
- The magnitude of $\cos\theta_{\mathrm{T}}$ must be < 0.9.

Separate ntuples are generated for both $B^\pm \to a_1^\pm\pi^0$ and $B^\pm \to a_1^0\pi^\pm$ decays.

5.4.3 Final Selection for $B^\pm \to (a_1\pi)^\pm$

Further selection criteria are applied after the skim and ntuple stages, in order to further suppress backgrounds. Reduced `Root` ntuples are created, these containing a smaller number of variables and events. The following selection criteria are applied and unless otherwise specified these are applied to both modes:

- $|\cos\theta_{\mathrm{T}}| \leq 0.65$. This helps to significantly reduce the continuum background.
- $|\Delta E| \leq 0.2$ GeV,

- $5.25 \leq m_{\rm ES} \leq 5.29 \ \mathrm{GeV}/c^2$. $m_{\rm ES}$ signal peaks above 5.72, but data is kept below this region to parameterise the continuum background, in the onpeak sideband region.

- $N_{\rm trks} \geq N_{\rm tracks\,in\,decay\,mode} + 1$. This ensures there is at least one charged track in the other event and hence that we have reconstructed a $B\overline{B}$ pair.

- $-2.5 <$ Fisher, $\mathcal{F} < 2.5$. This cuts around the peak in the MC signal distribution for the Fisher discriminant.

- $120 < m^{\pi^0}_{\gamma\gamma} < 150 \ \mathrm{MeV}/c^2$, a loose cut around the π^0 mass.

- $0.46 < m^{\rho}_{\pi\pi} < 1.1 \ \mathrm{GeV}/c^2$, a loose cut around the ρ mass.

- $0.8 < m^{a_1}_{\rho\pi} < 1.8 \ \mathrm{GeV}/c^2$, a loose cut around the a_1 mass.

- a_1 helicity $\mathcal{H} < |0.85|$, where $\mathcal{H}$ is the cosine of the a_1 decay angle. This is used to reduce some of the $B\overline{B}$ background.

- a_1 decay plane normal $-0.6 < \mathcal{A} < 0.6$, where $\mathcal{A}$ is the cosine of the decay plane normal angle. This helps to reduce the a_2 background.

- $p(\chi^2) > 0.01$, the probability of the χ^2 of the B vertex, which ensures that the B vertex has converged and that it is a good fit.

- a_1 momentum in CM system between 2.3 and $2.7 \ \mathrm{GeV}/c$. In the CM system, the two B mesons are produced at rest. We are looking at the two-body decay of a B to $a_1\pi$, so all of the energy of the B goes into $a_1\pi$ with each having a momentum of $\frac{1}{2}$ the total. This rejects against three-body decays.

- All charged pion candidates must NOT satisfy the `Tight` criteria of the electron `LH` selector, the `VeryTight` criteria of the proton `LH` selector and the `Tight` criteria of the kaon `LH` selector. This removes events that have electrons, kaons and protons instead of pions as the reconstructed charged tracks.

- For the $a_1^0\pi^+$ mode, DIRC pull of the bachelor track (using the pion hypothesis) between -2 and 3.5. The bachelor track is the track decaying directly from the B meson.

- For the $a_1^0\pi^+$ mode, $E_\gamma > 0.1\,\text{GeV}$ for each π^0 photon, which is to remove misreconstructed π^0 candidates that arise from accepting low energy photons. This isn't applied for the $a_1^+\pi^0$ mode, as the π^0 there decays directly from the B, and is high energy, therefore there is only a small chance of accepting low energy photons.

- For the $a_1^0\pi^+$ mode, a D veto is imposed, using the mass range $1.82\,\text{GeV}/c \leq m_{3\pi} \leq 1.90\,\text{GeV}/c$. If this criteria is satisfied for a single candidate, then the whole event is discarded.

A single candidate for each event is chosen, using the condition of the $\pi\pi$ mass nearest to the nominal ρ mass. For Monte Carlo, this algorithm selects the correct-combination candidate in $B^+ \to a_1^+\pi^0$ and $B^+ \to a_1^0\pi^+$ in 65% and 55% of events, respectively.

Table 5.1 and 5.2 show the cut efficiencies for both modes, for both Monte Carlo and data. These are defined relative to the number of events at the beginning of the final selection stage. The total efficiencies are shown at the bottom of the tables. For $B^+ \to a_1^+\pi^0$, before applying the preselection cuts, there were 1.29 multiple candidates on average for signal MC, and 1.20 for data. For $B^+ \to a_1^0\pi^+$, there were 1.83 multiple candidates for signal MC, and 1.56 for data.

5.4.4 Definition of Fitting Regions

The region as defined by the cuts previously mentioned is used to model the PDFs for the signal Monte Carlo. To model the continuum background, the on-resonance data is used, but ignoring the central signal region in the $(m_{\text{ES}}, \Delta E)$ plane. To model the m_{ES} shape, a cut of $|\Delta E| > 0.1\,\text{GeV}$ is made. To model the ΔE, $m_{a_1}$and $\mathcal{A}$ continuum shapes, on-resonance data with a cut of $5.25 < m_{\text{ES}} < 5.27$ is used. These regions are referred to as the ΔE sideband and grand-sideband, respectively. For the $\mathcal{F}$ continuum distribution, the off-

Table 5.1: Cut Efficiencies for $a_1^+\pi^0$ ($a_1^+ \to \rho^0\pi^+$). $115,000$ MC signal events are used.

Cut	Num Events Passing	Efficiency
No Cuts	115,000	1.000
Tag Bit Cuts	56,895	0.495
$\cos\theta_{\mathrm{T}}$	37,937	0.667
ΔE	33,326	0.878
N_{trks}	33,242	0.997
m_{ES}	29,997	0.902
Fisher, $\mathcal{F}$	29,899	0.997
m_{a_1}	29,660	0.992
m_ρ	29,660	1.000
m_{π_0}	28,503	0.961
$p(\chi^2)$	25,241	0.886
$\mathcal{H}$	22,812	0.904
$p_{a_1}^{CM}$	20,898	0.916
$\mathcal{A}$	16,083	0.770
$K^\pm$ Veto	15,269	0.949
e^- Veto	15,183	0.994
Proton, p Veto	15,045	0.991
Total	15,045	0.131

resonance data is used. This is to eliminate the effect of $B\overline{B}$ backgrounds that are present in the on-resonance sideband, for this variable. However, it is still preferable to use the sideband data for the other variables, as this contains higher statistics than the off-resonance data.

Figures 5.15 to 5.22 show the cut variables after the preselection cuts were applied.

Table 5.2: Cut Efficiencies for $a_1^0\pi^+$ ($a_1^0 \to \rho^\pm\pi^\mp$). $159,000$ MC signal events are used.

Cut	Num Events Passing	Efficiency
No Cuts	159,000	1.000
Tag Bit Cuts	98,998	0.623
$\cos\theta_{\mathrm{T}}$	62,753	0.634
ΔE	54,765	0.873
N_{trks}	54,648	0.998
m_{ES}	48,600	0.889
Fisher, $\mathcal{F}$	48,436	0.997
m_{a_1}	47,916	0.989
m_ρ	47,851	0.999
m_{π_0}	46,214	0.966
E_γ	32,456	0.702
$p(\chi^2)$	29,071	0.896
$\mathcal{H}$	26,107	0.898
$p_{a_1}^{CM}$	23,200	0.889
$\mathcal{A}$	17,867	0.770
$K^\pm$ Veto	16,671	0.933
e^- Veto	16,610	0.996
Proton, p Veto	16,415	0.988
DIRC Pion Pull	13,866	0.845
D Veto	11,965	0.863
Total	11,965	0.0753

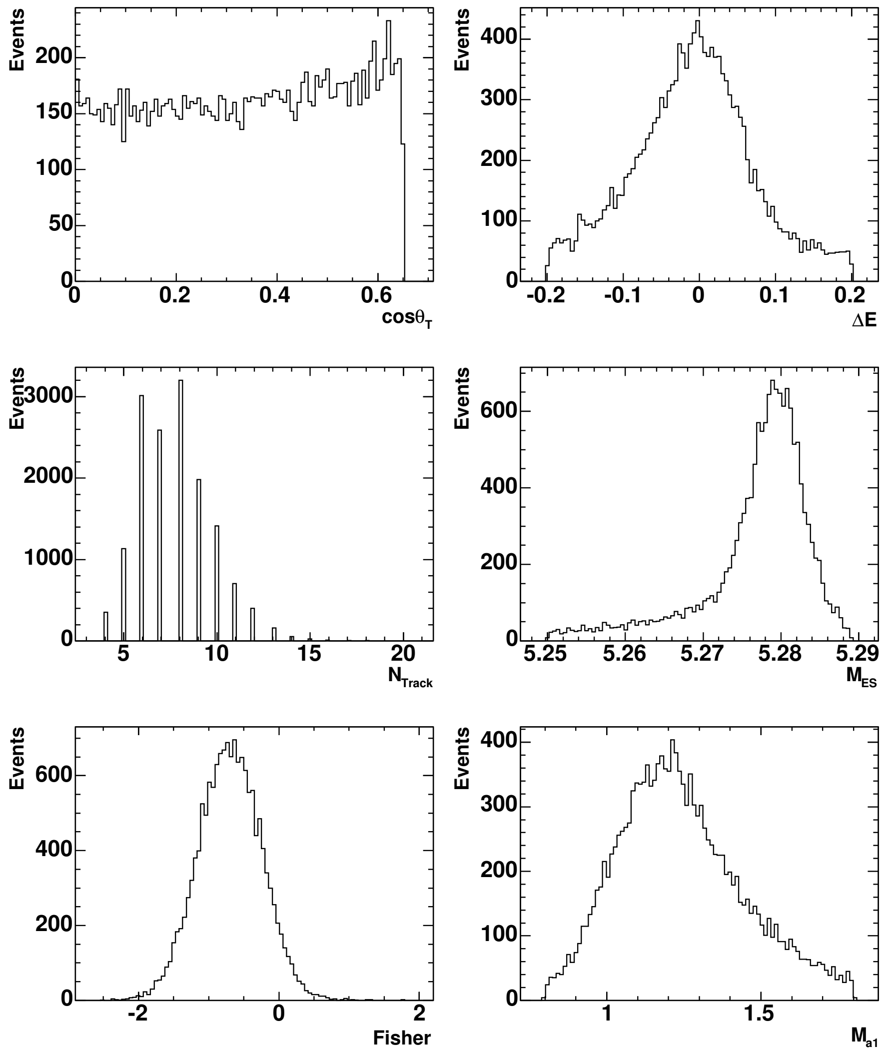

Figure 5.15: Cut Variables for $a_1^{+}\pi^0$ Signal Monte Carlo, for $\cos\theta_{\mathrm{T}}$, ΔE, N_{trks}, m_{ES}, $\mathcal{F}$ and m_{a_1}

The number of signal events can be estimated by using the number of $B\overline{B}$ pairs, $N_{B\overline{B}}$, the reconstruction efficiency of the signal Monte Carlo, ϵ. The efficiency must also be corrected by tracking and neutral differences between data and Monte Carlo, to give the corrected efficiency, ϵ_{corr}. For this analysis, the total correction is a factor of 0.955, and the number of expected signal events are given by:

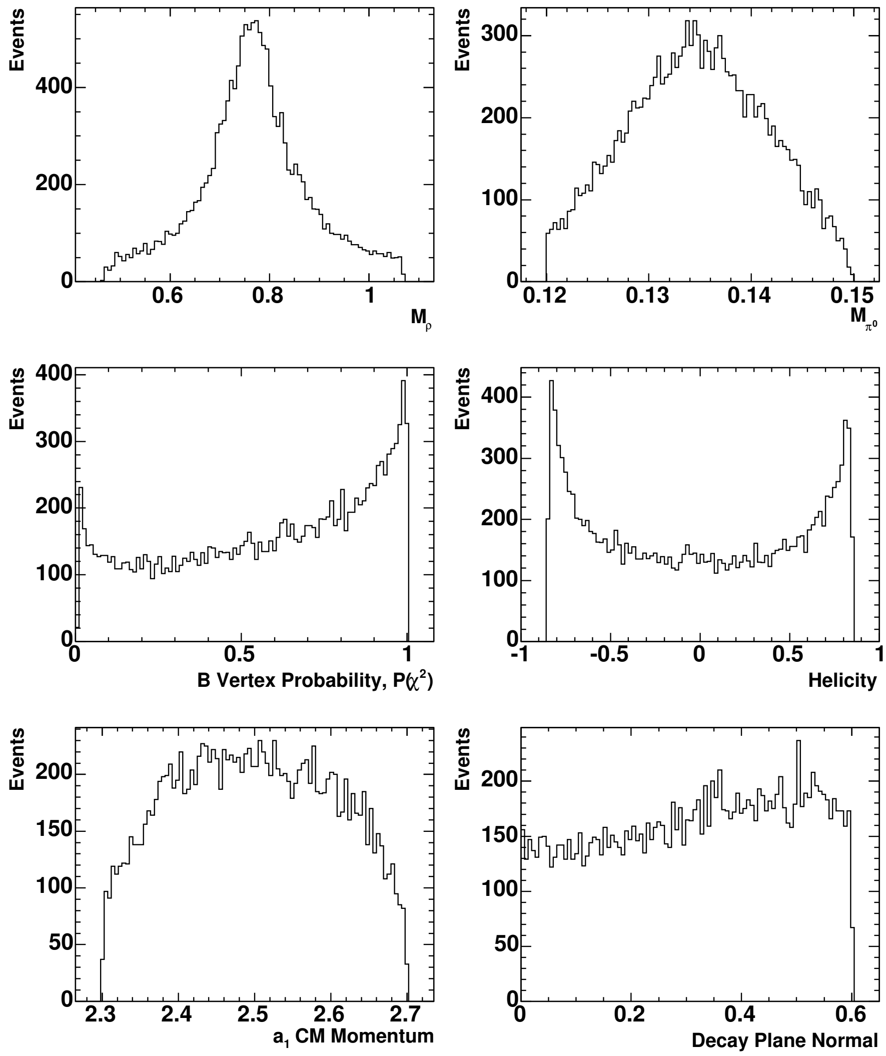

Figure 5.16: Cut Variables for $a_1^+\pi^0$ Signal Monte Carlo, for m_ρ, m_{π_0}, $p(\chi^2)$, $\mathcal{H}$, $p_{a_1}^{CM}$, $\mathcal{A}$

$$S = \epsilon_{corr} N_{B\bar{B}} \mathcal{B} \tag{5.13}$$

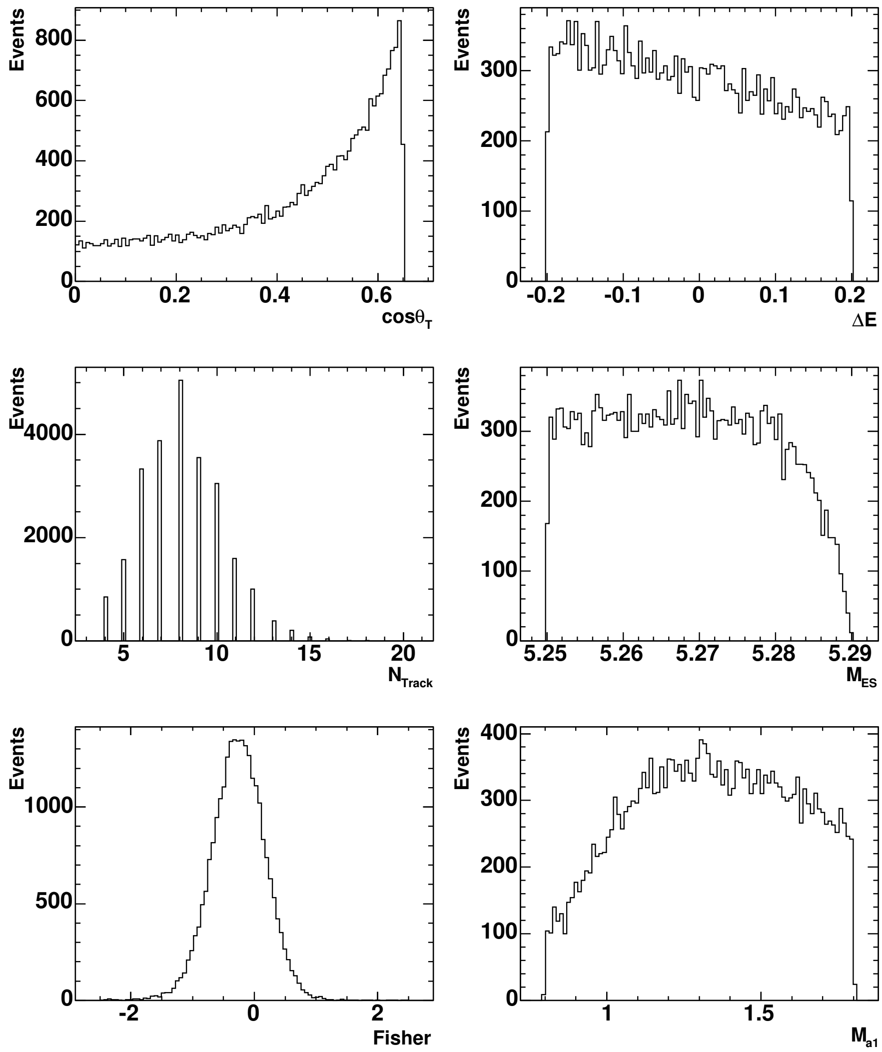

Figure 5.17: Cut Variables for $a_1^+\pi^0$ OnPeak Sidebands, for $\cos\theta_{\mathrm{T}}$, ΔE, N_{trks}, m_{ES}, $\mathcal{F}$and m_{a_1}

5.5 Background Determination

There is a large amount of background present in rare charmless analyses. This section will describe the methods used to reduce the various backgrounds, and how to model those that remain.

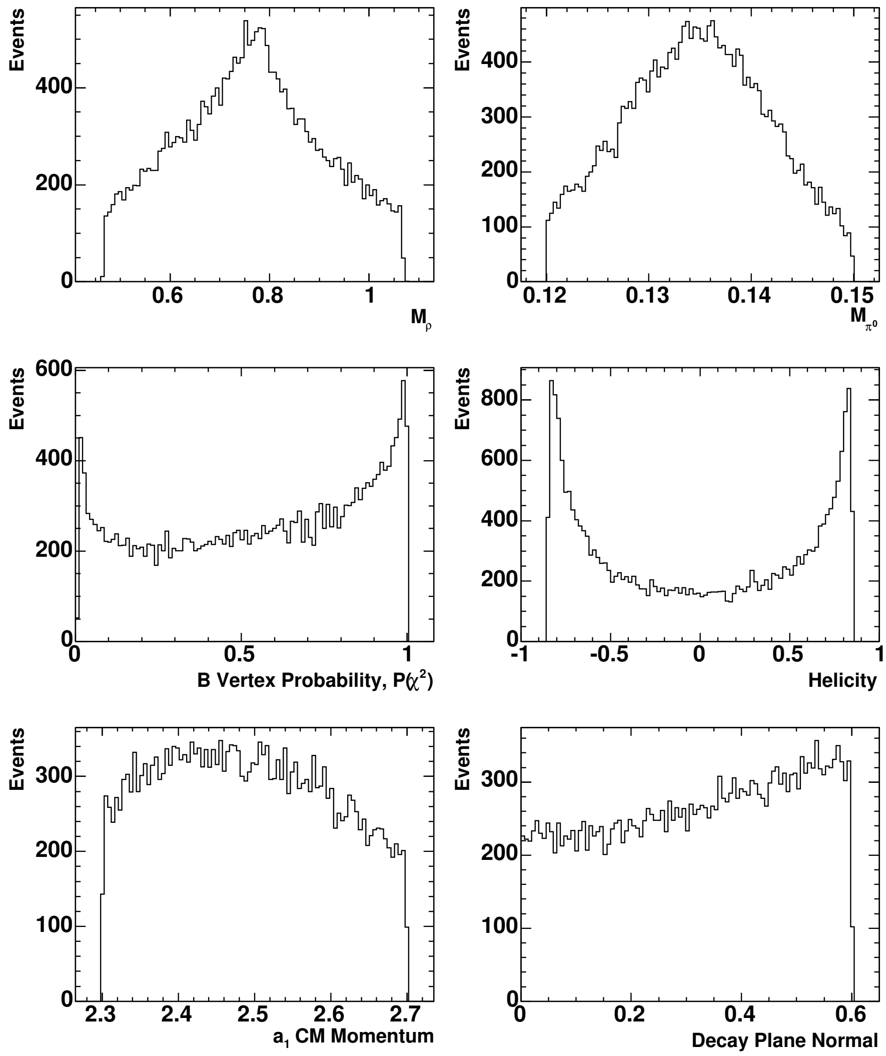

Figure 5.18: Cut Variables for $a_1^{+}\pi^0$ OnPeak Sidebands, for m_ρ, m_{π_0}, $p(\chi^2)$, $\mathcal{H}$, $p_{a_1}^{CM}$ and $\mathcal{A}$

5.5.1 $B\overline{B}$ Background

$B\overline{B}$ background consists of B meson decays to modes other than the signal mode, $B \to a_1\pi$. The reconstruction algorithms are run on generic $B\overline{B}$ MC, and the MC truth information is used to identify the most prominent $B\overline{B}$ backgrounds. The generic $B\overline{B}$ MC consists of samples of 174 million generic B^+B^- and 148 million generic $B^0\overline{B}^0$, which is equivalent to a luminosity of $116\,\mathrm{fb}^{-1}$ and $99\,\mathrm{fb}^{-1}$ respectively. $B\overline{B}$ background can be split into the following categories:

- Pure combinatorics: A $B\overline{B}$ event has three unrelated tracks and two unrelated photons. These events have a very similar m_{ES} distribution to continuum background events.
- Signal self crossfeed: These arise when a track from a $a_1^+\pi^0$ or $a_1^0\pi^+$ is exchanged with a track from the rest of the event. The amount of SCF present is estimated from MC studies, and SCF is taken as part of the signal hypothesis in the ML fit. This means that separate PDFs are formed from the SCF MC, but that as shown in Eq. (5.16) the SCF events are used to measure the total signal branching ratio.
- $B\overline{B}$ backgrounds from particle misidentification, for example pion/kaon misidentification. The effect of $B \to a_1 K$ is taken as a systematic error on the branching fraction.
- $B \to D$ decays also contribute, owing in part to their relatively high branching fraction. The variables have similar shapes to the continuum background events.
- Two and four-body charmless decays contribute, for example, $B \to a_1\rho$. This occurs when a particle is lost in reconstruction, usually a low momentum particle, or when a track from the other B in the event is incorrectly attributed to the reconstructed signal B.

After carrying out the selection cuts, the remaining $B\overline{B}$ is modelled using exclusive MC samples to quantify them and obtain distributions.

Tables 5.3 and 5.4 show the most dominant charmless $B\overline{B}$ modes that were taken into account for both modes. These tables show the *BABAR* mode number corresponding to the Monte Carlo sample; the MC selection efficiencies after all the preselection cuts have been applied; the estimated branching fractions. The expected number of $B\overline{B}$ events are calculated from the reconstruction efficiencies, and the current world average branching fractions for each of the modes, taken either from the Particle Data Group tables [18] or from the Heavy Flavor Averaging Group [62]. The product branching fraction represents the resonance daughter decay, also obtained similarly. The estimated number of preselection events is calculated by using Eq. (5.14).

$$N_{\text{Est}} = N_{B\overline{B}} \times \mathcal{B} \times \mathcal{B}_{dtr} \times \varepsilon \tag{5.14}$$

where $N_{B\overline{B}} = 232 \times 10^6$ is the integrated luminosity for *BABAR* Runs 1 to 4, corresponding to the dataset analysed here; $\mathcal{B}_{dtr}$ is the specific charmless $B\overline{B}$ daughter branching fraction and ε is the MC efficiency.

Table 5.3: Charmless $B\overline{B}$ backgrounds for the $a_1^+\pi^0$ mode.

Group	Bkg. Channel	*BABAR* Mode num	MC ε (%) (%)	Est. $\mathcal{B}$ (10^{-6})	$\prod \mathcal{B}_i$ (%)	Est. presel. (events)
A	$B^+ \to a_1^+\pi^0(a_1^+ \to \rho^+\pi^0)$	4957	0.2930	42.6	50	14.5
	$B^0 \to a_1^+\pi^-(a_1^+ \to \rho^+\pi^0)$	4951	0.0590	33.4	50	2.3
	$B^0 \to K_s^0\rho^0$	5221	0.2175	5.1	0.34	0.9
B	$B^0 \to B^0 \to \omega\pi^0$	2362	1.1047	1.2	100	3.1
C	$B^+ \to \rho^+\rho^0$	2390	1.6713	26.4	100	102.3
D	$B^0 \to \rho^+\rho^-$	2498	0.3598	30	100	25.0
E	$B^+ \to f^0\rho^+$	4755	2.633	4.0	100	24.4
F	$B^0 \to K^{*0}(K^+\pi^-)\pi^0$	1225	0.8196	1.7	100	3.2
G	$B^+ \to \rho^+\pi^0$	1940	0.3604	12	100	10.0
H	$B^0 \to \eta'_{\rho\gamma}\pi^0$	2847	3.9212	3.7	30	9.9
I	$B^+ \to \rho^+K^{*0}(K^+\pi-)(L, f_L = 1)$	2244	0.2851	10.5	100	6.9
J	$B^+ \to \omega\rho^+$	2768	0.1005	12.6	100	2.9
K	$B^+ \to \eta'_{\rho\gamma}\rho^+$	2775	0.8152	22	30	12.3
L	$B^+ \to a_1^0\rho^+(L, f_L = 1)$	3999	0.3565	48	50	39.7
	$B^+ \to a_1^+(\rho^+\pi^0)\rho^0(L, f_L = 1)$	4107	0.1941	48	50	10.8
	$B^+ \to a_1^+(\rho^+\pi^0)\rho^-(L, f_L = 1)$	4001	0.0802	84	50	7.8
M	$B^+ \to a_1^+(\rho^0\pi^+)\rho^-(L, f_L = 1)$	4002	1.0109	84	50	98.4
	Total					367.3

Table 5.4: Charmless $B\overline{B}$ backgrounds for the $a_1^0\pi^+$ mode.

Group	Bkg. Channel	Mode #	MC ε (%)	Est. $\mathcal{B}$ (10^{-6})	$\prod\mathcal{B}_i$ (%)	Est. presel. (events)
A	$B^+ \to \rho^0\pi^+$	1220	1.285	9.1	100	27.1
	$B^+ \to K^{*0}\pi^+$	1051	0.536	9.7	100	12.0
B	$B^+ \to \omega\pi^+$	1248	1.590	5.9	100	21.7
	$B^+ \to \omega K^+$	1250	0.082	5.1	100	0.97
C	$B^+ \to \rho^+\rho^0$	2390	2.303	26.4	100	140.96
	$B^0 \to \rho^+\rho^-$	2498	1.196	30	100	83.2
	$B^0 \to \rho^0\rho^0$	2396	3.384	1.1	100	8.63
	$B^0 \to K_2^{*+}\pi^-(K_2^{*+} \to K^+\pi^0)$	4730	0.4063	13.2	50	6.20
D	$B^+ \to f^0\rho^+$	4755	1.905	4	100	17.7
	$B^0 \to a_1^+\pi^-(a_1^+ \to \rho^0\pi^+)$	4950	2.4825	33.4	50	96.1
	$B^0 \to a_1^+\pi^-(a_1^+ \to \rho^+\pi^0)$	4951	1.511	33.4	50	58.5
E	$B^+ \to \eta'_{\rho\gamma}K^+$	1508	0.119	70.8	30	5.74
F	$B^+ \to \omega\rho^+$	2768	0.144	12.6	100	4.19
G	$B^+ \to \eta'_{\rho\gamma}\rho^+$	2775	0.712	22	30	10.71
H	$B^+ \to K_2^{*0}\pi^+(K_2^{*0} \to K^+\pi^-)$	4747	0.561	2.3	50	1.49
I	$B^+ \to a_1^+(\rho^+\pi^0)\rho^0(L, f_L = 1)$	4107	0.5140	48	50	28.6
	$B^+ \to a_1^+(\rho^0\pi^+)\rho^0(L, f_L = 1)$	4105	0.6832	48	50	38.0
	$B^+ \to a_1^+(\rho^+\pi^0)\rho^-(L, f_L = 1)$	4001	0.2585	84	50	25.2
	$B^+ \to a_1^+(\rho^0\pi^+)\rho^-(L, f_L = 1)$	4002	0.4364	84	50	42.5
J	$B^0 \to \rho^-\pi^+$	1229	0.823	24	100	45.8
	Total					755.1

5.5.2 $q\overline{q}$ Background

The $q\overline{q}$ background is the largest source of background. B mesons are produced almost at rest in the $\Upsilon(4S)$ rest frame, so there is no preferred direction for their decay products. The event is said to be "spherical".

Continuum events are produced with high momentum, and so their decay products form two highly collimated, back-to-back jets. Event topology variables are used to discriminate between signal and continuum events. The remaining $q\overline{q}$ background is modelled using either on-resonance sideband samples, or using off-resonance data. The on-resonance data sideband sample also contains backgrounds from B meson decays.

To generate the resonance mass continuum distribution, a $B\overline{B}$ background subtraction procedure is applied. The onpeak sideband distribution is used, but the shape for the $B\overline{B}$ background obtained from generics is subtract from this. The normalisation of the subtraction is fixed at the expected value from MC. This helps with $B\overline{B}$ events being present in the onpeak sideband regions.

5.6 PDF Descriptions

5.6.1 Splitting the signal component

The ML method assumes that the components and variables of the fit are uncorrelated, but correlations may introduce biases. Because of correlations present in the signal component, it was split into truth matched and self crossfeed (SCF) sub-components, S_{TRU} and S_{SCF}.

Correlations are calculated using:

$$\rho_{x,y} = \frac{cov(x,y)}{\sigma_x \sigma_y} \tag{5.15}$$

and splitting the signal, S component gives:

$$\mathcal{P}_S = (1 - f_{SCF})\mathcal{P}_{S_{TRU}} + f_{SCF}\mathcal{P}_{S_{SCF}} \tag{5.16}$$

where f_{SCF} is the fraction of SCF as determined from signal Monte Carlo. As an example, figures 5.23 and 5.24 show scatter plots displaying the correlations between the two most correlated variables, $\Delta E$and M_{a_1}, for both truth matched MC and non-truth matched MC (SCF). By splitting the signal component, the correlations are contained in the SCF component, and this helps reduce the intrinsic bias from the fit, as measured using toy MC.

5.6.2 Data Samples

The functional forms and parameter values are determined by unbinned, one-dimensional fits to a Monte Carlo sample, where $B \to a_1\pi$ is simulated. The fraction of self crossfeed, f_{SCF} is determined from Monte Carlo to be 35% and 44%, respectively for the two modes.

$q\overline{q}$ fits are performed on either the on-resonance sideband data or off-resonance data, depending on the variable. $B\overline{B}$ generic charm and $B\overline{B}$ exclusive charmless data samples are used to parameterize the $B\overline{B}$ background components. The a_2 background component is derived from Monte Carlo of exclusive B decays to $a_2\pi$.

The functional forms of the PDFs are fixed in the final fit to the on-resonance sample. Almost all of the parameters are also fixed, to ensure a stable fit. For example, f_{SCF} is fixed in this final fit.

5.6.3 ΔE PDFs

For $B^+ \to a_1^0\pi^+$, a 2-dimensional Keys PDF is used to parameterize the ΔE-m_{a_1}shapes, for both true and self-crossfeed signal. For $B^+ \to a_1^+\pi^0$, a double Gaussian shape is used to parameterize each of the true and self crossfeed signal and a_2 distributions. For the real signal component the second Gaussian is asymmetric.

For continuum background the on-resonance data is selected in the $m_{\rm ES}$ sideband as defined above. The resulting distribution is fit by a second order polynomial. For $B\overline{B}$ charmless background, the distributions are fit by combinations of Gaussians and polynomials. For $B\overline{B}$ charm background, a second order polynomial is used.

5.6.4 m_{ES} PDFs

The m_{ES} distribution of true signal Monte Carlo event is fit with a Gaussian plus a crystal ball function. The self crossfeed component is fit with a one dimensional Keys shape for $a_1^+\pi^0$, and a triple Gaussian for $a_1^0\pi^+$.

For background on-resonance data in the ΔE sidebands, as defined above, is used. This is fit with an Argus function. For charmless $B\overline{B}$ background, the distributions are fit with either an Argus, double Gaussian or 1-dimensional Keys shapes. For the charm $B\overline{B}$ background, a one dimensional Keys PDF is used.

5.6.5 m_{a_1} PDFs

The PDFs for the a_1^+ and a_1^0 resonance invariant mass are obtained from signal MC samples. The signal a_1 resonance mass shape is fit with a relativistic Breit Wigner shape, for $a_1^+\pi^0$. For the final fit, the mean and width parameters are fixed at $1.23\ \mathrm{GeV}/c^2$ and $393\ \mathrm{MeV}/c^2$ respectively. The self crossfeed is fit with a double Gaussian. For $a_1^0\pi^+$, the signal shapes are fit with two dimensional Keys PDFs, ΔE being the other variable. The a_2 component is fit with a double Gaussian PDF.

The continuum background shapes consist of the sum of a third order quadratic component, to describe the combinatorics, a peak of real resonances and a generic $B\overline{B}$ shape, which is subtracted in the later fit stages. For charmless $B\overline{B}$ background, the distribution is fit with either double or triple Gaussians, or a one dimensional Keys PDF. For the charm $B\overline{B}$ background, a third order Chebychev polynomial is used for $a_1^+\pi^0$, and a one dimensional Keys PDF for $a_1^0\pi^+$.

5.6.6 $\mathcal{A}$ PDFs

All components except for the charmless $B\overline{B}$ backgrounds are parameterized by second or third order polynomials. The charmless backgrounds are parameterized by either polynomials or multiple Gaussians.

5.6.7 $\mathcal{F}$ PDFs

The shape used for all components is an asymmetric Gaussian. This shape gives a good fit for signal but in order to account for outliers, an additional Gaussian contribution is used for continuum and $B\overline{B}$ charm background. Also, data taken off resonance is used to parameterize the continuum background.

5.7 Fit Validation

The PDFs are combined to form a prototype fit model. This model must be verified to ensure that it behaves as expected, and does not return biased results. The effect of $B\overline{B}$ backgrounds on the fit behaviour was also studied.

5.7.1 Toy MC and Toy Tests

The PDFs are used both fitting and to generate the toy MC. This is a similar, but statistically independent sample to the on-resonance data, to run the fit on. Numerous experiments are run, where one experiment consists of generating an independent dataset and applying the fit to extract the floated PDF parameters and yields. The samples differ by statistical fluctuations.

The pull distribution also tests error coverage. The Gaussian width of the pull distribution should be unity. Deviations indicate error undercoverage (width > 1) or error overcoverage (width < 1).

5.7.2 Pure Toy Tests

These are used to check for fit instabilities and intrinsic biases, and also for fit error studies. A single pure toy test consists of numerous experiments, here this is 500. Each component (signal, $q\overline{q}$ background, a_2, $B\overline{B}$ charm, $B\overline{B}$ charmless) are sampled using the PDFs.

The number of events generated for each hypothesis is varied around a mean value, using the Poisson distribution. This is termed "Poisson smearing". The mean value is determined by the number of events expected in the final on-resonance sample. An extended ML fit is applied to extract the floated PDF parameters and the yields. A Gaussian is fitted to the pull distribution. For an unbiased model with correct error coverage, this Gaussian should be centred on zero with unit width.

Table 5.5 shows the results from pure toy MC studies for both decay modes. Figures 5.25 and 5.26 show the signal yield, error on the signal yield and the signal yield pull distributions for both modes, respectively.

Table 5.5: Summary of results from pure toy MC studies for both decay modes. In each case 500 toy experiments have been used. The mean N_{sig} is taken from the average over all experiments.

Mode	N_{total}	N_{sig} (input)	$N_{B\overline{B}}$ (input)	N_{sig} (fit)	$\sigma(N_{sig})$ (fit)	Bias [ratio]
$a_1^+\pi^0$	24,608	241	367	236.5 ± 3.2	61.8	0.98 ± 0.01
$a_1^0\pi^+$	33,375	277	755	281.4 ± 3.3	64.1	1.02 ± 0.01

5.7.3 Toy Tests with embedded signal events

The toy tests are repeated, but this time using fully simulated MC events for the signal component. This involves taking random samples from the available MC.

These tests look for any subtle correlations between the fit variables, giving rise to biases. Here we are not concerned with validating the error coverage.

Table 5.6 shows the results from toy experiments using simulation signal events. Figures 5.27 and 5.28 show the signal yield, signal yield error, and the signal yield pull distributions for both modes, respectively.

Table 5.6: Summary of toy experiments from samples containing embedded SP5/SP6 MC signal events, with continuum events, a_2 and $B\overline{B}$ (both charm and charmless) generated from PDFs. The $B\overline{B}$ components are fixed

Mode	N_{total}	N_{sig} (input)	Mean N_{sig} (fit)	bias [ratio]	bias [evts]
$a_1^+\pi^0$	24,608	241	273.4 ± 4.0	1.13 ± 0.02	$+32.4 \pm 0.5$
$a_1^0\pi^+$	33,375	277	293.4 ± 3.6	1.06 ± 0.01	$+16.4 \pm 0.2$

5.7.4 Fully Embedded Toy Tests

The toy tests are repeated again, but using simulated events for all components except for the continuum now.

Table 5.7 shows the results from these toy experiments. Figures 5.29 and 5.30 show the signal yield, signal yield error, and the signal yield pull distributions for both modes, respectively.

Table 5.7: Summary of toy experiments from samples containing embedded SP5/SP6 MC signal, a_2 and charmless/charm $B\overline{B}$ background events, with continuum events generated from the PDFs. The charmless $B\overline{B}$ components are fixed.

Mode	$a_1^+\pi^0$	$a_1^0\pi^+$
N_{total}	24,608	33,375
N_{sig} (input)	241	277
N_{a_2} (input)	35	36
$N_{B\overline{B}charmless}$ (input)	367	5295
$N_{B\overline{B}charm}$ (input)	1721	755
Mean N_{sig} (fit)	281.9 ± 3.1	322.1 ± 3.5
Mean N_{a_2} (fit)	26.5 ± 3.1	19.6 ± 2.9
Mean $N_{B\overline{B}charm}$ (fit)	1637 ± 5.5	5043 ± 8
Signal bias [ratio]	1.17 ± 0.01	1.16 ± 0.01
Signal bias [evts]	$+40.9 \pm 0.4$	$+45.1 \pm 0.5$

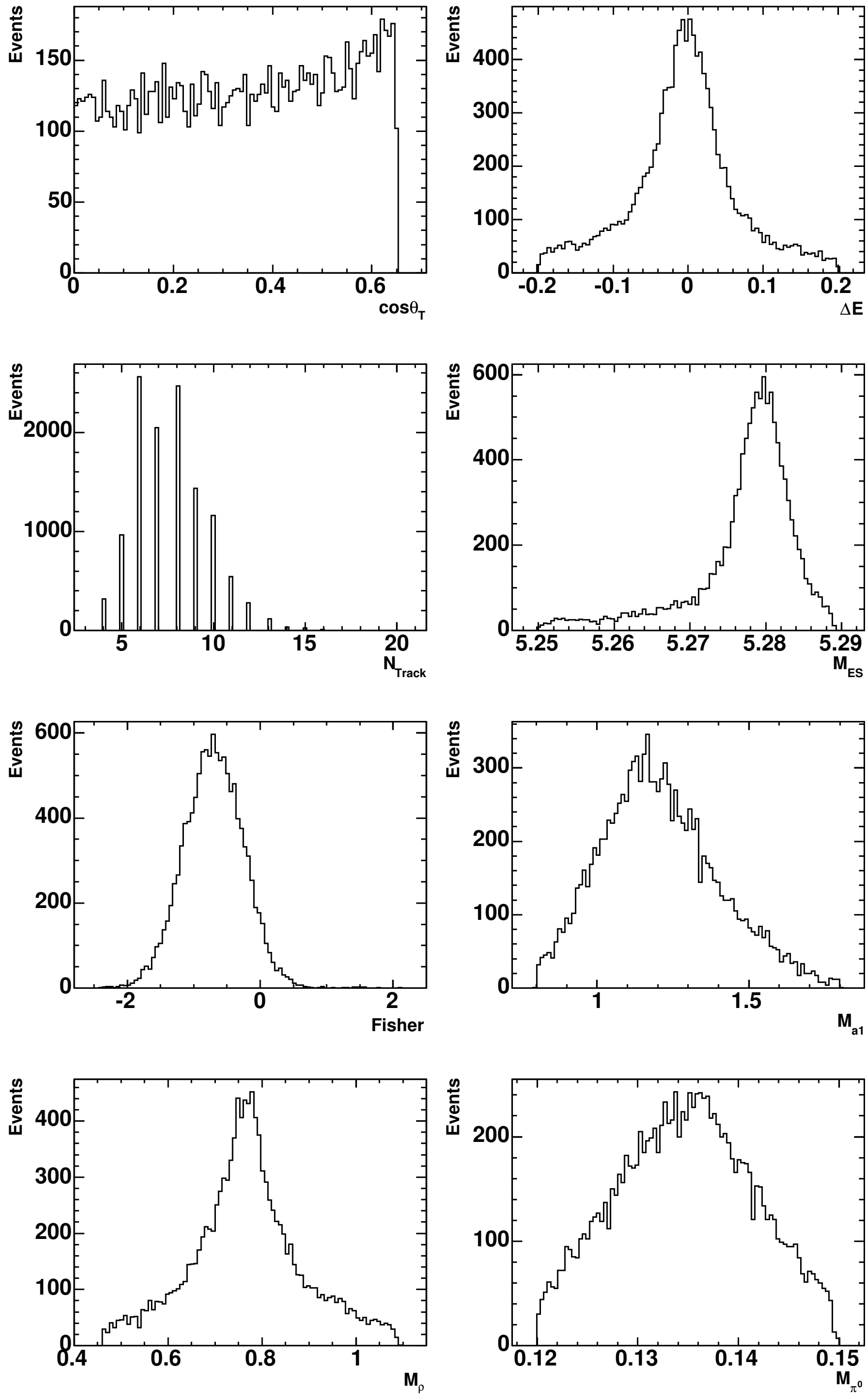

Figure 5.19: Cut Variables for $a_1^0\pi^+$ Signal Monte Carlo, for $\cos\theta_{\rm T}$, ΔE, $N_{\rm trks}$, $m_{\rm ES}$, $\mathcal{F}$, m_{a_1}, m_ρ, m_{π_0}

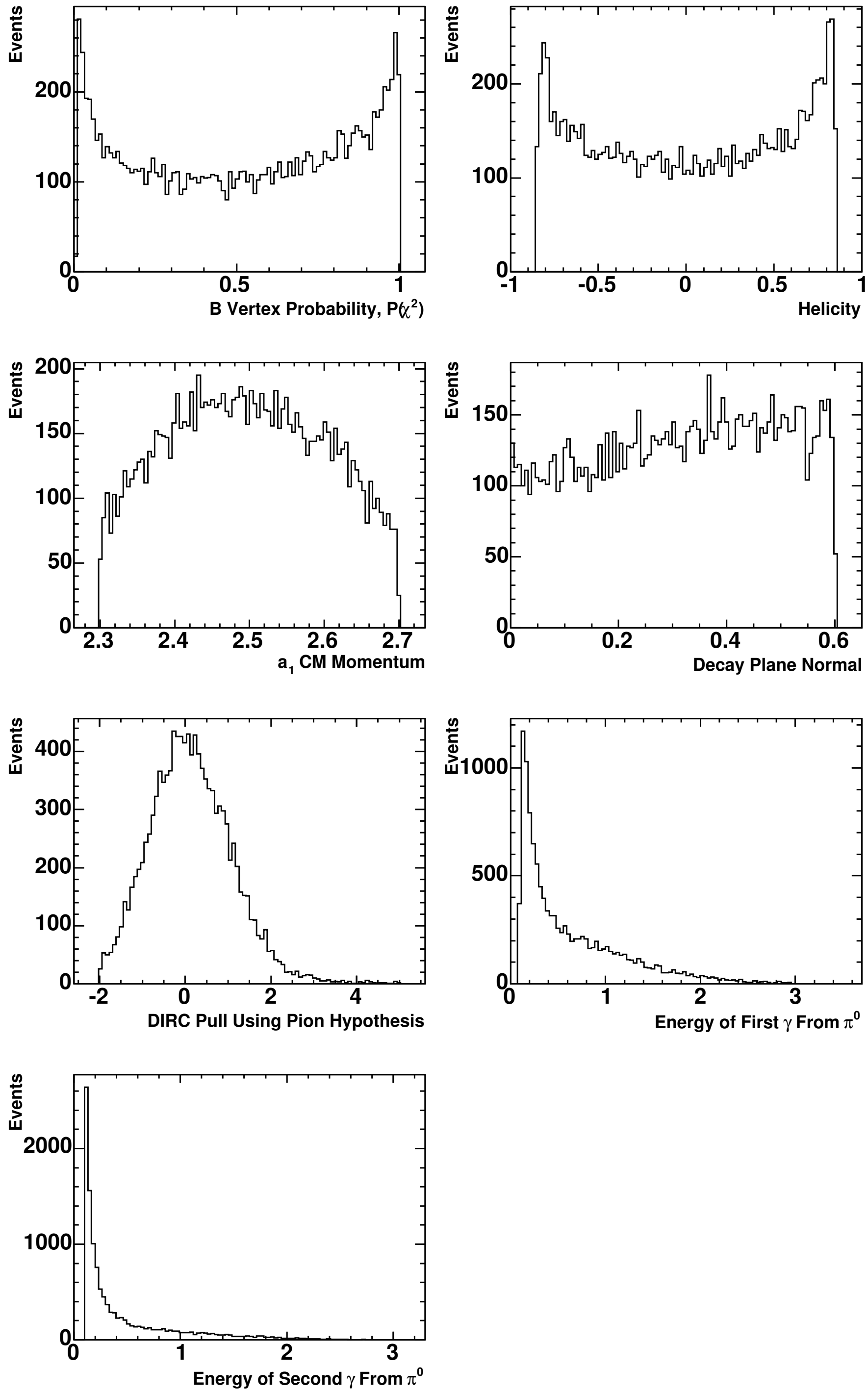

Figure 5.20: Cut Variables for $a_1^0\pi^+$ Signal Monte Carlo, for $p(\chi^2)$, $\mathcal{H}$, $p_{a_1}^{CM}$, $\mathcal{A}$, DIRC Pull (Pion Hypothesis) $E_{\gamma 1}$, $E_{\gamma 2}$

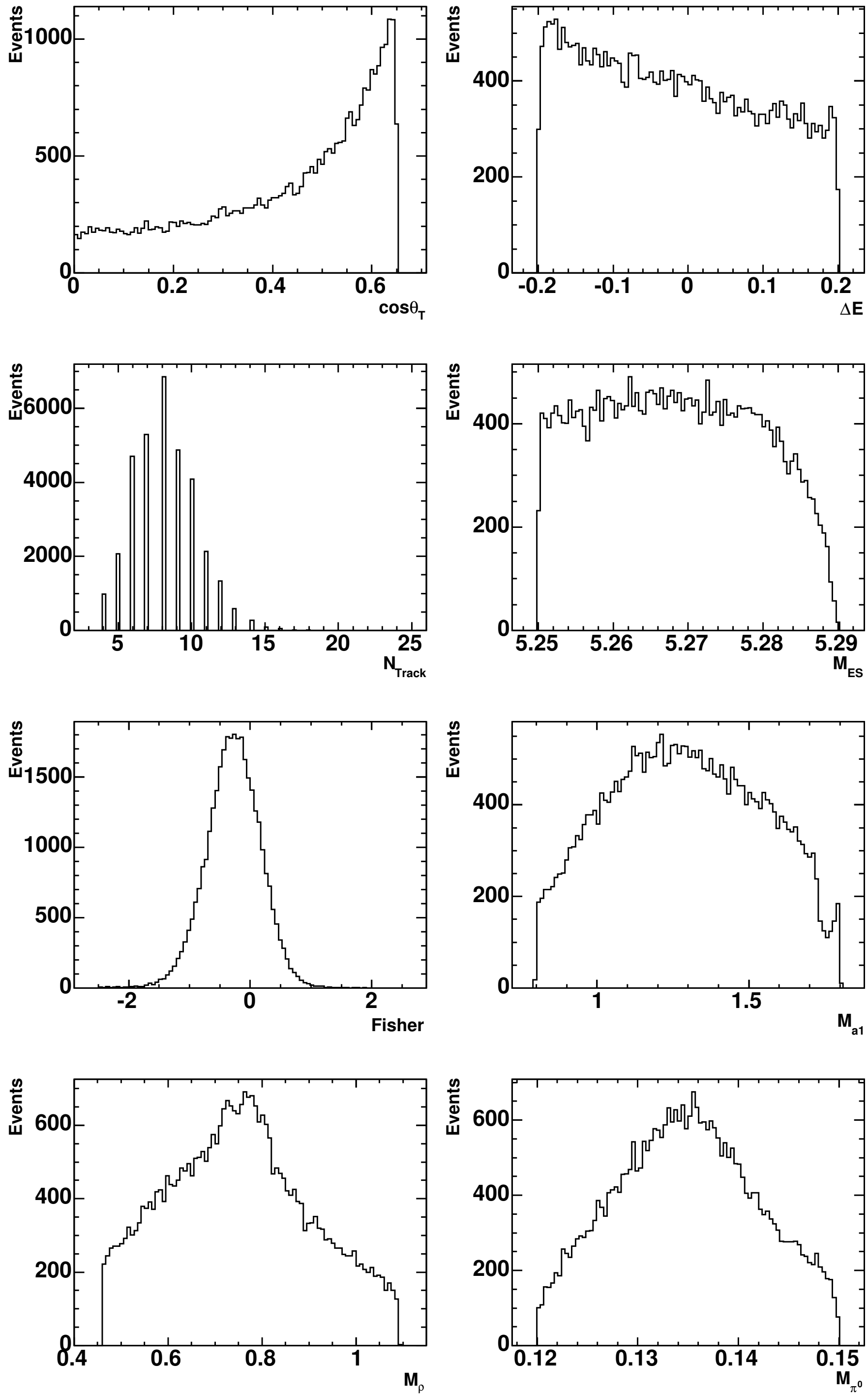

Figure 5.21: Cut Variables for $a_1^0\pi^+$ OnPeak Sidebands, for $\cos\theta_{\mathrm{T}}$, ΔE, N_{trks}, m_{ES}, $\mathcal{F}$, m_{a_1}, m_ρ, m_{π_0}

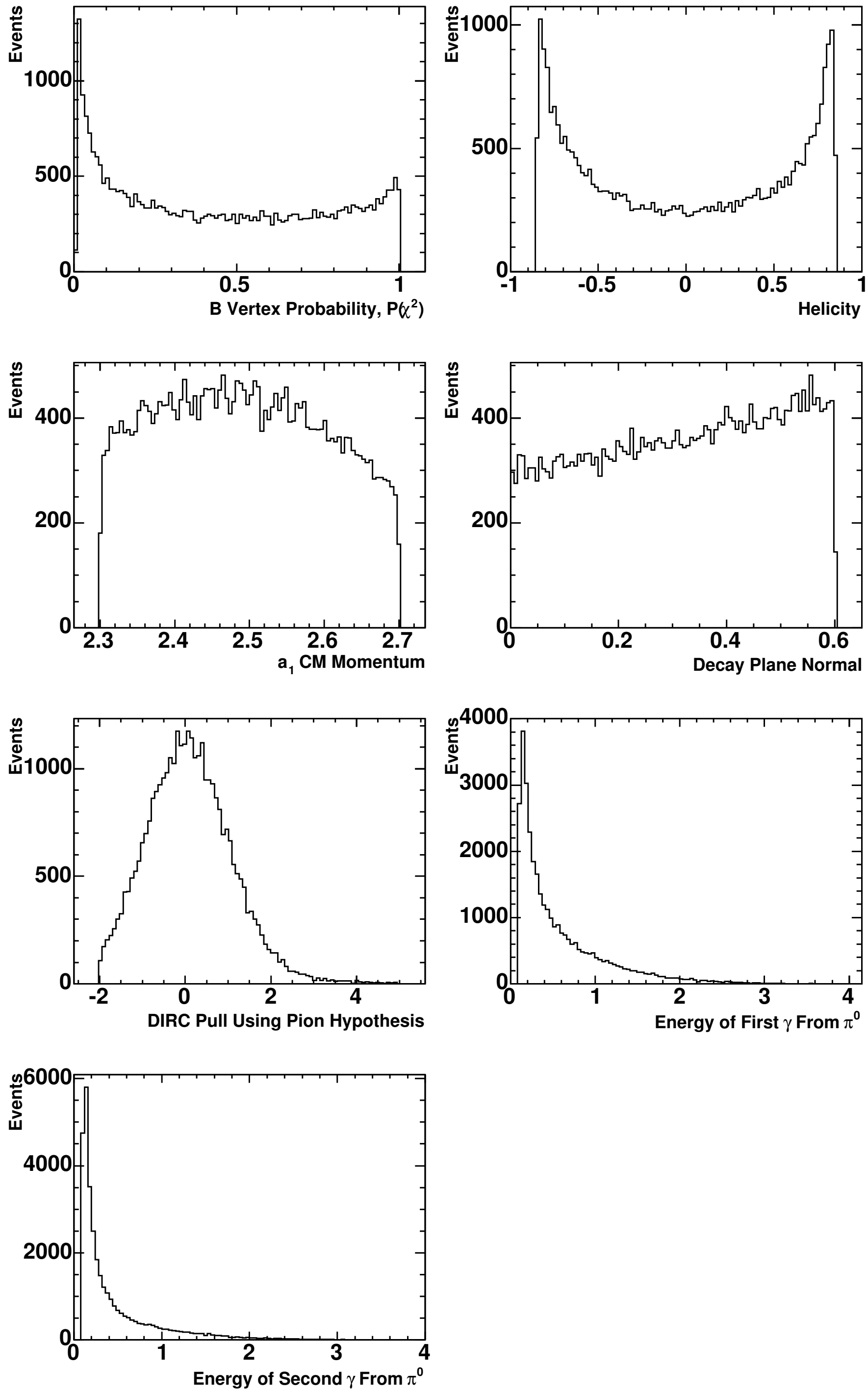

Figure 5.22: Cut Variables for $a_1^0\pi^+$ OnPeak Sidebands, for $p(\chi^2)$, $\mathcal{H}$, $p_{a_1}^{CM}$, $\mathcal{A}$, DIRC Pull (Pion Hypothesis) $E_{\gamma 1}$, $E_{\gamma 2}$

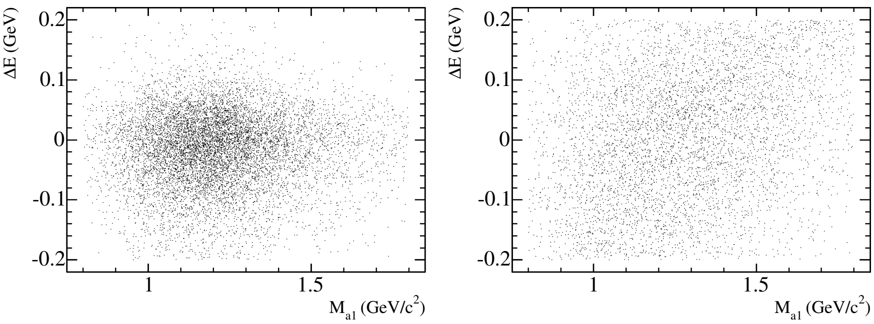

Figure 5.23: 2-dimensional scatter plots showing the correlations between the variables ΔE and M_{a_1} for $B^+ \to a_1^+ \pi^0$. The left plots shows truth matched MC and the right non-truth matched (SCF).

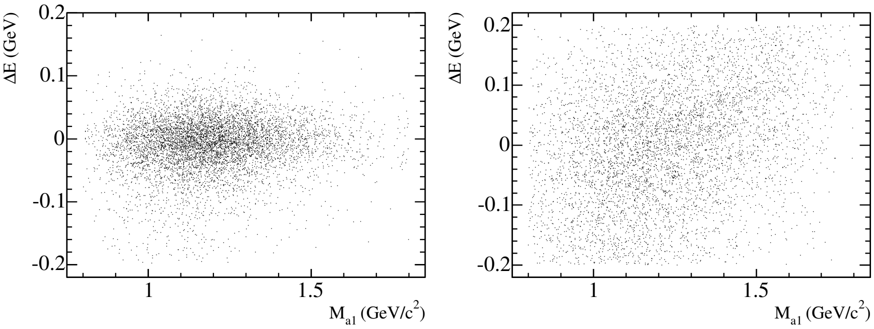

Figure 5.24: 2-dimensional scatter plots showing the correlations between the variables ΔE and M_{a_1} for $B^+ \to a_1^0 \pi^+$. The left plots shows truth matched MC and the right non-truth matched (SCF).

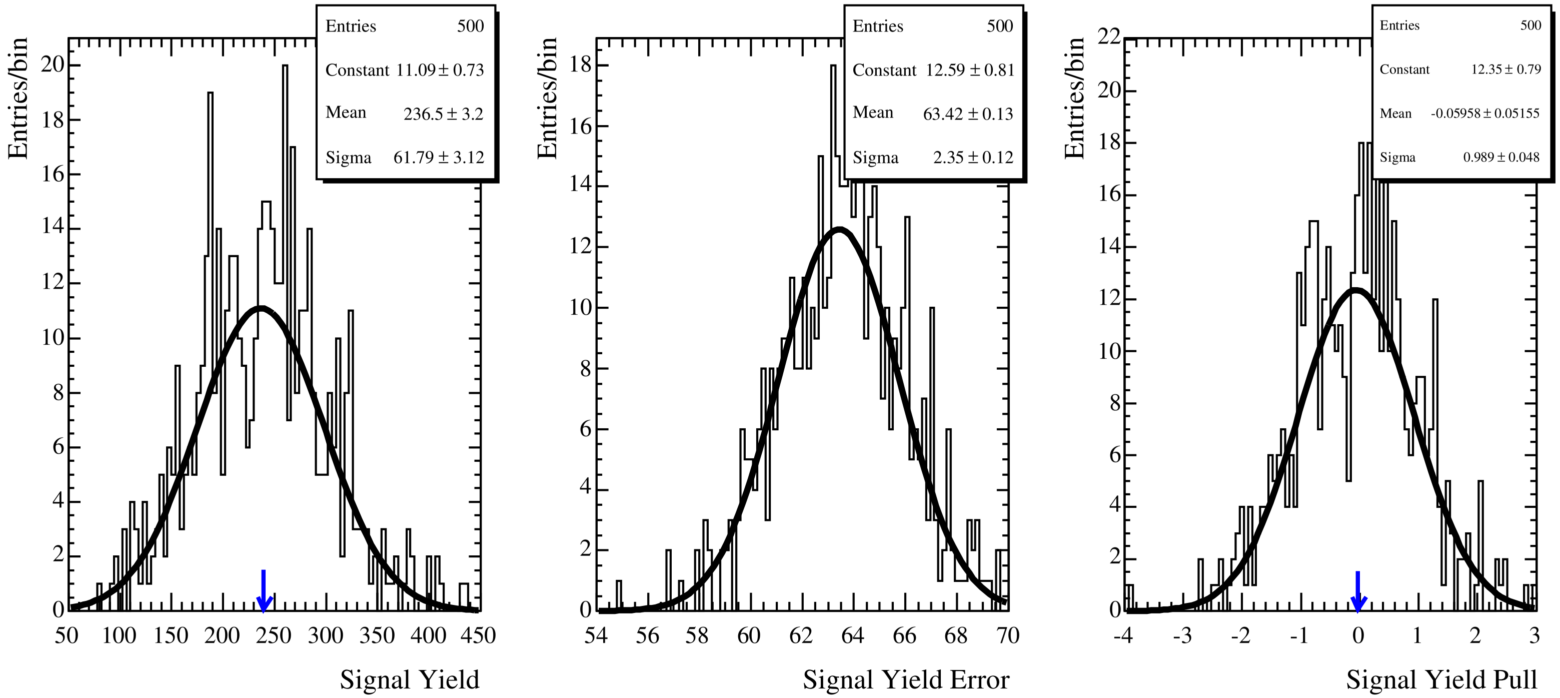

Figure 5.25: Fitted signal yield for $B^+ \to a_1^+ \pi^0$ where all components are determined by the PDFs. Number of signal, a_2, continuum and $B\overline{B}$ charm events were floated.

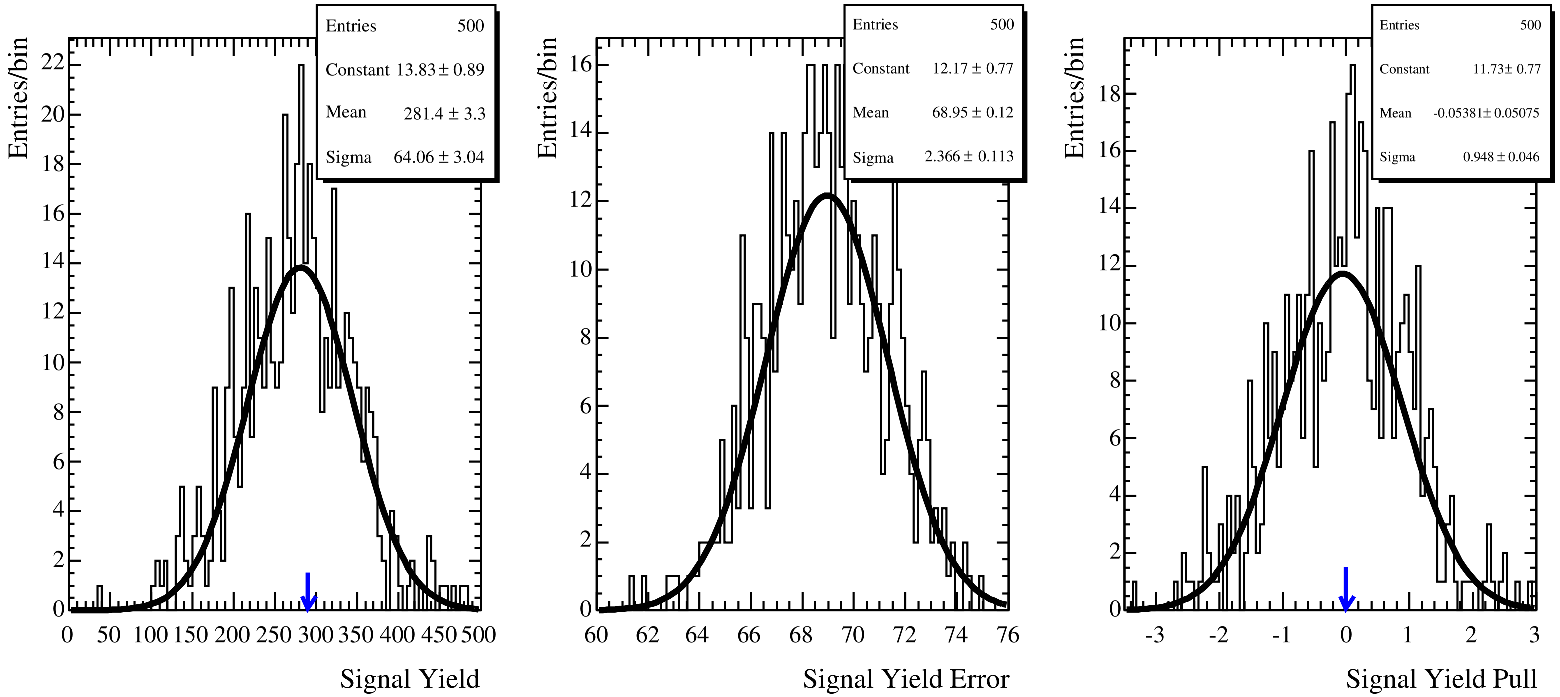

Figure 5.26: Fitted signal yield for $B^+ \to a_1^0 \pi^+$ where all components are determined by the PDFs. Number of signal, a_2, continuum and $B\overline{B}$ charm events were floated.

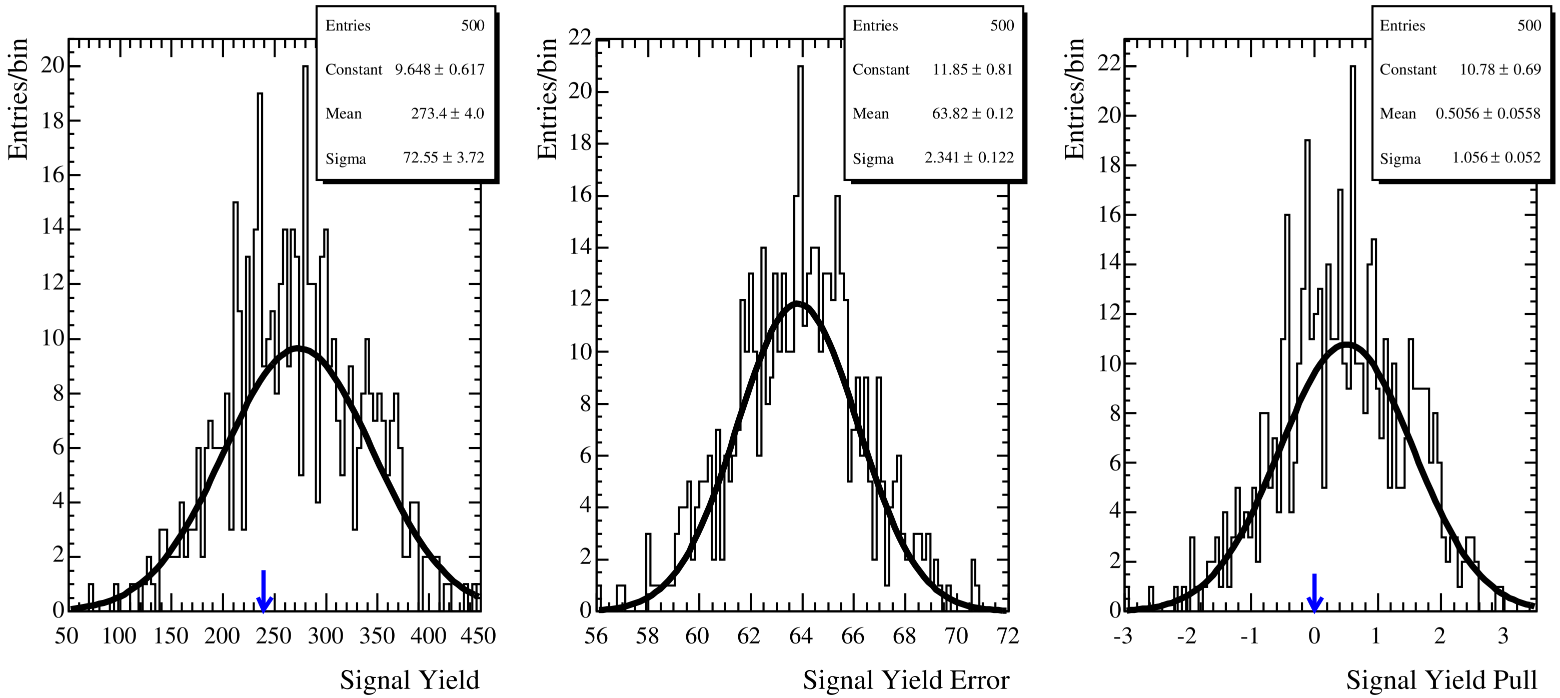

Figure 5.27: Fitted signal yield for $B^+ \to a_1^+\pi^0$ for Monte Carlo embedded signal events, continuum, a_2 and $B\overline{B}$ (both charm and charmless) generated from PDFs.

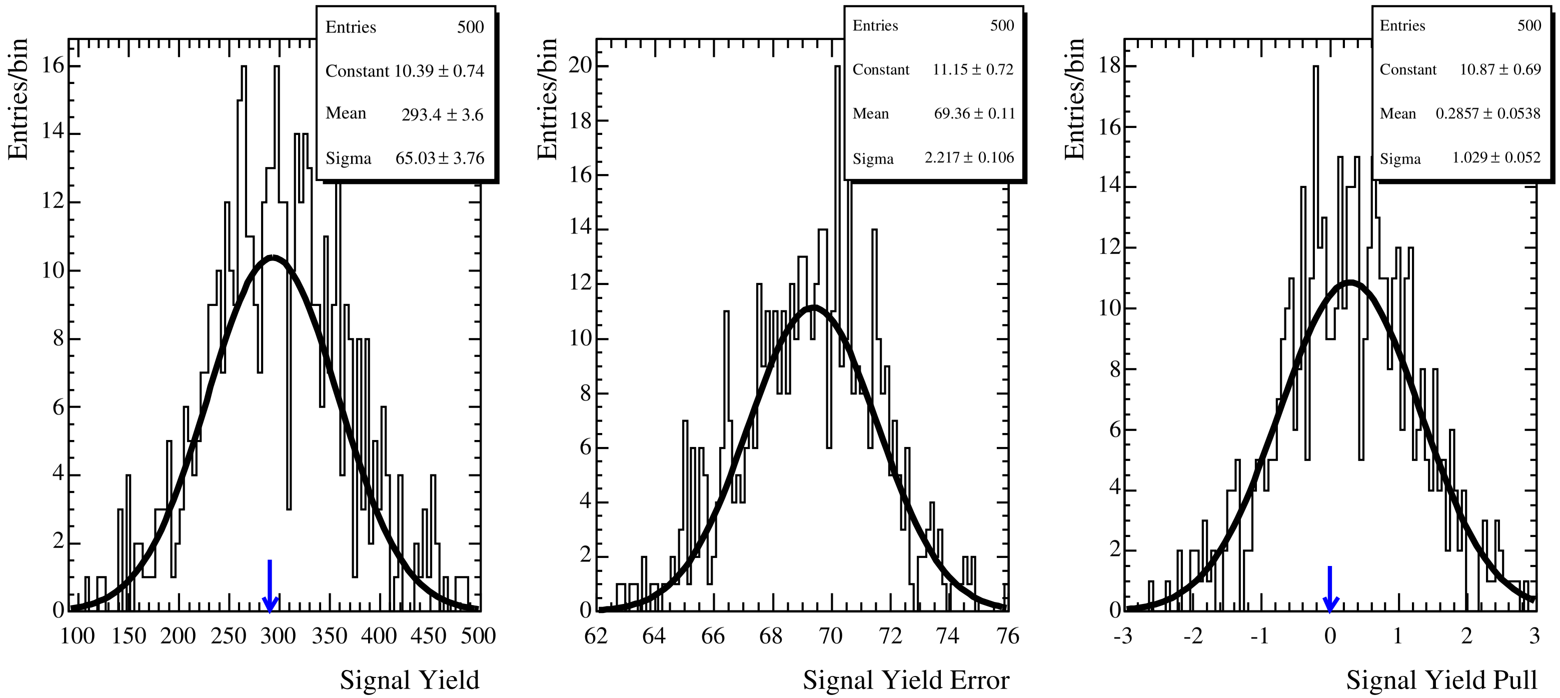

Figure 5.28: Fitted signal yield for $B^+ \to a_1^0\pi^+$ for Monte Carlo embedded signal events, continuum, a_2 and $B\overline{B}$ (both charm and charmless) generated from PDFs.

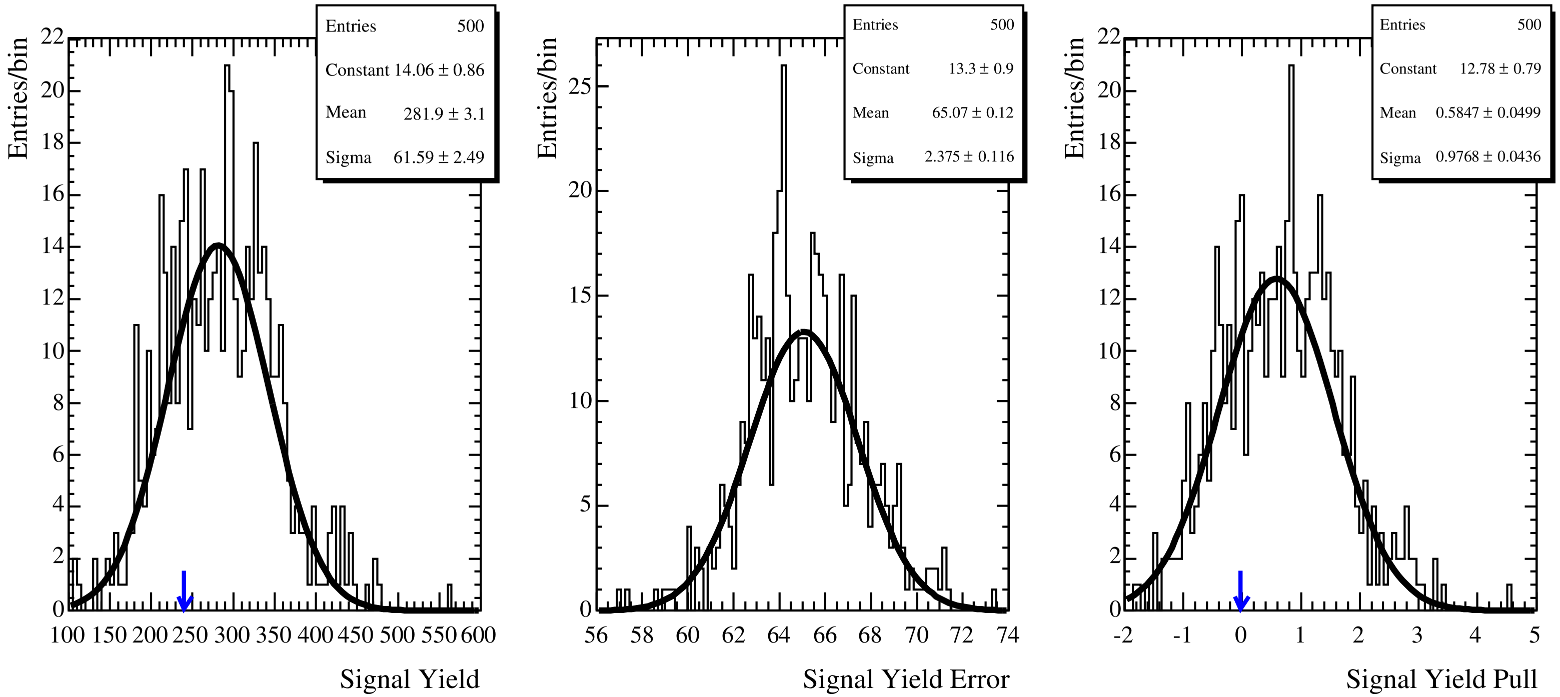

Figure 5.29: Fitted signal yield for $B^+ \to a_1^+ \pi^0$ for MC embedded signal events, a_2 and $B\overline{B}$ (both charm and charmless), with continuum embedded from PDFs.

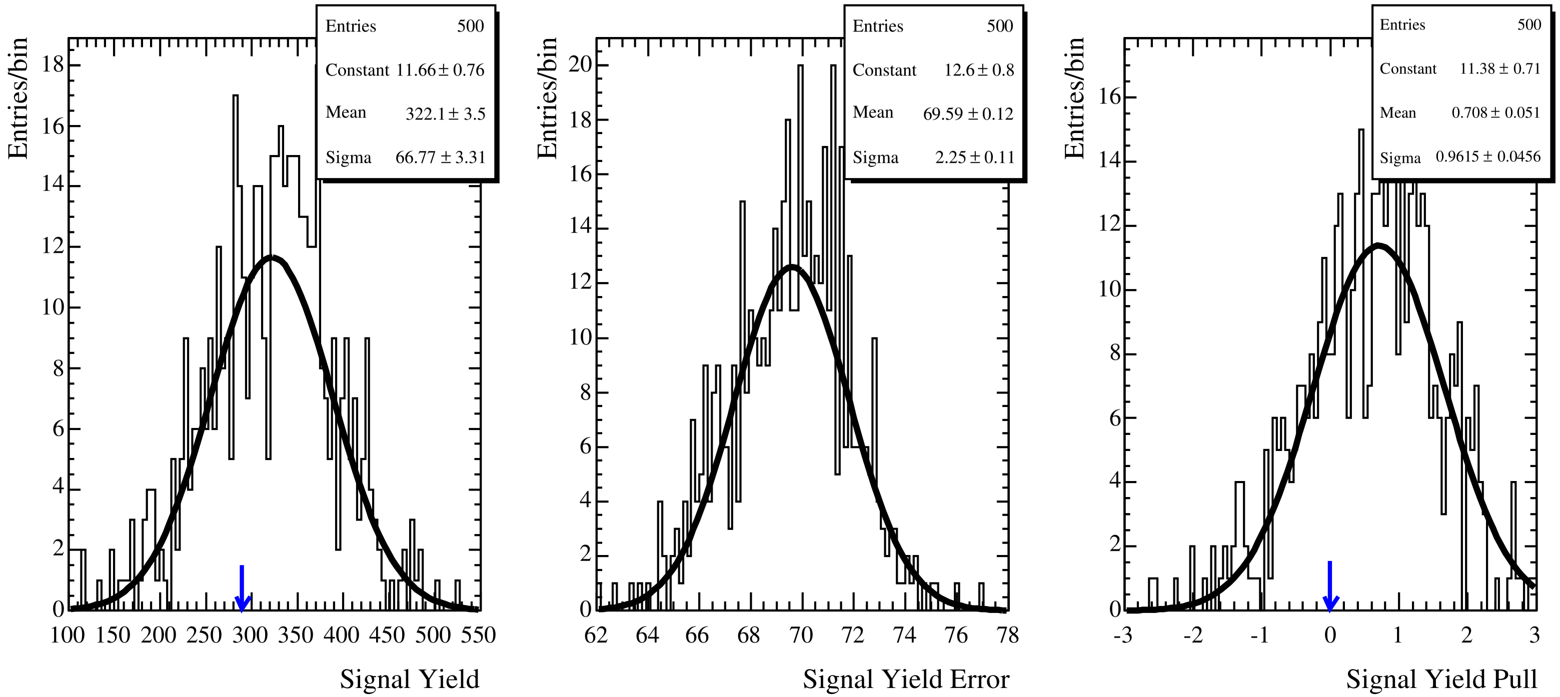

Figure 5.30: Fitted signal yield for $B^+ \to a_1^0 \pi^+$ for MC embedded signal events, a_2 and $B\overline{B}$ (both charm and charmless), with continuum embedded from PDFs.

Chapter 6

Results

6.1 Introduction

This chapter will show the branching fraction results from the maximum likelihood fits, and also a description of the systematic uncertainties on the results.

6.2 Branching Fraction Results

Table 6.1 shows the Maximum Likelihood fit results. The branching fraction for $B \to a_1\pi$ is given by:

$$\mathcal{B}(B \to a_1\pi) = \frac{N_{B \to a_1\pi}}{\epsilon_{corr} N_{B\bar{B}} \mathcal{B}(a_1 \to 3\pi)} \tag{6.1}$$

where $N_{B \to a_1\pi}$ is the measured number of signal events and ϵ_{corr} is the corrected signal MC efficiency.

The statistical significance is determined by using the difference in $-\ln(\mathcal{L})$ between the full fit and the case where the $B \to a_1\pi$ component is set to zero, as shown in Eq. (6.2)

$$\text{Significance} = \sqrt{-2\log(\mathcal{L}_{null}/\mathcal{L}_{max})} \tag{6.2}$$

The upper limit of the number of events N_{UL} is determined by numerical integration of the likelihood function, $L(N)$, as a function of fitted $B \to a_1\pi$ yield N where

$$\frac{\int_0^{N_{UL}} \mathcal{L}(N)dN}{\int_0^{\infty} \mathcal{L}(N)dN} = 0.9 \tag{6.3}$$

This gives the statistical 90% CL upper limit before systematic errors are included.

Table 6.1: Summary of ML Fit Results

ML fit quantity	$a_1^+\pi^0$	$a_1^0\pi^+$
#Data combs/ev.	1.20	1.56
#MC combs/ev.	1.29	1.83
Events to fit	24,608	33,375
Signal yield	$459.4^{+79.4}_{-77.2}$	$381.9^{+80.1}_{-77.1}$
Continuum yield	22811 ± 184	29348 ± 221
a_2 yield	28 ± 65	107 ± 65
$B\overline{B}$ charm yield	938 ± 99	2780 ± 147
ML-fit bias (/events)	77.0 ± 0.5	41.8 ± 0.4
MC ϵ (%)	13.08	7.53
Tracking corr. (%)	97.6	97.6
Neutrals corr. (%)	97.8	97.8
$\mathcal{B}_{dtr}$ (%)	50	100
$\mathcal{B}(\times 10^{-6})$	$26.4 \pm 5.4(stat) \pm 4.1(syst)$	$20.4 \pm 4.7(stat) \pm 3.3(syst)$
Upper Limits ($\times 10^{-6}$)	35.4	28.1
Stat. sign (σ)	4.2	3.8

6.2.1 Projection Plots

The signal component can be enhanced by making a cut on the probability ratio for the event to be signal. For each event, the ratio, $\mathcal{R}$ is defined to be

$$\mathcal{R} = \frac{n_{a_1\pi}\mathcal{P}_{a_1\pi}}{n_{a_1\pi}\mathcal{P}_{a_1\pi} + n_{a_2\pi}\mathcal{P}_{a_2\pi} + n_{cont}\mathcal{P}_{cont} + n_{B\bar{B}charm}\mathcal{P}_{B\bar{B}charm}} \tag{6.4}$$

Figures 6.1 and 6.2 show the projection plots with a cut of $\mathcal{R} < 0.9$ imposed.

6.2.2 ${}_s\mathcal{P}lots$

The ${}_s\mathcal{P}lots$ technique is described in detail in [63]. This method is used to create histograms showing only the signal distribution of the data for each of the five fit variables. This relies on the fact that the PDFs are sufficiently discriminating between the different species, and is valid since the toy MC tests show small pulls in the number of signal events.

The ${}_s\mathcal{P}lot$ technique makes use of the PDFs, the obtained yields, and also the correlation matrix obtained from the fit, in order to calculate a weight for each event. These weights are termed ${}_s\mathcal{W}eights$, and are properly normalised so that when they are summed over all of the events in the sample they give the measured signal yield. One can also obtain an ${}_s\mathcal{W}eight$ for a particular species in the fit, and it is found that for each event, these species ${}_s\mathcal{W}eights$ sum to unity. ${}_s\mathcal{P}lots$ are shown in figures 6.3 to 6.6 for the fit variables.

6.2.3 Log Likelihood Ratio Plots

A useful plot to use as a cross check shows the distribution of the likelihood ratio. Signal is expected to have a value close to unity, where background has a value closer to 0. Figure 6.7 and Figure 6.8 show Log Likelihood Ratio plots for both $B^+ \to a_1^+\pi^0$ and $B^+ \to a_1^0\pi^+$.

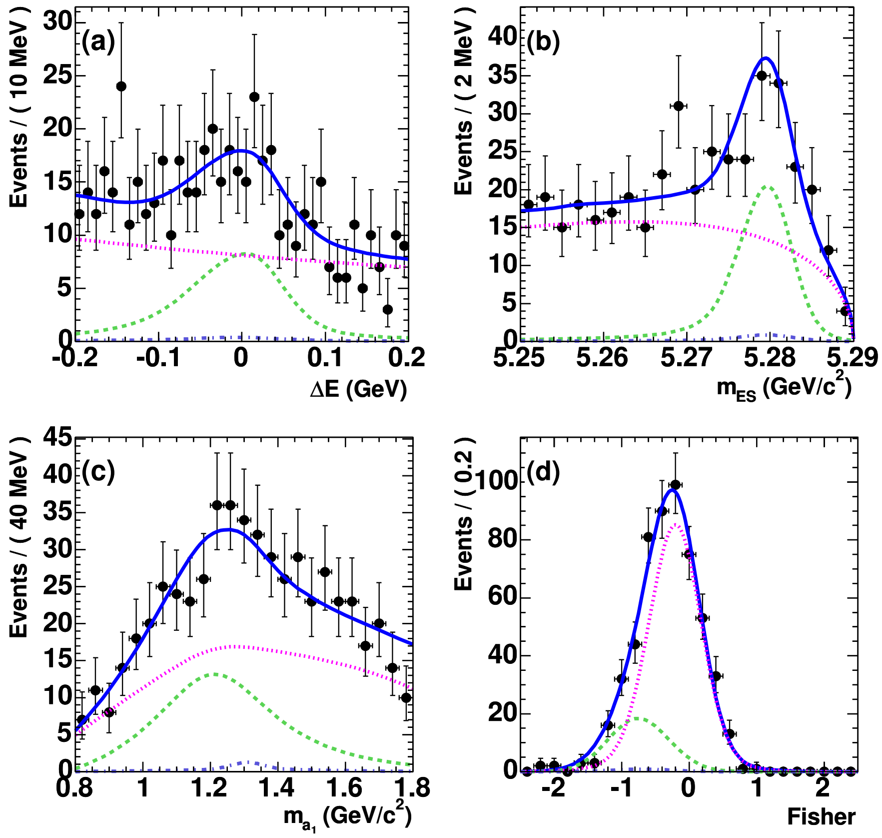

Figure 6.1: Projections of a) ΔE, b) $m_{\rm ES}$, c) m_{a_1}, and d) $\mathcal{F}$ for $B^{\pm} \to a_1^{\pm}\pi^0$. Points represent on-resonance data, green dashed lines the signal, pink dotted lines the continuum, blue dashed-dotted lines the a_2 background, and solid lines the full fit function. These plots are made with a requirement on the signal likelihood to enhance the signal, and thus do not show all events in the data sample.

6.3 Systematic Uncertainties

The systematic errors are summarized in Table 6.2. Some of the systematic errors on the signal yield that arise from uncertainties in the values of the PDF parameters have already been incorporated into the overall statistical error, since they are floated in the fit. The sensitivity to the other parameters of the signal and background PDF components are determined

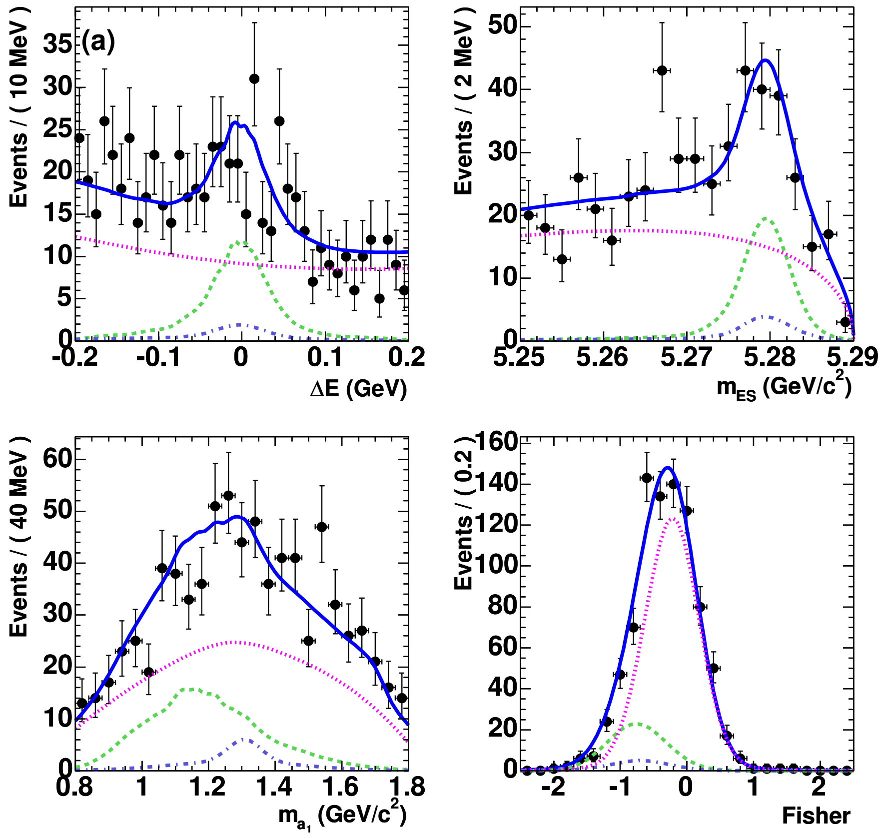

Figure 6.2: Projections of a) ΔE, b) m_{ES}, c) m_{a_1}, and d) $\mathcal{F}$ for $B^{\pm} \to a_1^0 \pi^{\pm}$. Points represent on-resonance data, green dashed lines the signal, pink dotted lines the continuum, blue dashed-dotted lines the a_2 background, and solid lines the full fit function. These plots are made with a requirement on the signal likelihood to enhance the signal, and thus do not show all events in the data sample.

by varying these within their uncertainties. For example, the effect of varying the mass and width of the a_1 is included in the PDF parameters variation systematic.

The fit bias correction as described in 5.7.4 has an error associated with it The error is taken as half of the fit bias correction.

As described in section 2.6.3, there is a possible effect from the interference between the a_2 resonance and the a_1. As this analysis has been treated in the quasi two-body

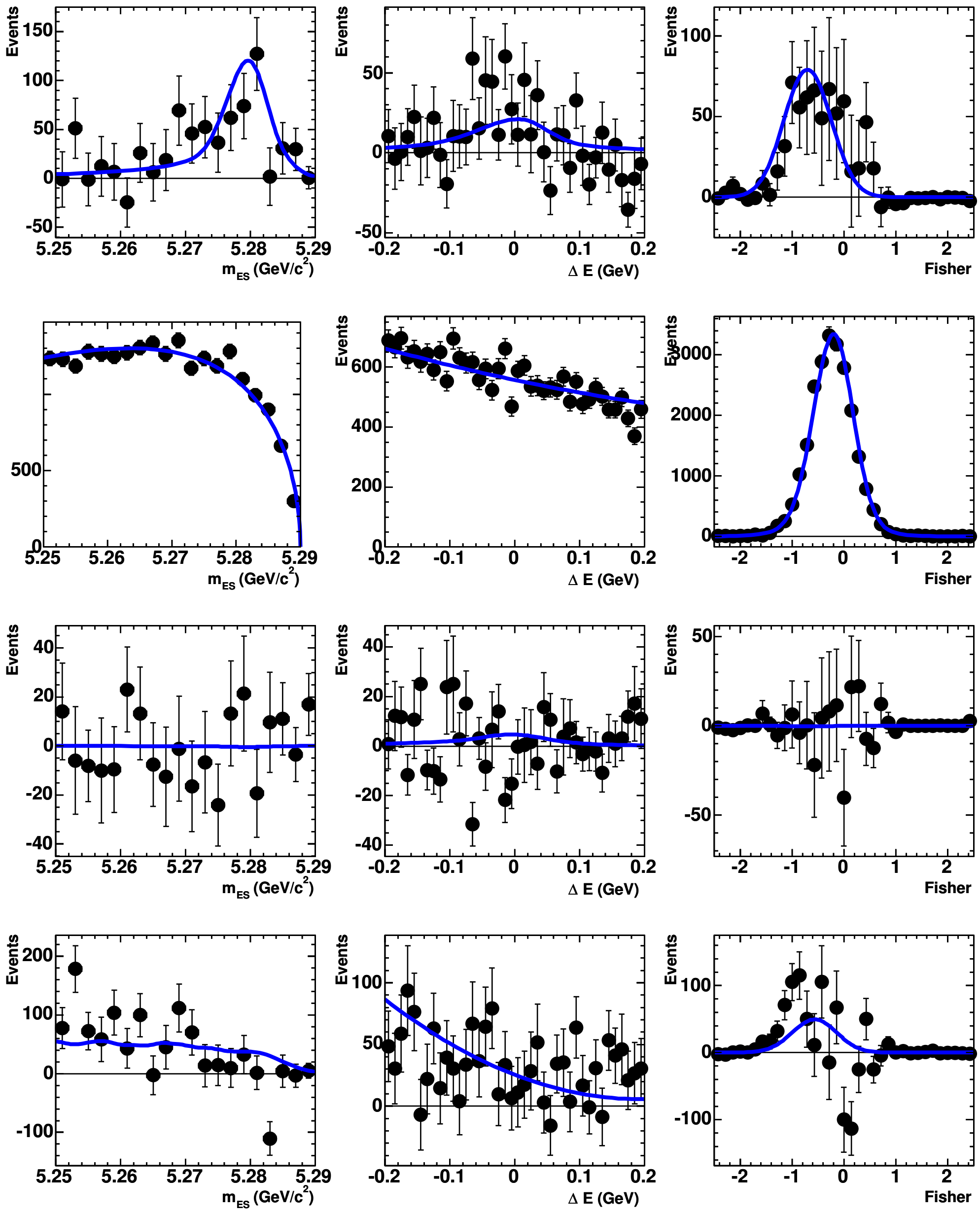

Figure 6.3: ${}_s\mathcal{P}lots$ for $B^{\pm} \to a_1^{\pm}\pi^0$. Fit components are signal (top row), continuum (second row), a_2 (third row), $B\overline{B}$ Charm (fourth row).

approximation, then a reasonable way of taking this into account is by assigning a systematic. The systematic can be estimated by investigating the approximate effect on the branching

Table 6.2: Summary of systematic errors for the $a_1^{\pm}\pi^0$ and $a_1^0\pi^{\pm}$ branching fraction measurements.

Systematic	$a_1^+\pi^0$	$a_1^0\pi^+$
PDF Parameter Variation	8.6%	8.8%
Fit Bias	8.4%	5.5%
$a_1 - a_2$ Interference	6.6%	7.4%
SCF Variation	4.4%	8.2%
Tracking Efficiency	3.9%	3.9%
π^0 Efficiency	3.0%	3.0%
P-wave and S-wave Reconstruction	1.6%	-
Charmless $B\overline{B}$ Background	1.4%	3.1%
Number of $B\overline{B}$ Pairs	1.1%	1.1%
$\cos\theta_T$	1.1%	1.8%
Track Multiplicity	1.0%	1.0%
$\rho\pi\pi$, 4π Cross-Feed	0.9%	0.5%
a_1K Cross-Feed	-	0.4%
Total	16%	16%

ratio of the interference. The a_2 and a_1 amplitudes were added together with a varying phase difference to determine the maximum change in the yield. Half of the maximum change in yield was used as an uncertainty.

The determination of the fraction of SCF relies on the truth matching available in the MC simulation, which isn't exact. Some error must be assigned for this effect, even though it is difficult to determine exactly how the fraction may be inaccurate. The uncertainty in SCF is investigated by varying the SCF fraction by an arbitrary $\pm 10\%$, so this gives some idea of the effect, and the variation is consistent with the previous *BABAR* a_1 analysis [5].

Another possible source of interference is from the σ interfering with the ρ. The a_1 decay has, like the B decay been treated in a two-body approximation, and so interferences have been neglected. MC simulating the $a_1 \to \sigma\pi$ decay was reconstructed to determine the selection efficiency. The difference between this and the reconstruction efficiency of the a_1

signal Monte Carlo was used as the systematic error. This is 1.6% for both modes.

Another error arises from fixing the charmless $B\overline{B}$ background yields in the final fit, and originates from the uncertainties in the branching ratios used to estimate the numbers of events expected in the final data sample. The variation in the number of charmless $B\overline{B}$ events expected in the data sample was calculated, and from this the PDF shapes could be varied. By redoing the fit with the altered shapes, the overall effect on the branching ratio was determined.

There are a number of smaller systematic errors: The total number of $B\overline{B}$ pairs, which is measured by B counting as described in section 4.4 has an intrinsic error. The selection criteria for event shape cuts also introduces a further error, the largest of these being due to the cut on $\cos\theta_T$. The assumption made is that for signal MC this variable has a flat distribution, and so an error can be assigned by looking at the actual efficiency of this cut and calculating the difference between this and the expected efficiency, which is 65% for a flat distribution.

The track multiplicity is related to the cut on the minimum number of tracks in the event, which requires at least one other track from the other B. The signal MC inefficiency for this is a few percent, and so a systematic error of 1% is assigned for this.

There are potential backgrounds from $\rho\pi\pi$ and 4π, which haven't been included in the fit model. As their branching fractions are not well known, a systematic error is sufficient to take these into account. By reconstructing MC events of these decays, the reconstruction efficiency can be determined, and an error is calculated from the difference between this and the a_1 signal reconstruction efficiency. Also considered is the possibility of misreconstruction of $a_1 K$ decays, and these are considered in a similar manner, assigning a systematic error by determining the reconstruction efficiency, and this again is a small error.

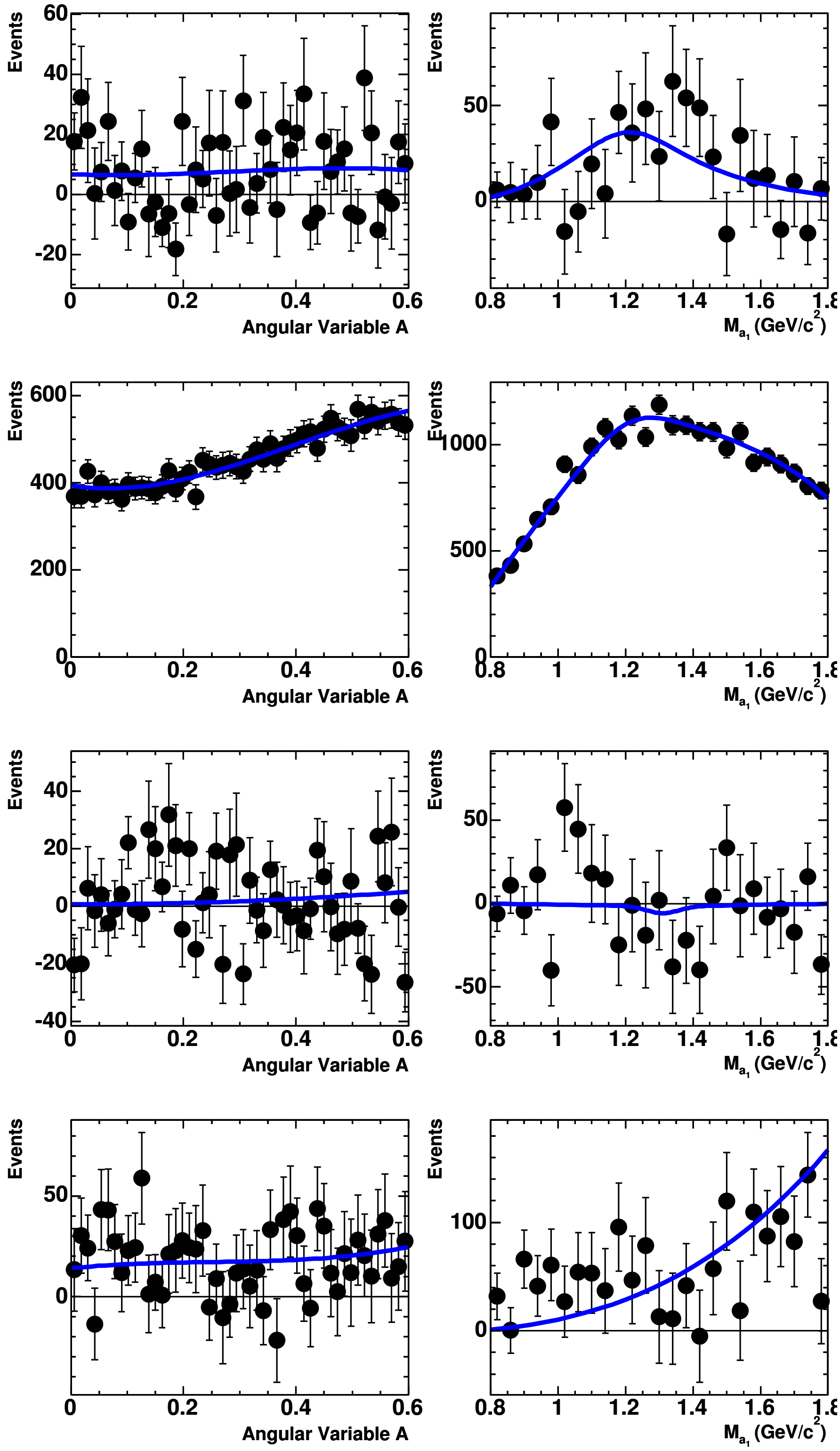

Figure 6.4: ${}_s\mathcal{P}lots$ for $B^{\pm} \rightarrow a_1^{\pm}\pi^0$. Fit components are signal (top row), continuum (second row), a_2 (third row), $B\overline{B}$ Charm (fourth row).

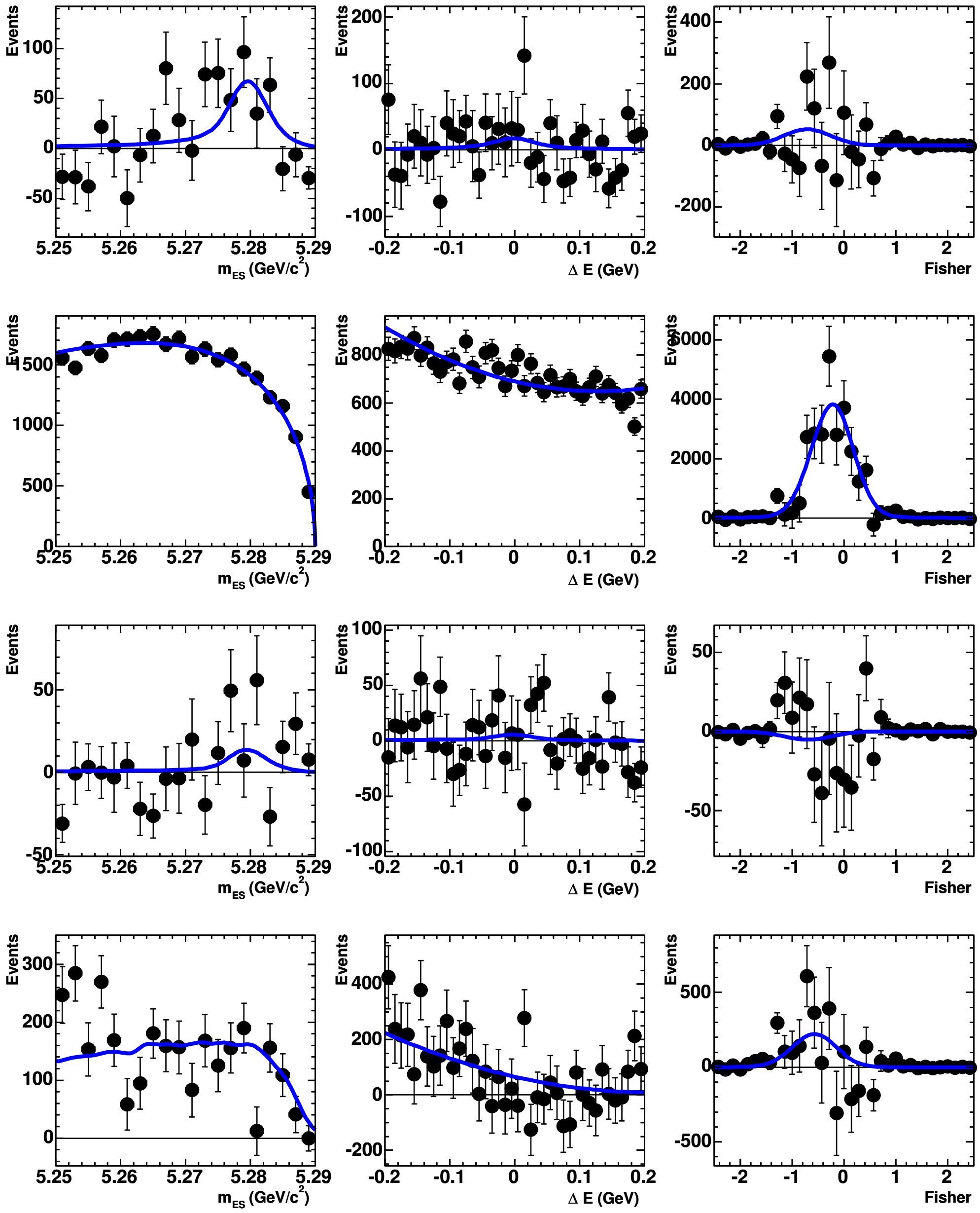

Figure 6.5: ${}_s\mathcal{P}lots$ for $B^{\pm} \to a_1^0\pi^{\pm}$. Fit components are signal (top row), continuum (second row), a_2 (third row), $B\overline{B}$ Charm (fourth row).

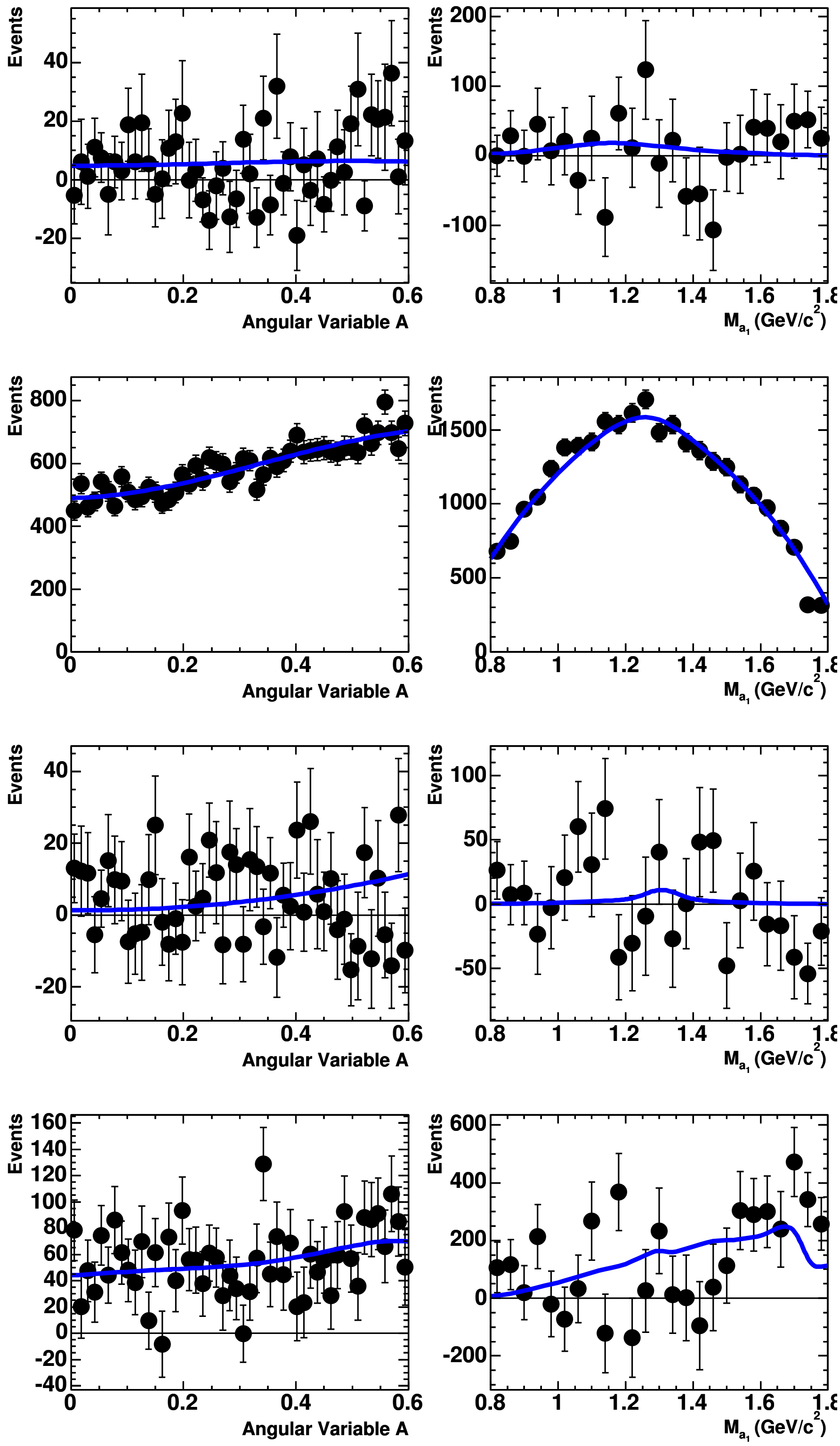

Figure 6.6: ${}_s\mathcal{P}lots$ for $B^{\pm} \to a_1^0 \pi^{\pm}$. Fit components are signal (top row), continuum (second row), a_2 (third row), $B\overline{B}$ Charm (fourth row).

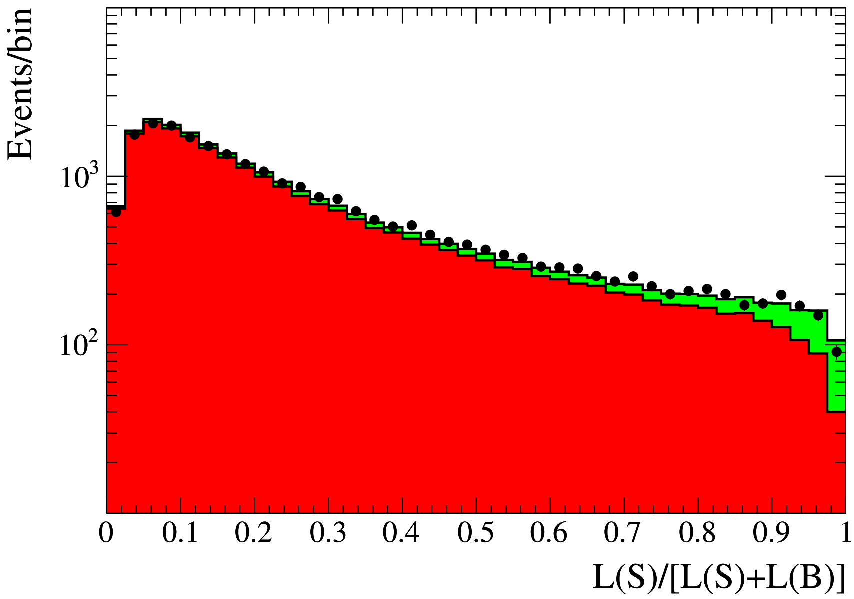

Figure 6.7: Log Likelihood Ratio Plots distribution for $B^+ \to a_1^+ \pi^0$. Points represent the data, the solid histogram is from MC samples of signal and background, with the background component in red.

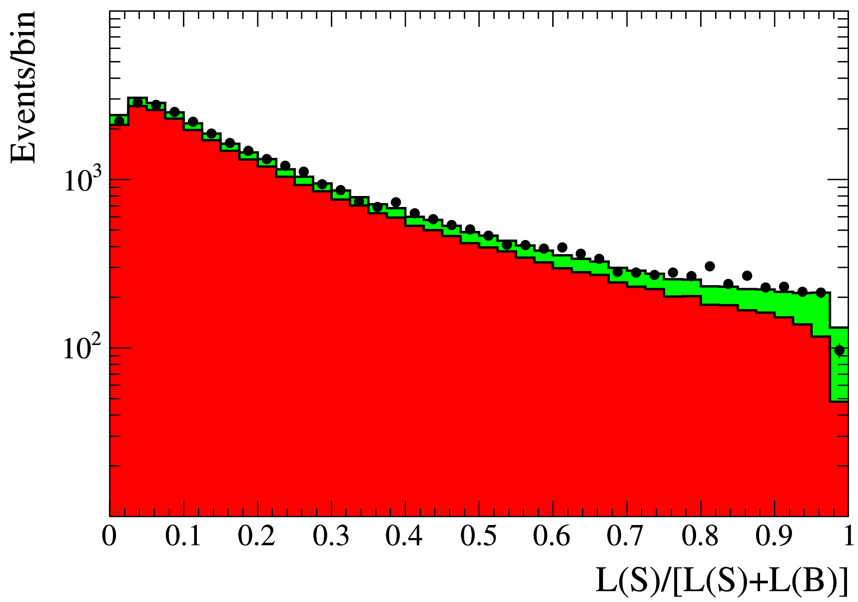

Figure 6.8: Log Likelihood Ratio Plots distribution for $B^+ \to a_1^0\pi^+$. Points represent the data, the solid histogram is from MC samples of signal and background, with the background component in red.

Chapter 7

Discussion & Conclusions

7.1 Introduction

This chapter will summarise the results of the maximum likelihood analysis and compare with previous results and theoretical predictions. Expectations and suggestions for future improvements are also discussed.

7.2 Summary and Significance of Results

This measurement constitutes first evidence for the charged B-meson decay to $a_1\pi$. The main results are shown in Table 7.1.

Table 7.1: Summary of results.

	$a_1^+\pi^0$	$a_1^0\pi^+$
$\mathcal{B}(\times 10^{-6})$	$26.4 \pm 5.4(stat) \pm 4.1(syst)$	$20.4 \pm 4.7(stat) \pm 3.3(syst)$
90% CL UL ($\times 10^{-6}$)	35.4	28.1
Stat. sign (σ)	4.2	3.8

This agrees well with the prediction of $33.2 \pm 3.8 \pm 3.0$ for $B^0 \to a_1^{\pm}\pi^{\mp}$made in the framework of naive factorisation made by Bauer, Stech and Wirbel [7]. The branching fraction for $B^{\pm} \to (a_1\pi)^{\pm}$ is expected to be half of this, which is $(16.6 \pm 1.9 \pm 1.5) \times 10^{-6}$. This agrees with the results of this analysis.

The results agree less with the prediction made by Laporta [8], also within the framework of naive factorization. The predicted branching fractions here are $(5 - 11) \times 10^{-6}$ and $(4-9) \times 10^{-6}$ for $B^+ \to a_1^+\pi^0$ and $B^+ \to a_1^0\pi^+$, respectively. The predictions are given for different mixing angles, and the values shown here represent the range considered of 32° to 58°.

$B^+ \to (a_1\pi)^+$ is a possible background in the analysis of $B^0 \to (\rho\pi)^0$, which measures the angle α [64]. As this analysis was carried out before this one was finished, an estimated branching fraction for $B^+ \to (a_1\pi)^+$ of 20.0 ± 15.0 had to be used. This estimate is consistent with the results shown here.

7.3 Future Enhancements

The luminosity of data taken by *BABAR* has been increasing since this analysis was performed. This analysis was performed on $210.5\,\text{fb}^{-1}$ of data, whereas the full dataset now stands at around $500\,\text{fb}^{-1}$, and the final dataset is estimated to be around $700\,\text{fb}^{-1}$. This means that the statistical error on the branching fraction will reduce by a factor $\approx \sqrt{3}$, and the significance will increase by a factor of $\approx \sqrt{3}$. Hence the error on the branching fraction will reduce to around ± 1.5, and the significance will increase to around 7. This would mean that an unequivocal observation would be likely to be made using the full dataset.

One possible area of improvement is the reduction in the systematics during further iterations of this analysis. As the luminosity increases, many of these will naturally reduce. Here is a summary of how the main ones are expected to vary:

- The errors on the PDF parameters will reduce as the luminosity increases, due to the increased data sample, and hence the reduction of the statistical error. These will reduce by $\approx \sqrt{3}$, and hence the new errors would be expected to be 5.0% and 5.1%.

- The fit bias error was estimated at 8.4% and 5.5% for the two modes. As the luminosity increases, this error is expected to reduce by a factor of $\approx \sqrt{3}$, so this will mean the new errors are likely to be around 4.8% and 3.2% for the two modes.

- The interference from the a_2 was estimated by looking at overlapping resonances, and finding its possible maximum effect. It is not expected that this phenomenon is dependent on the luminosity, and so an estimate of the new errors would be unchanged. It may be possible to measure the a_2 yield in the fit, compared with the current analysis which gave values consistent with zero. The errors should remain at 6.6% and 7.4% for the two modes.

- The error from P-wave and S-wave reconstruction, referring to the interference of the σ resonance with the ρ is not expected to depend on luminosity. The error was determined by looking at exclusive Monte Carlo, that decays just to $B^+ \to a_1\pi, a_1 \to \sigma\pi$, and determining the difference in reconstruction efficiency between this sample and the a_1 signal MC. With higher statistics, this effect and hence error might be better estimated, but is not expected to significantly reduce. The errors should remain at 1.6%, and is not relevant for the $B^+ \to a_1^0\pi^+$ mode.

- The fraction of SCF was obtained using the Monte Carlo, which isn't exact, hence a systematic error was applied, found by varying the fraction by an arbitrary value of 10%. It is thought that this effect isn't a function of luminosity, so the error will remain unchanged at 4.4% and 8.2% for the two modes.

- The error on the tracking efficiency is determined from studies that shouldn't vary much with the luminosity. So, these errors should remain at 3.9% for both modes.

- There are several smaller errors, for example the charmless $B\overline{B}$ backgrounds that are included in the fit model but fixed and so introduce a possible error; and the $\rho\pi\pi, 4\pi$, which aren't included in the fit and so need an error to account for them. The total of these errors would be expected to remain roughly the same for higher luminosities, so around 2.5% and 3.9%.

In total, if the integrated luminosity was to increase by a factor of 3, compared with the amount of data used in this analysis, then the total systematic error would be expected to reduce to 11.5% and 14.4%. The statistical errors would be expected to be reduced by a factor of $\sqrt{3}$, giving 3.1×10^{-6} for $B^+ \to a_1^+ \pi^0$, and 2.7×10^{-6} for $B^+ \to a_1^0 \pi^+$. Assuming the same central values for the branching fractions, then the expected results are:

$$
\begin{aligned}
\mathcal{B}_{B^+ \to a_1^+ \pi^0} &= (26.4 \pm 3.1 \pm 3.0) \times 10^{-6} \qquad (7.1)\\
\mathcal{B}_{B^+ \to a_1^0 \pi^+} &= (20.4 \pm 2.7 \pm 2.9) \times 10^{-6}
\end{aligned}
$$

The significances are expected to be 7.2σ and 6.6σ. With these reduced errors, the results are still consistent with the theory prediction from Laporta.

As a future improvement it may be possible to fit to the a_1 mass, M and width, Γ. The current analysis fixed these at the values obtained by the previous *BABAR* analysis of $B^0 \to a_1^{\pm} \pi^{\mp}$, as the fit couldn't handle the extra degrees of freedom. Further investigation would have to be carried out to determine how the fit could handle these two extra variables.

Having made a successful measurement of $B^+ \to (a_1\pi)^+$ and with larger luminosities providing the expectation of a more accurate result, possibly more in line with theory, then one could attempt to measure the other a_1 modes. In particular, the modes with final state $3\pi^0$ or $4\pi^0$ are thought to be harder in terms of reconstruction. There will no doubt be larger numbers of misreconstructed photons that will cause higher levels of background, and these must be dealt with. The a_1 decay with final state of 3π might be a significant background to the $B^+ \to \rho^+\rho^0$ decay.

Also worth pursuing would be the measurement of $B^+ \to a_1^0 K^+$. The only change is effectively swapping the charged pion track for a kaon, even the efficiency should stay the same. In addition it would be possible to measure $a_1\pi$ and $a_1 K^+$ together, using the DIRC pull to distinguish them.

As for measuring the a_2, the current analysis included this in the fit model, and floated the yield. The yields obtained are 28 ± 65 and 107 ± 65, so it is not possible to say the a_2 has been observed here. The errors here include just the statistical ones. With larger statistics, it still may not be possible to measure this branching fraction, there is no reliable prediction for the a_2 at present. As discussed in sections Section 2.6.2 and 5.3, there is a total of three angles that can be used to parameterise the a_1 decay, whereas only one of these was used in the fit model for this analysis. This was the decay plane normal angle, and it is possible that including another angle may yield further improvements.

Bibliography

[1] Gustavo Burdman. New solutions to the hierarchy problem. *Braz. J. Phys.*, 37:506–513, 2007.

[2] A. D. Sakharov. Violation of CP invariance, C asymmetry, and baryon asymmetry of the Universe. *Pisma Zh. Eksp. Teor. Fiz.*, 5:32–35, 1967.

[3] http://www-public.slac.stanford.edu/babar/.

[4] http://www.slac.stanford.edu/.

[5] B. Aubert et al. Observation of b0 meson decay to a1(1260)+- pi-+. *Phys. Rev. Lett.*, 97:051802, 2006.

[6] M. Gronau and J. Zupan. Weak phase alpha from $B^0 \to a_1(1260) \pm \pi \mp$. *Phys. Rev.*, D73:057502, 2006.

[7] B. Aubert et al. Exclusive non-leptonic decays of D-,D_s- and B-mesons. *Z. Phys. C*, 34:103, 1987.

[8] V. Laporta, G. Nardulli, and T. N. Pham. Non leptonic B decays to axial-vector mesons and factorization. *Phys. Rev.*, D74:054035, 2006.

[9] T. D. Lee and C. N. Yang. Question of parity conservation in weak interactions. *Phys. Rev.*, 104:254–258, 1956.

[10] C. S. Wu et al. Experimental test of parity conservation in β decay. *Phys. Rev.*, 105:1413–1414, 1957.

[11] B. L. Ioffe et al. *Sov. Phys. JETP*, 5:327, 1957.

[12] J. H. Christenson et al. Evidence for the 2π decay of the K_2^0 meson. *Phys. Rev. Lett.*, 13:138–140, 1964.

[13] K. Hagiwara et al. Review of particle physics. *Phys. Rev.*, D66:010001, 2002.

[14] M. Kobayashi and T. Maskawa. CP violation in the renormalizable theory of weak interaction. *Prog. Theor. Phys.*, 49:652–657, 1973.

[15] L. M. Lederman. The discovery of the upsilon, bottom quark, and B mesons. Given at 3rd International Symposium on the History of Particle Physics: The Rise of the Standard Model, Stanfor d, CA, 24-27 Jun 1992.

[16] M. L. Perl. Review of heavy lepton production in e^+e^- annihilation. Invited talk presented at International Symposium on Lepton and Photon Interactions at High Energies, Hamburg, Aug 25-31, 1977.

[17] Cabibbo, Nicola. Unitary Symmetry and Leptonic Decays. *Phys. Rev. Lett.*, 10(12):531–533, Jun 1963.

[18] W.-M. Yao et al. Review of Particle Physics. *Journal of Physics G*, 33:1+, 2006.

[19] L. Wolfenstein. Parametrization of the Kobayashi-Maskawa matrix. *Phys. Rev. Lett.*, 51:1945, 1983.

[20] C. Jarlskog. Commutator of the quark mass matrices in the standard electroweak model and a measure of maximal CP violation. *Phys. Rev. Lett.*, 55:1039, 1985.

[21] P. F. Harrison and H. R. Quinn. The *BABAR* physics book: Physics at an asymmetric B factory. Papers from Workshop on Physics at an Asymmetric B Factory (*BABAR* Collaboration Meeting), Rome, Italy, 11-14 Nov 1996, Princeton, NJ, 17-20 Mar 1997, Orsay, France, 16-19 Jun 1997 and Pasadena, CA, 22-24 Sep 1997.

[22] S. Eidelman et al. Review of particle physics. *Phys. Lett.*, B592:1, 2004.

[23] V. Fanti et al. A new measurement of direct CP violation in two pion decays of the neutral kaon. *Phys. Lett.*, B465:335–348, 1999.

[24] A. Alavi-Harati et al. Observation of direct CP violation in $K_{S,L} \to \pi\pi$ decays. *Phys. Rev. Lett.*, 83:22, 1999.

[25] B. Aubert et al. Observation of direct CP violation in $B^0 \to K/\pi$ decays. *Phys. Rev. Lett.*, 93:131801, 2004.

[26] http://belle.kek.jp/.

[27] B. Aubert et al. Improved measurement of CP asymmetries in $B^0 \to c\bar{c}K^{(*)0}$ decays. 2006. hep-ex/0607107.

[28] K.F. Chen et al. Observation of Time-Dependent CP Violation in $B^0 \to \eta' K^0$ Decays and Improved Measurements of CP Asymmetries in $B^0 \to \phi K^0, K_S^0 K_S^0 K_S^0$ and $B^0 \to J/\psi K^0$ Decays. 2007.

[29] E. Barberio et al. Averages of b-hadron properties at the end of 2006. 2007.

[30] http://cern.ch/lhcb.

[31] M. Beneke et al. Angles of the Unitarity Triangle: Measurements and perspectives. Invited talk at 2nd Workshop on the CKM Unitarity Triangle, Durham, England, 5-9 Apr 2003.

[32] A. Jawahery. CKM unitarity angles α (ϕ_2) and γ (ϕ_3). *Int. J. Mod. Phys.*, A19:975–990, 2004.

[33] J. Charles et al. CP violation and the CKM matrix: Assessing the impact of the asymmetric B factories. *Eur. Phys. J.*, C41:1–131, 2005.

[34] A. Bornheim et al. Improved measurement of $|V_{ub}|$ with inclusive semileptonic B decays. *Phys. Rev. Lett.*, 88:231803, 2002.

[35] Gerhard Buchalla, Andrzej J. Buras, and Markus E. Lautenbacher. Weak decays beyond leading logarithms. *Rev. Mod. Phys.*, 68(4):1125–1244, Oct 1996.

[36] Ahmed Ali, G. Kramer, and Cai-Dian Lu. Experimental tests of factorization in charmless non-leptonic two-body B decays. *Phys. Rev. D.*, 58:094009, 1998.

[37] Martin Beneke and Neubert Matthias. QCD factorization for $B \to PP$ and $B \to PV$ decays. *Nucl. Phys.*, B675:333–415, 2003.

[38] M. Beneke, G. Buchalla, M. Neubert, and C. T. Sachrajda. QCD factorization for $B \to \pi\pi$ decays: Strong phases and cp violation in the heavy quark limit. *Phys. Rev. Lett.*, 83(10):1914–1917, Sep 1999.

[39] M. Beneke, G. Buchalla, M. Neubert, and C. T. Sachrajda. QCD factorization for exclusive non-leptonic B-meson decays: general arguments and the case of heavy-light final states. *Nucl. Phys. B*, 591:313–418, Dec 2000.

[40] M. Beneke, G. Buchalla, M. Neubert, and C. T. Sachrajda. QCD factorization for $B \to PP$ and $B \to PV$ decays. *Nucl. Phys. B*, 675:333–415, Dec 2003.

[41] M. Beneke, G. Buchalla, M. Neubert, and C. T. Sachrajda. QCD factorization in $B \to \pi K, \pi\pi$ decays and extraction of Wolfenstein parameters. *Nucl. Phys. B*, 606:245–321, July 2001.

[42] W. Kozanecki. The PEP-II B-factory: Status and prospects. *Nucl. Instrum. Meth.*, A446:59–64, 2000.

[43] B. Aubert et al. Measurement of the B^+/B^0 production ratio from the $\Upsilon(4S)$ meson using $B^+ \to J/\psi K^+$ and $B^0 \to J/\psi K^0_S$ decays. *Phys. Rev.*, D69:071101, 2004.

[44] B. Aubert et al. The *BABAR* detector. *Nucl. Instrum. Meth.*, A479:1–116, 2002.

[45] A. J. Smith et al. A barrel IFR instrumented with limited streamer tubes. http://www.slac.stanford.edu/BFROOT/www/Detector/LST/documentation/LSTprop-A4-May30-ajss.pdf.

[46] Pierre Billoir. Track fitting with multiple scattering: A new method. *Nucl. Instrum. Meth.*, A225:352, 1984.

[47] S. Spanier and G. Mancinelli. Kaon selection at *BABAR*. *BABAR* Analysis Document #116.

[48] T. Brandt. Likelihood-based electron identification. *BABAR* Analysis Document #396.

[49] C. Hearty. Measurement of the number of $\Upsilon(4S)$ mesons produced in run 1 (B counting). *BABAR* Analysis Document #134.

[50] W. M. Dunwoodie. Simple observations on $B\overline{B}$ kinematics. http://www.slac.stanford.edu/~wmd/bbkinematics/kinematics.note.

[51] J. Smith et al. Recommendation for exclusive B reconstruction analysis variables. *BABAR* Note #134.

[52] W. T. Ford. Choice of kinematic variables in B meson reconstruction—take 3. *BABAR* Analysis Document #53.

[53] A. Hoecker et al. Measurement of cp-violating asymmetries in $B^0 \rightarrow \pi^+\pi^-\pi^0$. *BABAR* Analysis Document #637.

[54] G. Cowan. *Statistical data analysis*. Oxford University Press Inc., 1998.

[55] F. James and M. Roos. 'MINUIT' a system for function minimization and analysis of the parameter errors and correlations. *Comput. Phys. Commun.*, 10:343–367, 1975.

[56] F. James. MINUIT, function minimization and error analysis, reference manual. http://wwwasdoc.web.cern.ch/wwwasdoc/minuit/minmain.html.

[57] Kirkby D. and Verkerke W. RooFit users manual v2.07. http://roofit.sourceforge.net/docs/index.html.

[58] ROOT, an object oriented data analysis framework. http://root.cern.ch/.

[59] RooRarFit, an ML fitting package based on ROOT and RooFit. http://rarfit.sourceforge.net/.

[60] I. M. Sobol. *The Monte Carlo Method*. University Chicago Press, Chicago, 1974.

[61] http://www.slac.stanford.edu/BFROOT/dist/releases/analysis-23/Q2BUser/doc/Q2BUser.html.

[62] Heavy flavor averaging group. http://www.slac.stanford.edu/xorg/hfag/.

[63] Muriel Pivk and Francois R. Le Diberder. ${}_s\mathcal{P}lot$: a statistical tool to unfold data distributions. *Nucl. Instrum. Methods*, 555:356–369, 2005.

[64] B. Aubert et al. Measurement of CP-violating asymmetries in $B^0 \rightarrow (\rho\pi)^0$ using a time-dependent dalitz plot analysis. *Phys. Rev.*, D76:012004, 2007.